

2. The Milky Way as a Galaxy

The Earth is orbiting around the Sun, which itself is orbiting around the center of the Milky Way. Our Milky Way, the Galaxy, is the only galaxy in which we are able to study astrophysical processes in detail. Therefore, our journey through extragalactic astronomy will begin in our home Galaxy, with which we first need to become familiar before we are ready to take off into the depths of the Universe. Knowing the properties of the Milky Way is indispensable for understanding other galaxies.

2.1 Galactic Coordinates

On a clear night, and sufficiently far away from cities, one can see the magnificent band of the Milky Way on the sky (Fig. 2.1). This observation suggests that the distribution of light, i.e., that of the stars in the Galaxy, is predominantly that of a thin disk. A detailed analysis of the geometry of the distribution of stars and gas confirms this impression. This geometry of the Galaxy suggests the introduction of two specially adapted coordinate systems which are particularly convenient for quantitative descriptions.

Spherical Galactic Coordinates (ℓ, b). We consider a spherical coordinate system, with its center being “here”, at the location of the Sun (see Fig. 2.2). The *Galactic plane* is the plane of the Galactic disk, i.e., it is parallel to the band of the Milky Way. The two *Galactic coordinates* ℓ and b are angular coordinates on the sphere. Here, b denotes the *Galactic latitude*, the

angular distance of a source from the Galactic plane, with $b \in [-90^\circ, +90^\circ]$. The great circle $b = 0^\circ$ is then located in the plane of the Galactic disk. The direction $b = 90^\circ$ is perpendicular to the disk and denotes the North Galactic Pole (NGP), while $b = -90^\circ$ marks the direction to the South Galactic Pole (SGP). The second angular coordinate is the *Galactic longitude* ℓ , with $\ell \in [0^\circ, 360^\circ]$. It measures the angular separation between the position of a source, projected perpendicularly onto the Galactic disk (see Fig. 2.2), and the Galactic center, which itself has angular coordinates $b = 0^\circ$ and $\ell = 0^\circ$. Given ℓ and b for a source, its location on the sky is fully specified. In order to specify its three-dimensional location, the distance of that source from us is also needed.

The conversion of the positions of sources given in Galactic coordinates (b, ℓ) to that in equatorial coordinates (α, δ) and vice versa is obtained from the rotation between these two coordinate systems, and is described by spherical trigonometry.¹ The necessary formulae can be found in numerous standard texts. We will not reproduce them here, since nowadays this transformation is done nearly exclusively using computer programs. Instead, we will give some examples. The following figures refer to the Epoch 2000: due to the precession

¹The equatorial coordinates are defined by the direction of the Earth’s rotation axis and by the rotation of the Earth. The intersections of the Earth’s axis and the sphere define the northern and southern poles. The great circles on the sphere through these two poles, the meridians, are curves of constant *right ascension* α . Curves perpendicular to them and parallel to the projection of the Earth’s equator onto the sky are curves of constant *declination* δ , with the poles located at $\delta = \pm 90^\circ$.



Fig. 2.1. An unusual optical image of the Milky Way. This total view of the Galaxy is composed of a large number of individual images

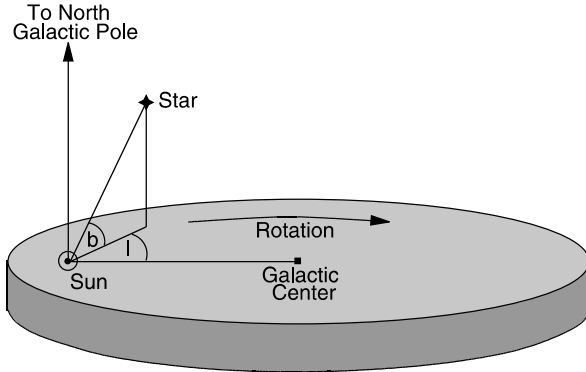


Fig. 2.2. The Sun is at the origin of the Galactic coordinate system. The directions to the Galactic center and to the North Galactic Pole (NGP) are indicated and are located at $l = 0^\circ$ and $b = 0^\circ$, and at $b = 90^\circ$, respectively

of the rotation axis of the Earth, the equatorial coordinate system changes with time, and is updated from time to time. The position of the Galactic center (at $l = 0^\circ = b$) is $\alpha = 17^{\text{h}}45.6^{\text{m}}$, $\delta = -28^\circ56'2$ in equatorial coordinates. This immediately implies that at the La Silla Observatory, located at geographic latitude -29° , the Galactic center is found near the zenith at local midnight in May/June. Because of the high stellar density in the Galactic disk and the large extinction due to dust this is therefore not a good season for extragalactic observations from La Silla. The North Galactic Pole has coordinates $\alpha_{\text{NGP}} = 192.85948^\circ \approx 12^{\text{h}}51^{\text{m}}$, $\delta_{\text{NGP}} = 27.12825^\circ \approx 27^\circ7'7$.

Zone of Avoidance. As already mentioned, the absorption by dust and the presence of numerous bright stars render optical observations of extragalactic sources in the direction of the disk difficult. The best observing conditions are found at large $|b|$, while it is very hard to do extragalactic astronomy in the optical regime at $|b| \lesssim 10^\circ$; this region is therefore often called the “Zone of Avoidance”. An illustrative example is the galaxy Dwingeloo 1, which was already mentioned in Sect. 1.1 (see Fig. 1.6). This galaxy was only discovered in the 1990s despite being in our immediate vicinity: it is located at low $|b|$, right in the Zone of Avoidance.

Cylindrical Galactic Coordinates (R, θ, z). The angular coordinates introduced above are well suited to describing the angular position of a source relative to the

Galactic disk. However, we will now introduce another three-dimensional coordinate system for the description of the Milky Way geometry that will prove very convenient in the study of the kinematic and dynamic properties of the Milky Way. It is a cylindrical coordinate system, with the Galactic center at the origin (see also Fig. 2.13). The radial coordinate R measures the distance of an object from the Galactic center in the disk, and z specifies the height above the disk (objects with negative z are thus located below the Galactic disk, i.e., south of it). For instance, the Sun has a distance from the Galactic center of $R \approx 8$ kpc. The angle θ specifies the angular separation of an object in the disk relative to the position of the Sun, seen from the Galactic center. The distance of an object with coordinates R, θ, z from the Galactic center is then $\sqrt{R^2 + z^2}$, independent of θ . If the matter distribution in the Milky Way were axially symmetric, the density would then depend only on R and z , but not on θ . Since this assumption is a good approximation, this coordinate system is very well suited for the physical description of the Galaxy.

2.2 Determination of Distances Within Our Galaxy

A central problem in astronomy is the estimation of distances. The position of sources on the sphere gives us a two-dimensional picture. To obtain three-dimensional information, measurements of distances are required. Furthermore, we need to know the distance to a source if we want to draw conclusions about its physical parameters. For example, we can directly observe the angular diameter of an object, but to derive the physical size we need to know its distance. Another example is the determination of the *luminosity* L of a source, which can be derived from the observed *flux* S only by means of its distance D , using

$$L = 4\pi S D^2 . \quad (2.1)$$

It is useful to consider the dimensions of the physical parameters in this equation. The unit of the luminosity is $[L] = \text{erg s}^{-1}$, and that of the flux $[S] = \text{erg s}^{-1} \text{cm}^{-2}$. The flux is the energy passing through a unit area per unit time (see Appendix A). Of course, the physical properties of a source are characterized by the lumi-

osity L and not by the flux S , which depends on its distance from the Sun.

In the following section we will review various methods for the estimation of distances in our Milky Way, postponing the discussion of methods for estimating extragalactic distances to Sect. 3.6.

2.2.1 Trigonometric Parallax

The most important method of distance determination is the *trigonometric parallax*, and not only from a historical point-of-view. This method is based on a purely geometric effect and is therefore independent of any physical assumptions. Due to the motion of the Earth around the Sun the positions of nearby stars on the sphere change relative to those of very distant sources (e.g., extragalactic objects such as quasars). The latter therefore define a fixed reference frame on the sphere (see Fig. 2.3). In the course of a year the apparent position of a nearby star follows an ellipse on the sphere, the semimajor axis of which is called the *parallax* p . The axis ratio of this ellipse depends on the direction of the star relative to the ecliptic (the plane that is defined by the orbits of the planets) and is of no further interest. The parallax depends on the radius r of the Earth's orbit, hence on the Earth–Sun distance which is, by definition, one astronomical unit.² Furthermore, the parallax depends on the distance D of the star,

$$\frac{r}{D} = \tan p \approx p, \quad (2.2)$$

where we used $p \ll 1$ in the last step, and p is measured in radians as usual. The trigonometric parallax is also used to define the common unit of distance in astronomy: one *parsec* (pc) is the distance of a hypothetical source for which the parallax is exactly $p = 1''$. With the conversion of arcseconds to radians ($1'' \approx 4.848 \times 10^{-6}$ radians) one gets $p/1'' = 206\,265 p$, which for a parsec yields

$$1 \text{ pc} = 206\,265 \text{ AU} = 3.086 \times 10^{18} \text{ cm}. \quad (2.3)$$

²To be precise, the Earth's orbit is an ellipse and one astronomical unit is its semimajor axis, being $1 \text{ AU} = 1.496 \times 10^{13} \text{ cm}$.

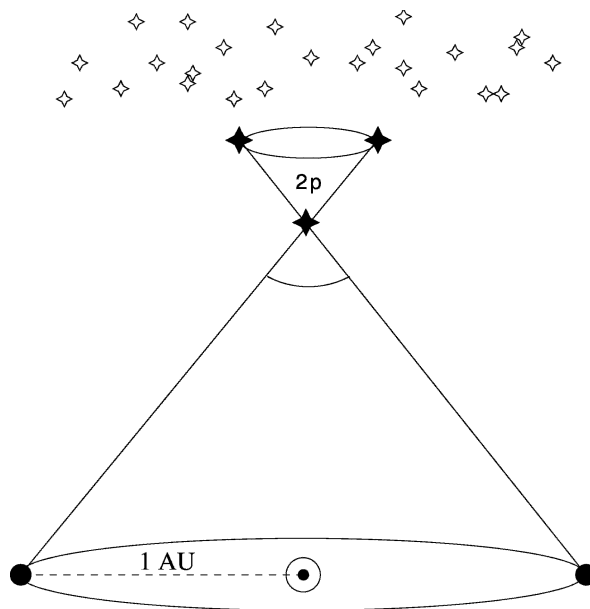


Fig. 2.3. Illustration of the parallax effect: in the course of the Earth's orbit around the Sun the apparent positions of nearby stars on the sky seem to change relative to those of very distant background sources

The distance corresponding to a measured parallax is then calculated as

$$D = \left(\frac{p}{1''}\right)^{-1} \text{ pc}. \quad (2.4)$$

To determine the parallax p , precise measurements of the position of an object at different times are needed, spread over a year, allowing us to measure the ellipse drawn on the sphere by the object's apparent position. For ground-based observation the accuracy of this method is limited by the atmosphere. The seeing causes a blurring of the images of astronomical sources and thus limits the accuracy of position measurements. From the ground this method is therefore limited to parallaxes larger than $\approx 0''.01$, implying that the trigonometric parallax yields distances to stars only within ~ 30 pc.

An extension of this method towards smaller p , and thus larger distances, became possible with the astrometric satellite HIPPARCOS. It operated between November 1989 and March 1993 and measured the positions and trigonometric parallaxes of about 120 000 bright stars, with a precision of $\sim 0''.001$ for the brighter targets. With HIPPARCOS the method of trigonomet-

ric parallax could be extended to stars up to distances of ~ 300 pc. The satellite GAIA, the successor mission to HIPPARCOS, is scheduled to be launched in 2012. GAIA will compile a catalog of $\sim 10^9$ stars up to $V \approx 20$ in four broad-band and eleven narrow-band filters. It will measure parallaxes for these stars with an accuracy of $\sim 2 \times 10^{-4}$ arcsec, with the accuracy for brighter stars even being considerably better. GAIA will thus determine the distances for $\sim 2 \times 10^8$ stars with a precision of 10%, and tangential velocities (see next section) with a precision of better than 3 km/s.

The trigonometric parallax method forms the basis of nearly all distance determinations owing to its purely geometrical nature. For example, using this method the distances to nearby stars have been determined, allowing the production of the Hertzsprung–Russell diagram (see Appendix B.2). Hence, all distance measures that are based on the properties of stars, such as will be described below, are calibrated by the trigonometric parallax.

2.2.2 Proper Motions

Stars are moving relative to us or, more precisely, relative to the Sun. To study the kinematics of the Milky Way we need to be able to measure the velocities of stars. The radial component v_r of the velocity is easily obtained from the Doppler shift of spectral lines,

$$v_r = \frac{\Delta\lambda}{\lambda_0} c, \quad (2.5)$$

where λ_0 is the rest-frame wavelength of an atomic transition and $\Delta\lambda = \lambda_{\text{obs}} - \lambda_0$ the Doppler shift of the wavelength due to the radial velocity of the source. The sign of the radial velocity is defined such that $v_r > 0$ corresponds to a motion away from us, i.e., to a redshift of spectral lines.

In contrast, the determination of the other two velocity components is much more difficult. The tangential component, v_t , of the velocity can be obtained from the *proper motion* of an object. In addition to the motion caused by the parallax, stars also change their positions on the sphere as a function of time because of the transverse component of their velocity relative to the Sun. The proper motion μ is thus an angular velocity, e.g., measured in milliarcseconds per year (mas/yr).

This angular velocity is linked to the tangential velocity component via

$$v_t = D\mu \quad \text{or} \quad \frac{v_t}{\text{km/s}} = 4.74 \left(\frac{D}{1 \text{ pc}} \right) \left(\frac{\mu}{1''/\text{yr}} \right). \quad (2.6)$$

Therefore, one can calculate the tangential velocity from the proper motion and the distance. If the latter is derived from the trigonometric parallax, (2.6) and (2.4) can be combined to yield

$$\frac{v_t}{\text{km/s}} = 4.74 \left(\frac{\mu}{1''/\text{yr}} \right) \left(\frac{p}{1''} \right)^{-1}. \quad (2.7)$$

HIPPARCOS measured proper motions for $\sim 10^5$ stars with an accuracy of up to a few mas/yr; however, they can be translated into physical velocities only if their distance is known.

Of course, the proper motion has two components, corresponding to the absolute value of the angular velocity and its direction on the sphere. Together with v_r this determines the three-dimensional velocity vector. Correcting for the known velocity of the Earth around the Sun, one can then compute the velocity vector \mathbf{v} of the star relative to the Sun, called the *heliocentric velocity*.

2.2.3 Moving Cluster Parallax

The stars in an (open) star cluster all have a very similar spatial velocity. This implies that their proper motion vectors should be similar. To what extent the proper motions are aligned depends on the angular extent of the star cluster on the sphere. Like two railway tracks that run parallel but do not appear parallel to us, the vectors of proper motions in a star cluster also do not appear parallel. They are directed towards a convergence point, as depicted in Fig. 2.4. We shall demonstrate next how to use this effect to determine the distance to a star cluster.

We consider a star cluster and assume that all stars have the same spatial velocity \mathbf{v} . The position of the i -th star as a function of time is then described by

$$\mathbf{r}_i(t) = \mathbf{r}_i + \mathbf{v}t, \quad (2.8)$$

where \mathbf{r}_i is the current position if we identify the origin of time, $t = 0$, with “today”. The direction of a star

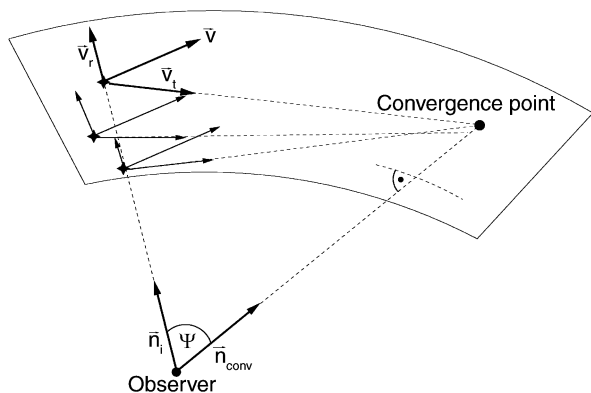


Fig. 2.4. The moving cluster parallax is a projection effect, similar to that known from viewing railway tracks. The directions of velocity vectors pointing away from us seem to converge and intersect at the convergence point. The connecting line from the observer to the convergence point is parallel to the velocity vector of the star cluster

relative to us is described by the unit vector

$$\mathbf{n}_i(t) := \frac{\mathbf{r}_i(t)}{|\mathbf{r}_i(t)|} . \quad (2.9)$$

From this, one infers that for large times, $t \rightarrow \infty$, the direction vectors are identical for all stars in the cluster,

$$\mathbf{n}_i(t) \rightarrow \frac{\mathbf{v}}{|\mathbf{v}|} =: \mathbf{n}_{\text{conv}} . \quad (2.10)$$

Hence for large times all stars will appear at the same point \mathbf{n}_{conv} : the convergence point. This only depends on the direction of the velocity vector of the star cluster. In other words, the direction vector of the stars is such that they are all moving towards the convergence point. Thus, \mathbf{n}_{conv} (and hence $\mathbf{v}/|\mathbf{v}|$) can be measured from the direction of the proper motions of the stars in the cluster, and so can $\mathbf{v}/|\mathbf{v}|$. On the other hand, one component of \mathbf{v} can be determined from the (easily measured) radial velocity v_r . With these two observables the three-dimensional velocity vector \mathbf{v} is completely determined, as is easily demonstrated: let ψ be the angle between the line-of-sight \mathbf{n} towards a star in the cluster and \mathbf{v} . The angle ψ is directly read off from the direction vector \mathbf{n} and the convergence point, $\cos \psi = \mathbf{n} \cdot \mathbf{v}/|\mathbf{v}| = \mathbf{n}_{\text{conv}} \cdot \mathbf{n}$. With $v \equiv |\mathbf{v}|$ one then obtains

$$v_r = v \cos \psi , \quad v_t = v \sin \psi ,$$

and so

$$v_t = v_r \tan \psi . \quad (2.11)$$

This means that the tangential velocity v_t can be measured without determining the distance to the stars in the cluster. On the other hand, (2.6) defines a relation between the proper motion, the distance, and v_t . Hence, a distance determination for the star is now possible with

$$\mu = \frac{v_t}{D} = \frac{v_r \tan \psi}{D} \rightarrow D = \frac{v_r \tan \psi}{\mu} . \quad (2.12)$$

This method yields accurate distance estimates of star clusters within ~ 200 pc. The accuracy depends on the measurability of the proper motions. Furthermore, the cluster should cover a sufficiently large area on the sky for the convergence point to be well defined. For the distance estimate, one can then take the average over a large number of stars in the cluster if one assumes that the spatial extent of the cluster is much smaller than its distance to us. Targets for applying this method are the Hyades, a cluster of about 200 stars at a mean distance of $D \approx 45$ pc, the Ursa-Major group of about 60 stars at $D \approx 24$ pc, and the Pleiades with about 600 stars at $D \approx 130$ pc.

Historically the distance determination to the Hyades, using the moving cluster parallax, was extremely important because it defined the scale to all other, larger distances. Its constituent stars of known distance are used to construct a calibrated Hertzsprung–Russell diagram which forms the basis for determining the distance to other star clusters, as will be discussed in Sect. 2.2.4. In other words, it is the lowest rung of the so-called distance ladder that we will discuss in Sect. 3.6. With HIPPARCOS, however, the distance to the Hyades stars could also be measured using the trigonometric parallax, yielding more accurate values. HIPPARCOS was even able to differentiate the “near” from the “far” side of the cluster – this star cluster is too close for the assumption of an approximately equal distance of all its stars to be still valid. A recent value for the mean distance of the Hyades is

$$\overline{D}_{\text{Hyades}} = 46.3 \pm 0.3 \text{ pc} . \quad (2.13)$$

2.2.4 Photometric Distance; Extinction and Reddening

Most stars in the color–magnitude diagram are located along the main sequence. This enables us to compile a calibrated main sequence of those stars whose

trigonometric parallaxes are measured, thus with known distances. Utilizing photometric methods, it is then possible to derive the distance to a star cluster, as we will demonstrate in the following.

The stars of a star cluster define their own main sequence (color–magnitude diagrams for some star clusters are displayed in Fig. 2.5); since they are all located at the same distance, their main sequence is already defined in a color–magnitude diagram in which only apparent magnitudes are plotted. This cluster main sequence can then be fitted to a calibrated main sequence³ by a suitable choice of the distance, i.e., by adjusting the distance modulus $m - M$,

$$m - M = 5 \log (D/\text{pc}) - 5 ,$$

where m and M denote the apparent and absolute magnitude, respectively.

In reality this method cannot be applied so easily since the position of a star on the main sequence does not only depend on its mass but also on its age and metallicity. Furthermore, only stars of luminosity class V (i.e., dwarf stars) define the main sequence, but without spectroscopic data it is not possible to determine the luminosity class.

Extinction and Reddening. Another major problem is extinction. Absorption and scattering of light by dust affect the relation of absolute to apparent magnitude: for a given M , the apparent magnitude m becomes larger (fainter) in the case of absorption, making the source appear dimmer. Also, since extinction depends on wavelength, the spectrum of the source is modified and the observed color of the star changes. Because extinction by dust is always associated with such a change in color, one can estimate the absorption – provided one has sufficient information on the intrinsic color of a source or of an ensemble of sources. We will now demonstrate how this method can be used to estimate the distance to a star cluster.

We consider the equation of radiative transfer for pure absorption or scattering (see Appendix A),

$$\boxed{\frac{dI_\nu}{ds} = -\kappa_\nu I_\nu} , \quad (2.14)$$

³i.e., to the main sequence in a color–magnitude diagram in which absolute magnitudes are plotted

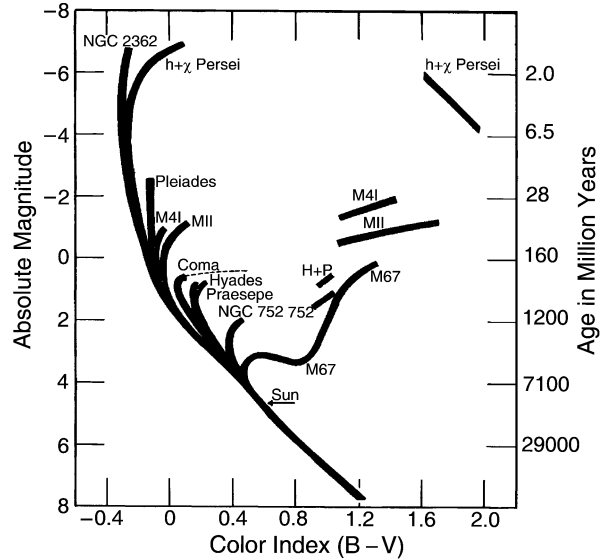


Fig. 2.5. Color–magnitude diagram (CMD) for different star clusters. Such a diagram can be used for the distance determination of star clusters because the absolute magnitudes of main-sequence stars are known (by calibration with nearby clusters, especially the Hyades). One can thus determine the distance modulus by vertically “shifting” the main sequence. Also, the age of a star cluster can be estimated from a CMD: luminous main-sequence stars have a shorter lifetime on the main sequence than less luminous ones. The turn-off point in the stellar sequence away from the main sequence therefore corresponds to that stellar mass for which the lifetime on the main sequence equals the age of the star cluster. Accordingly, the age is specified on the right axis as a function of the position of the turn-off point; the Sun will leave the main sequence after about 10×10^9 years

where I_ν denotes the specific intensity at frequency ν , κ_ν the absorption coefficient, and s the distance coordinate along the light beam. The absorption coefficient has the dimension of an inverse length. Equation (2.14) says that the amount by which the intensity of a light beam is diminished on a path of length ds is proportional to the original intensity and to the path length ds . The absorption coefficient is thus defined as the constant of proportionality. In other words, on the distance interval ds , a fraction $\kappa_\nu ds$ of all photons at frequency ν is absorbed or scattered out of the beam. The solution of the transport equation (2.14) is obtained by writing it in the form $d \ln I_\nu = dI_\nu/I_\nu = -\kappa_\nu ds$ and integrating from 0 to s ,

$$\ln I_\nu(s) - \ln I_\nu(0) = - \int_0^s ds' \kappa_\nu(s') \equiv -\tau_\nu(s),$$

where in the last step we defined the *optical depth*, τ_ν , which depends on frequency. This yields

$$I_\nu(s) = I_\nu(0) e^{-\tau_\nu(s)}. \quad (2.15)$$

The specific intensity is thus reduced by a factor $e^{-\tau}$ compared to the case of no absorption taking place. Accordingly, for the flux we obtain

$$S_\nu = S_\nu(0) e^{-\tau_\nu(s)}, \quad (2.16)$$

where S_ν is the flux measured by the observer at a distance s from the source, and $S_\nu(0)$ is the flux of the source without absorption. Because of the relation between flux and magnitude $m = -2.5 \log S + \text{const}$, or $S \propto 10^{-0.4m}$, one has

$$\frac{S_\nu}{S_{\nu,0}} = 10^{-0.4(m-m_0)} = e^{-\tau_\nu} = 10^{-\log(e)\tau_\nu},$$

or

$$\begin{aligned} A_\nu &:= m - m_0 = -2.5 \log(S_\nu/S_{\nu,0}) \\ &= 2.5 \log(e) \tau_\nu = 1.086 \tau_\nu. \end{aligned} \quad (2.17)$$

Here, A_ν is the *extinction coefficient* describing the change of apparent magnitude m compared to that without absorption, m_0 . Since the absorption coefficient κ_ν depends on frequency, absorption is always linked to a change in color. This is described by the *color excess* which is defined as follows:

$$\begin{aligned} E(X - Y) &:= A_X - A_Y = (X - X_0) - (Y - Y_0) \\ &= (X - Y) - (X - Y)_0. \end{aligned} \quad (2.18)$$

The color excess describes the change of the color index $(X - Y)$, measured in two filters X and Y that define the corresponding spectral windows by their transmission curves. The ratio $A_X/A_Y = \tau_{\nu(X)}/\tau_{\nu(Y)}$ depends only on the optical properties of the dust or, more specifically, on the ratio of the absorption coefficients in the two frequency bands X and Y considered here. Thus, the color excess is proportional to the extinction coefficient,

$$\begin{aligned} E(X - Y) &= A_X - A_Y = A_X \left(1 - \frac{A_Y}{A_X}\right) \\ &\equiv A_X R_X^{-1}, \end{aligned} \quad (2.19)$$

where in the last step we introduced the factor of proportionality R_X between the extinction coefficient and the color excess, which depends only on the properties of the dust and the choice of the filters. Usually, one uses a blue and a visual filter (see Appendix A.4.2 for a description of the filters commonly used) and writes

$$A_V = R_V E(B - V). \quad (2.20)$$

For example, for dust in our Milky Way we have the characteristic relation

$$A_V = (3.1 \pm 0.1) E(B - V). \quad (2.21)$$

This relation is not a universal law, but the factor of proportionality depends on the properties of the dust. They are determined, e.g., by the chemical composition and the size distribution of the dust grains. Fig. 2.6 shows the wavelength dependence of the extinction coefficient for different kinds of dust, corresponding to different values of R_V . In the optical part of the spectrum we have

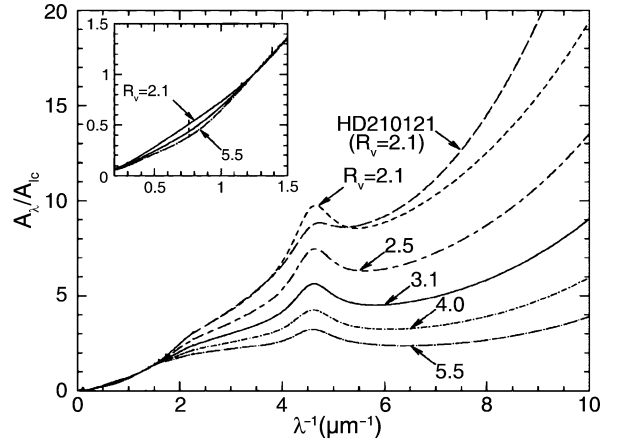


Fig. 2.6. Wavelength dependence of the extinction coefficient A_ν , normalized to the extinction coefficient A_I at $\lambda = 9000 \text{ \AA}$. Different kinds of clouds, characterized by the value of R_V , i.e., by the reddening law, are shown. On the x -axis we have plotted the inverse wavelength, so that the frequency increases to the right. The solid line specifies the mean Galactic extinction curve. The extinction coefficient, as determined from the observation of an individual star, is also shown; clearly the observed law deviates from the model in some details. The figure insert shows a detailed plot at relatively large wavelengths in the NIR range of the spectrum; at these wavelengths the extinction depends only weakly on the value of R_V .

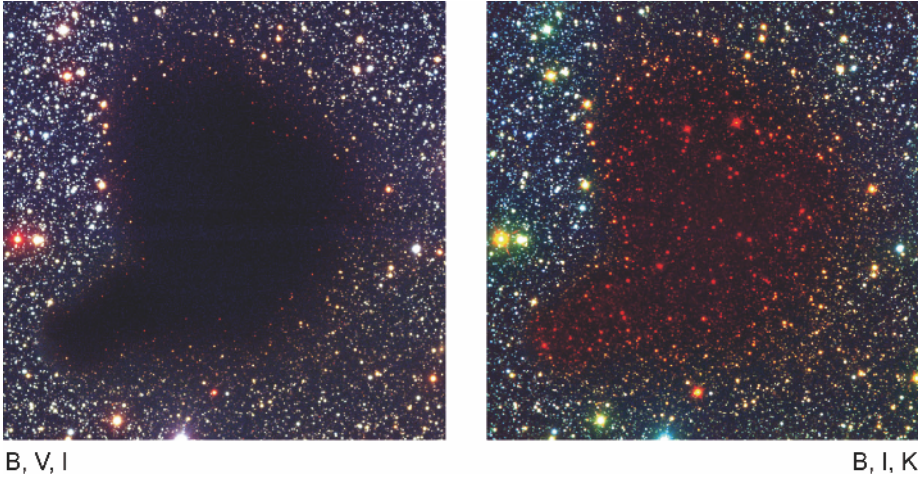


Fig. 2.7. These images of the molecular cloud Barnard 68 show the effects of extinction and reddening: the left image is a composite of exposures in the filters B, V, and I. At the center of the cloud essentially all the light from the background stars is absorbed. Near the edge it is dimmed

and visibly shifted to the red. In the right-hand image observations in the filters B, I, and K have been combined (red is assigned here to the near-infrared K-band filter); we can clearly see that the cloud is more transparent at longer wavelengths

approximately $\tau_\nu \propto \nu$, i.e., blue light is absorbed (or scattered) more strongly than red light. The extinction therefore always causes a reddening.⁴

In the Solar neighborhood the extinction coefficient for sources in the disk is about

$$A_V \approx 1 \text{ mag} \frac{D}{1 \text{ kpc}}, \quad (2.22)$$

but this relation is at best a rough approximation, since the absorption coefficient can show strong local deviations from this law, for instance in the direction of molecular clouds (see, e.g., Fig. 2.7).

Color-color diagram. We now return to the distance determination for a star cluster. As a first step in this measurement, it is necessary to determine the degree of extinction, which can only be done by analyzing the reddening. The stars of the cluster are plotted in a *color-color diagram*, for example by plotting the colors $(U - B)$ and $(B - V)$ on the two axes (see Fig. 2.8). A color-color diagram also shows a main sequence along which the majority of the stars are aligned. The wavelength-dependent extinction causes a reddening *in both colors*. This shifts the positions of the stars in the

diagram. The direction of the reddening vector depends only on the properties of the dust and is here assumed to be known, whereas the *amplitude* of the shift depends on the extinction coefficient. In a similar way to the CMD, this amplitude can now be determined if one has access to a calibrated, unreddened main sequence for the color-color diagram which can be obtained from the examination of nearby stars. From the relative shift of the main sequence in the two diagrams one can then derive the reddening and thus the extinction. The essential point here is the fact that the color-color diagram is independent of the distance.

This then defines the procedure for the distance determination of a star cluster using photometry: in the first step we determine the reddening $E(B - V)$, and thus with (2.21) also A_V , by shifting the main sequence in a color-color diagram along the reddening vector until it matches a calibrated main sequence. In the second step the distance modulus is then determined by vertically (i.e., in the direction of M) shifting the main sequence in the color-magnitude diagram until it matches a calibrated main sequence. From this, the distance is then obtained according to

$$m - M = 5 \log(D/1 \text{ pc}) - 5 + A \quad . \quad (2.23)$$

⁴With what we have just learned we can readily answer the question of why the sky is blue and the setting Sun red.

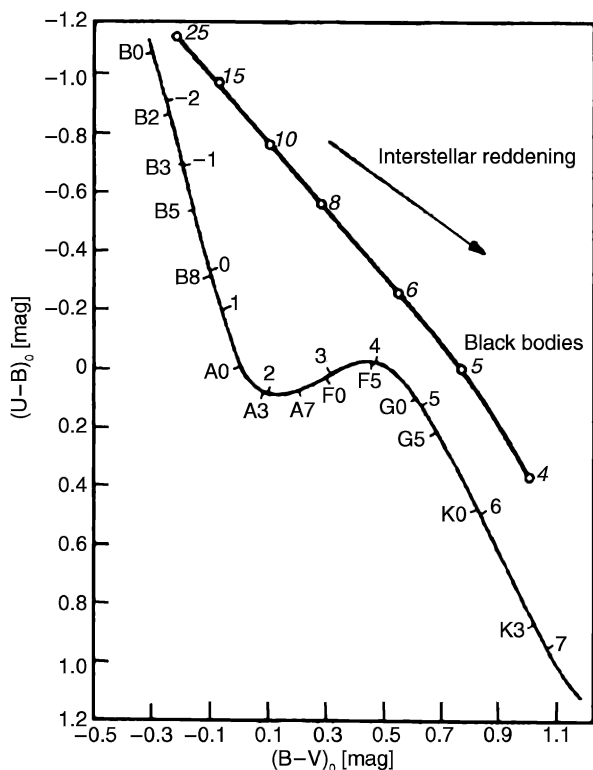


Fig. 2.8. Color-color diagram for main-sequence stars. Spectral types and absolute magnitudes are specified. Black bodies ($T/10^3$ K) would be located along the upper line. Interstellar reddening shifts the measured stellar locations parallel to the reddening vector indicated by the arrow

2.2.5 Spectroscopic Distance

From the spectrum of a star, the spectral type as well as the luminosity class can be determined. The former is determined from the strength of various absorption lines in the spectrum, while the latter is obtained from the width of the lines. From the line width the surface gravity of the star can be derived, and from that its radius (more precisely, M/R^2). From the spectral type and the luminosity class the position of the star in the HRD follows unambiguously. By means of stellar evolution models, the absolute magnitude M_V can then be determined. Furthermore, the comparison of the observed color with that expected from theory yields the color excess $E(B-V)$, and from that we obtain A_V . With this information we are then able to determine the distance using

$$V - A_V - M_V = 5 \log(D/\text{pc}) - 5. \quad (2.24)$$

2.2.6 Distances of Visual Binary Stars

Kepler's third law for a two-body problem,

$$P^2 = \frac{4\pi^2}{G(m_1 + m_2)} a^3, \quad (2.25)$$

specifies the relation between the orbital period P of a binary star, the masses m_i of the two components, and the semimajor axis a of the ellipse. The latter is defined by the distance vector between the two stars in the course of one period. This law can be used to determine the distance to a visual binary star. For such a system, the period P and the angular diameter 2θ of the orbit are direct observables. If one additionally knows the mass of the two stars, for instance from their spectral classification, a can be determined according to (2.25), and from this the distance follows with $D = a/\theta$.

2.2.7 Distances of Pulsating Stars

Several types of pulsating stars show periodic changes in their brightnesses, where the period of a star is related to its mass, and thus to its luminosity. This period-luminosity (PL) relation is ideally suited for distance measurements: since the determination of the period is independent of distance, one can obtain the luminosity directly from the period. The distance is thus directly derived from the measured magnitude using (2.24), if the extinction can be determined from color measurements.

The existence of a relation between the luminosity and the pulsation period can be expected from simple physical considerations. Pulsations are essentially radial density waves inside a star that propagate with the speed of sound, c_s . Thus, one can expect that the period is comparable to the sound crossing time through the star, $P \sim R/c_s$. The speed of sound c_s in a gas is of the same order of magnitude as the thermal velocity of the gas particles, so that $k_B T \sim m_p c_s^2$, where m_p is the proton mass (and thus a characteristic mass of particles in the stellar plasma) and k_B is Boltzmann's constant. According to the virial theorem, one expects that the

gravitational binding energy of the star is about twice the kinetic (i.e., thermal) energy, so that for a proton

$$\frac{GMm_p}{R} \sim k_B T.$$

Combining these relations, for the pulsation period we obtain

$$P \sim \frac{R}{c_s} \sim \frac{R\sqrt{m_p}}{\sqrt{k_B T}} \sim \frac{R^{3/2}}{\sqrt{GM}} \propto \bar{\rho}^{-1/2}, \quad (2.26)$$

where $\bar{\rho}$ is the mean density of the star. This is a remarkable result – the pulsation period depends only on the mean density. Furthermore, the stellar luminosity is related to its mass by approximately $L \propto M^3$. If we now consider stars of equal effective temperature T_{eff} (where $L \propto R^2 T_{\text{eff}}^4$), we find that

$$P \propto \frac{R^{3/2}}{\sqrt{M}} \propto L^{7/12}, \quad (2.27)$$

which is the relation between period and luminosity that we were aiming for.

One finds that a well-defined period–luminosity relation exists for three types of pulsating stars:

- δ Cepheid stars (classical Cepheids). These are young stars found in the disk population (close to the Galactic plane) and in young star clusters. Owing to their position in or near the disk, extinction always plays a role in the determination of their luminosity. To minimize the effect of extinction it is particularly useful to look at the period–luminosity relation in the near-IR (e.g., in the K-band at $\lambda \sim 2.4 \mu\text{m}$). Furthermore, the scatter around the period–luminosity relation is smaller for longer wavelengths of the applied filter, as is also shown in Fig. 2.9. The period–luminosity relation is also steeper for longer wavelengths, resulting in a more accurate determination of the absolute magnitude.
- W Virginis stars, also called Population II Cepheids (we will explain the term of stellar populations in Sect. 2.3.2). These are low-mass, metal-poor stars located in the halo of the Galaxy, in globular clusters, and near the Galactic center.
- RR Lyrae stars. These are likewise Population II stars and thus metal-poor. They are found in the halo, in globular clusters, and in the Galactic bulge. Their absolute magnitudes are confined to a narrow interval, $M_V \in [0.5, 1.0]$, with a mean value of about 0.6. This

obviously makes them very good distance indicators. More precise predictions of their magnitudes are possible with the following dependence on metallicity and period:

$$\begin{aligned} \langle M_K \rangle = & - (2.0 \pm 0.3) \log(P/1d) \\ & + (0.06 \pm 0.04)[\text{Fe}/\text{H}] - 0.7 \pm 0.1. \end{aligned} \quad (2.28)$$

Metallicity. In the last equation, the metallicity of a star was introduced, which needs to be defined. In astrophysics, all chemical elements heavier than helium are called *metals*. These elements, with the exception of some traces of lithium, were not produced in the early Universe but rather later in the interior of stars. The metallicity is thus also a measure of the chemical evolution and enrichment of matter in a star or gas cloud. For an element X, the metallicity index of a star is defined as

$$[\text{X}/\text{H}] \equiv \log \left(\frac{n(\text{X})}{n(\text{H})} \right)_* - \log \left(\frac{n(\text{X})}{n(\text{H})} \right)_\odot, \quad (2.29)$$

thus it is the logarithm of the ratio of the fraction of X relative to hydrogen in the star and in the Sun, where n is the number density of the species considered. For example, $[\text{Fe}/\text{H}] = -1$ means that iron has only a tenth of its Solar abundance. The *metallicity* Z is the total mass fraction of all elements heavier than helium; the Sun has $Z \approx 0.02$, meaning that about 98% of the Solar mass are contributed by hydrogen and helium.

The period–luminosity relations are not only of significant importance for distance determination within our Galaxy. They also play an important role in extragalactic astronomy, since by far the most luminous of the three types of pulsating stars listed above, the Cepheids, are also found and observed in other galaxies; they therefore enable us to directly determine the distances of other galaxies, which is essential for measuring the Hubble constant. These aspects will be discussed in detail in Sect. 3.6.

2.3 The Structure of the Galaxy

Roughly speaking, the Galaxy consists of the disk, the central bulge, and the Galactic halo – a roughly spherical

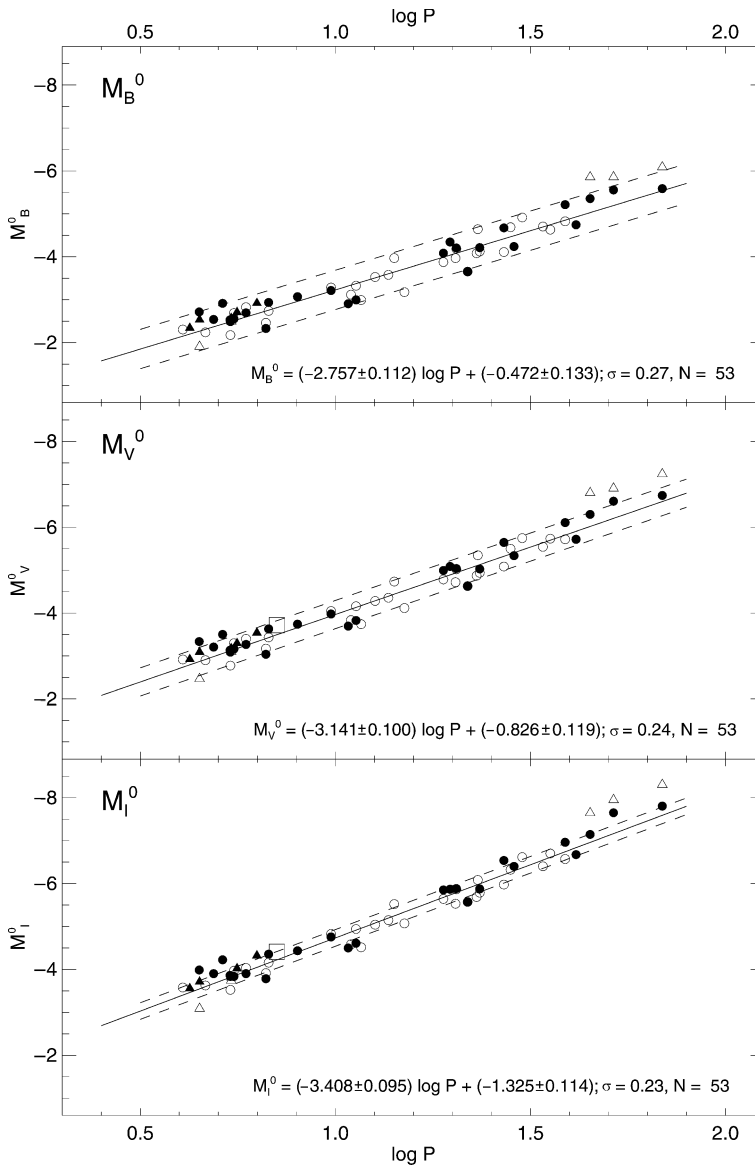


Fig. 2.9. Period–luminosity relation for Galactic Cepheids, measured in three different filter bands (B, V, and I, from top to bottom). The absolute magnitudes were corrected for extinction by using colors. The period is given in days. Open and solid circles denote data for those Cepheids for which distances were estimated using different methods; the three objects marked by triangles have a variable period and are discarded in the derivation of the period–luminosity relation. The latter is indicated by the solid line, with its parametrisation specified in the plots. The broken lines indicate the uncertainty range of the period–luminosity relation. The slope of the period–luminosity relation increases if one moves to redder filters

distribution of stars and globular clusters that surrounds the disk. The disk, whose stars form the visible band of the Milky Way, contains spiral arms similar to those observed in other galaxies. The Sun, together with its planets, orbits around the Galactic center on an approximately circular orbit. The distance R_0 to the Galactic center is not very well known, as we will discuss later. To have a reference value, the International Astronom-

ical Union (IAU) officially defined the value of R_0 in 1985,

$$R_0 = 8.5 \text{ kpc} \quad \text{official value, IAU 1985} . \quad (2.30)$$

More recent examinations have, however, found that the real value is slightly smaller, $R_0 \approx 8.0 \text{ kpc}$. The diameter of the disk of stars, gas, and dust is $\sim 40 \text{ kpc}$.

A schematic depiction of our Galaxy is shown in Fig. 1.3. Its most important structural parameters are listed in Table 2.1.

2.3.1 The Galactic Disk: Distribution of Stars

By measuring the distances of stars in the Solar neighborhood one can determine the three-dimensional stellar distribution. From these investigations, one finds that there are different stellar components, as we will discuss below. For each of them, the number density in the direction perpendicular to the Galactic disk is approximately described by an exponential law,

$$n(z) \propto \exp\left(-\frac{|z|}{h}\right), \quad (2.31)$$

where the *scale-height* h specifies the thickness of the respective component. One finds that h varies between different populations of stars, motivating the definition of different components of the Galactic disk. In principle, three components need to be distinguished: (1) The *young thin disk* contains the largest fraction of gas and dust in the Galaxy, and in this region star formation is still taking place today. The youngest stars are found in the young thin disk, which has a scale-height of about $h_{\text{ytd}} \sim 100$ pc. (2) The *old thin disk* is thicker and has a scale-height of about $h_{\text{otd}} \sim 325$ pc. (3) The *thick disk* has a scale-height of $h_{\text{thick}} \sim 1.5$ kpc. The thick disk contributes only about 2% to the total mass density in the Galactic plane at $z = 0$. This separation into three disk components is rather coarse and can be further refined if one uses a finer classification of stellar populations.

Table 2.1. Parameters and characteristic values for the components of the Milky Way. The scale-height denotes the distance from the Galactic plane at which the density has decreased

	Neutral gas	Thin disk	Thick disk	bulge	Stellar halo	Dm halo
M ($10^{10}M_{\odot}$)	0.5	6	0.2 to 0.4	1	0.1	55
L_{B} ($10^{10}L_{\odot}$)	–	1.8	0.02	0.3	0.1	0
M/L_{B} (M_{\odot}/L_{\odot})	–	3	–	3	~ 1	–
diam. (kpc)	50	50	50	2	100	> 200
form	$e^{-hz/z}$	$e^{-hz/z}$	$e^{-hz/z}$	bar?	$r^{-3.5}$	$(a^2 + r^2)^{-1}$
scale-height (kpc)	0.13	0.325	1.5	0.4	3	2.8
σ_z (km s^{-1})	7	20	40	120	100	–
[Fe/H]	> 0.1	-0.5 to $+0.3$	-1.6 to -0.4	-1 to $+1$	-4.5 to -0.5	–

Molecular gas, out of which new stars are born, has the smallest scale-height, $h_{\text{mol}} \sim 65$ pc, followed by the atomic gas. This can be clearly seen by comparing the distributions of atomic and molecular hydrogen in Fig. 1.5. The younger a stellar population is, the smaller its scale-height. Another characterization of the different stellar populations can be made with respect to the velocity dispersion of the stars, i.e., the amplitude of the components of their random motions. As a first approximation, the stars in the disk move around the Galactic center on circular orbits. However, these orbits are not perfectly circular: besides the orbital velocity (which is about 220 km/s in the Solar vicinity), they have additional random velocity components.

The formal definition of the components of the velocity dispersion is as follows: let $f(\mathbf{v})d^3v$ be the number density of stars (of a given population) at a fixed location, with velocities in a volume element d^3v around \mathbf{v} in the vector space of velocities. If we use Cartesian coordinates, for example $\mathbf{v} = (v_1, v_2, v_3)$, then $f(\mathbf{v})d^3v$ is the number of stars with the i -th velocity component in the interval $[v_i, v_i + dv_i]$, and $d^3v = dv_1 dv_2 dv_3$. The mean velocity $\langle \mathbf{v} \rangle$ of the population then follows from this distribution via

$$\langle \mathbf{v} \rangle = n^{-1} \int_{\mathbb{R}^3} d^3v f(\mathbf{v}) \mathbf{v}, \quad \text{where} \quad n = \int_{\mathbb{R}^3} d^3v f(\mathbf{v}) \quad (2.32)$$

denotes the total number density of stars in the population. The velocity dispersion σ then describes the mean squared deviations of the velocities from $\langle \mathbf{v} \rangle$. For

to $1/e$ of its central value. σ_z is the velocity dispersion in the direction perpendicular to the disk

a component i of the velocity vector, the dispersion σ_i is defined as

$$\begin{aligned}\sigma_i^2 &= \langle (v_i - \langle v_i \rangle)^2 \rangle = \langle v_i^2 - \langle v_i \rangle^2 \rangle \\ &= n^{-1} \int_{\mathbb{R}^3} d^3v f(\mathbf{v}) (v_i^2 - \langle v_i \rangle^2) .\end{aligned}\quad (2.33)$$

The larger σ_i is, the broader the distribution of the stochastic motions. We note that the same concept applies to the velocity distribution of molecules in a gas. The mean velocity $\langle \mathbf{v} \rangle$ at each point defines the bulk velocity of the gas, e.g., the wind speed in the atmosphere, whereas the velocity dispersion is caused by thermal motion of the molecules and is determined by the temperature of the gas.

The random motion of the stars in the direction perpendicular to the disk is the reason for the finite thickness of the population; it is similar to a thermal distribution. Accordingly, it has the effect of a pressure, the so-called *dynamical pressure* of the distribution. This pressure determines the scale-height of the distribution, which corresponds to the law of atmospheres. The larger the dynamical pressure, i.e., the larger the velocity dispersion σ_z perpendicular to the disk, the larger the scale-height h will be. The analysis of stars in the Solar neighborhood yields $\sigma_z \sim 16$ km/s for stars younger than ~ 3 Gyr, corresponding to a scale-height of $h \sim 250$ pc, whereas stars older than ~ 6 Gyr have a scale-height of ~ 350 pc and a velocity dispersion of $\sigma_z \sim 25$ km/s.

The density distribution of the total star population, obtained from counts and distance determinations of stars, is to a good approximation described by

$$n(R, z) = n_0 \left(e^{-|z|/h_{\text{thin}}} + 0.02e^{-|z|/h_{\text{thick}}} \right) e^{-R/h_R} ; \quad (2.34)$$

here, R and z are the cylinder coordinates introduced above (see Sect. 2.1), with the origin at the Galactic center, and $h_{\text{thin}} \approx h_{\text{old}} \approx 325$ pc is the scale-height of the thin disk. The distribution in the radial direction can also be well described by an exponential law, where $h_R \approx 3.5$ kpc denotes the *scale-length of the Galactic disk*. The normalization of the distribution is determined by the density $n \approx 0.2$ stars/pc³ in the Solar neighborhood, for stars in the range of absolute magnitudes of $4.5 \leq M_V \leq 9.5$. The distribution described by (2.34) is

not smooth at $z = 0$; it has a kink at this point and it is therefore unphysical. To get a smooth distribution which follows the exponential law for large z and is smooth in the plane of the disk, the distribution is slightly modified. As an example, for the luminosity density of the old thin disk (that is proportional to the number density of the stars), we can write:

$$L(R, z) = \frac{L_0 e^{-R/h_R}}{\cosh^2(z/h_z)} , \quad (2.35)$$

with $h_z = 2h_{\text{thin}}$ and $L_0 \approx 0.05 L_\odot/\text{pc}^3$. The Sun is a member of the young thin disk and is located above the plane of the disk, at $z = 30$ pc.

2.3.2 The Galactic Disk: Chemical Composition and Age

Stellar Populations. The chemical composition of stars in the thin and the thick disks differs: we observe the clear tendency that stars in the thin disk have a higher metallicity than those in the thick disk. In contrast, the metallicity of stars in the Galactic halo and in the bulge is smaller. To paraphrase these trends, one distinguishes between stars of Population I (Pop I) which have a Solar-like metallicity ($Z \sim 0.02$) and are mainly located in the thin disk, and stars of Population II (Pop II) that are metal-poor ($Z \sim 0.001$) and predominantly found in the thick disk, in the halo, and in the bulge. In reality, stars cover a wide range in Z , and the figures above are only characteristic values. For stellar populations a somewhat finer separation was also introduced, such as “extreme Population I”, “intermediate Population II”, and so on. The populations also differ in age (stars of Pop I are younger than those of Pop II), in scale-height (as mentioned above), and in the velocity dispersion perpendicular to the disk (σ_z is larger for Pop II stars than for Pop I stars).

We shall now attempt to understand the origin of these different metallicities and their relation to the scale-height and to age. We start with a brief discussion of the phenomenon that is the main reason for the metal enrichment of the interstellar medium.

Metallicity and Supernovae. Supernovae (SNe) are explosive events. Within a few days, a SN can reach

a luminosity of $10^9 L_{\odot}$, which is a considerable fraction of the total luminosity of a galaxy; after that the luminosity decreases again with a time-scale of weeks. In the explosion, a star is disrupted and (most of) the matter of the star is driven into the interstellar medium, enriching it with metals that were produced in the course of stellar evolution or in the process of the supernova explosion.

Classification of Supernovae. Depending on their spectral properties, SNe are divided into several classes. SNe of Type I do not show any Balmer lines of hydrogen in their spectrum, in contrast to those of Type II. A further subdivision of Type I SNe is based on spectral properties: SNe Ia show strong emission of Si III λ 6150 Å whereas no Si III at all is visible in spectra of Type Ib,c. Our current understanding of the supernova phenomenon differs from this spectral classification.⁵ Following various observational results and also theoretical analyses, we are confident today that SNe Ia are a phenomenon which is intrinsically different from the other supernova types. For this interpretation, it is of particular importance that SNe Ia are found in all types of galaxies, whereas we observe SNe II and SNe Ib,c only in spiral and irregular galaxies, and here only in those regions in which blue stars predominate. As we will see in Chap. 3, the stellar population in elliptical galaxies consists almost exclusively of old stars, while spirals also contain young stars. From this observational fact it is concluded that the phenomenon of SNe II and SNe Ib,c is linked to a young stellar population, whereas SNe Ia occur in older stellar populations. We shall discuss the two classes of supernovae next.

Core-Collapse Supernovae. SNe II and SNe Ib,c are the final stages in the evolution of massive ($\gtrsim 8M_{\odot}$) stars. Inside these stars, ever heavier elements are generated by fusion: once all the hydrogen is used up, helium will be burned, then carbon, oxygen, etc. This chain comes to an end when the iron nucleus is reached, the atomic nucleus with the highest binding energy per nu-

cleon. After this no more energy can be gained from fusion to heavier elements so that the pressure, which is normally balancing the gravitational force in the star, can no longer be maintained. The star will thus collapse under its own gravity. This gravitational collapse will proceed until the innermost region reaches a density about three times the density of an atomic nucleus. At this point the so-called rebound occurs: a shock wave runs towards the surface, thereby heating the infalling material, and the star explodes. In the center, a compact object probably remains – a neutron star or, possibly, depending on the mass of the iron core, a black hole. Such neutron stars are visible as pulsars⁶ at the location of some historically observed SNe, the most famous of which is the Crab pulsar which has been identified with a supernovae explosion seen by Chinese astronomers in 1054. Presumably all neutron stars have been formed in such core-collapse supernovae.

The major fraction of the binding energy released in the formation of the compact object is emitted in the form of neutrinos: about 3×10^{53} erg. Underground neutrino detectors were able to trace about 10 neutrinos originating from SN 1987A in the Large Magellanic Cloud. Due to the high density inside the star after the collapse, even neutrinos, despite their very small cross-section, are absorbed and scattered, so that part of their outward-directed momentum contributes to the explosion of the stellar envelope. This shell expands at $v \sim 10\,000$ km/s, corresponding to a kinetic energy of $E_{\text{kin}} \sim 10^{51}$ erg. Of this, only about 10^{49} erg is converted into photons in the hot envelope and then emitted – the energy of a SN that is visible in photons is thus only a small fraction of the total energy produced.

Owing to the various stages of nuclear fusion in the progenitor star, the chemical elements are arranged in shells: the light elements (H, He) in the outer shells, and the heavier elements (C, O, Ne, Mg, Si, Ar, Ca, Fe, Ni) in the inner ones – see Fig. 2.10. The explosion ejects them into the interstellar medium which is thus chemically enriched. It is important to note that mainly nuclei with an even number of protons and neutrons are formed. This is a consequence of the nuclear reaction chains

⁵This notation scheme (Type Ia, Type II, and so on) is characteristic for phenomena that one wishes to classify upon discovery, but for which no physical interpretation is available at that time. Other examples are the spectral classes of stars, which are not named in alphabetical order according to their mass on the main sequence, or the division of Seyfert galaxies into Type 1 and Type 2. Once such a notation is established, it often becomes permanent even if a later physical understanding of the phenomenon suggests a more meaningful classification.

⁶Pulsars are sources which show a *very* regular periodic radiation, most often seen at radio frequencies. Their periods lie in the range from $\sim 10^{-3}$ s (millisecond pulsars) to ~ 5 s. Their pulse period is identified as the rotational period of the neutron star – an object with about one Solar mass and a radius of ~ 10 km. The matter density in neutron stars is about the same as that in atomic nuclei.

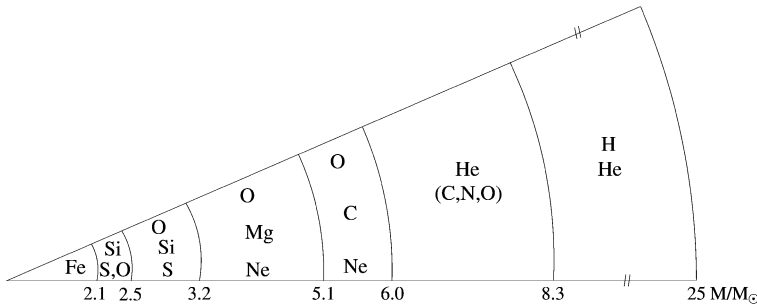


Fig. 2.10. Chemical shell structure of a massive star at the end of its life. The elements that have been formed in the various stages of the nuclear burning are ordered in a structure resembling that of an onion. This is the initial condition for a supernova explosion

involved, where successive nuclei in this chain are obtained by adding an α -particle (or ${}^4\text{He}$ -nucleus), i.e., two protons and two neutrons. Such elements are therefore called α -elements. The dominance of α -elements in the chemical abundance of the interstellar medium is thus a clear indication of nuclear fusion occurring in the He-rich zones of stars where the hydrogen has been burnt.

Supernovae Type Ia. SNe Ia are most likely the explosions of white dwarfs (WDs). These compact stars which form the final evolutionary stages of less massive stars no longer maintain their internal pressure by nuclear fusion. Rather, they are stabilized by the degeneracy pressure of the electrons – a quantum mechanical phenomenon. Such a white dwarf can only be stable if its mass does not exceed a limiting mass, the *Chandrasekhar mass*; it has a value of $M_{\text{Ch}} \approx 1.44M_{\odot}$. For $M > M_{\text{Ch}}$, the degeneracy pressure can no longer balance the gravitational force. If matter falls onto a WD with mass below M_{Ch} , as may happen by accretion in close binary systems, its mass will slowly increase and approach the limiting mass. At about $M \approx 1.3M_{\odot}$, carbon burning will ignite in its interior, transforming about half of the star into iron-group elements, i.e., iron, cobalt, and nickel. The resulting explosion of the star will enrich the ISM with $\sim 0.6M_{\odot}$ of Fe, while the WD itself will be torn apart completely, leaving no remnant star.

Since the initial conditions are probably very homogeneous for the class of SNe Ia (defined by the limiting mass prior to the trigger of the explosion), they are good candidates for *standard candles*: all SNe Ia have approximately the same luminosity. As we will discuss later (see Sect. 8.3.1), this is not really the case, but nevertheless SNe Ia play an important role in the cosmological

distance determination, and thus in the determination of cosmological parameters.

This interpretation of the different types of SNe explains why one finds core-collapse SNe only in galaxies in which star formation occurs. They are the final stages of massive, i.e., young, stars which have a lifetime of not more than 2×10^7 yr. By contrast, SNe Ia can occur in all types of galaxies.

In addition to SNe, metal enrichment of the interstellar medium (ISM) also takes place in other stages of stellar evolution, by stellar winds or during phases in which stars eject part of their envelope which is then visible, e.g., as a planetary nebula. If the matter in the star has been mixed by convection prior to such a phase, so that the metals newly formed by nuclear fusion in the interior have been transported towards the surface of the star, these metals will then be released into the ISM.

Age–Metallicity Relation. Assuming that at the beginning of its evolution the Milky Way had a chemical composition with only low metal content, the metallicity should be strongly related to the age of a stellar population. With each new generation of stars, more metals are produced and ejected into the ISM, partially by stellar winds, but mainly by SN explosions. Stars that are formed later should therefore have a higher metal content than those that were formed in the early phase of the Galaxy. One would therefore expect that a relation should exist between the age of a star and its metallicity.

For instance, under this assumption $[\text{Fe}/\text{H}]$ can be used as an age indicator for a stellar population, with the iron predominantly being produced and ejected in SNe of type Ia. Therefore, newly formed stars have a higher fraction of iron when they are born than their predecessors, and the youngest stars should have the highest

iron abundance. Indeed one finds $[\text{Fe}/\text{H}] = -4.5$ for extremely old stars (i.e., 3×10^{-5} of the Solar iron abundance), whereas very young stars have $[\text{Fe}/\text{H}] = 1$, so their metallicity can significantly exceed that of the Sun.

However, this age–metallicity relation is not very tight. On the one hand, SNe Ia occur only $\gtrsim 10^9$ years after the formation of a stellar population. The exact time-span is not known because even if one accepts the scenario for SN Ia described above, it is unclear in what form and in what systems the accretion of material onto the white dwarf takes place and how long it typically takes until the limiting mass is reached. On the other hand, the mixing of the SN ejecta in the ISM occurs only locally, so that large inhomogeneities of the $[\text{Fe}/\text{H}]$ ratio may be present in the ISM, and thus even for stars of the same age. An alternative measure for metallicity is $[\text{O}/\text{H}]$, because oxygen, which is an α -element, is produced and ejected mainly in supernova explosions of massive stars. These begin only $\sim 10^7$ yr after the formation of a stellar population, which is virtually instantaneous.

Characteristic values for the metallicity are $-0.5 \lesssim [\text{Fe}/\text{H}] \lesssim 0.3$ in the thin disk, while for the thick disk $-1.0 \lesssim [\text{Fe}/\text{H}] \lesssim -0.4$ is typical. From this, one can deduce that stars in the thin disk must be significantly younger on average than those in the thick disk. This result can now be interpreted using the age–metallicity relation. Either star formation has started earlier, or ceased earlier, in the thick disk than in the thin disk, or stars that originally belonged to the thin disk have migrated into the thick disk. The second alternative is favored for various reasons. It would be hard to understand why molecular gas, out of which stars are formed, was much more broadly distributed in earlier times than it is today, where we find it well concentrated near the Galactic plane. In addition, the widening of an initially narrow stellar distribution in time is also expected. The matter distribution in the disk is not homogeneous and, along their orbits around the Galactic center, stars experience this inhomogeneous gravitational field caused by other stars, spiral arms, and massive molecular clouds. Stellar orbits are perturbed by such fluctuations, i.e., they gain a random velocity component perpendicular to the disk from local inhomogeneities of the gravitational field. In other words, the velocity dispersion σ_z of a stellar population grows in time, and the scale-height of a population increases. In contrast to stars, the gas

keeps its narrow distribution around the Galactic plane due to internal friction.

This interpretation is, however, not unambiguous. Another scenario for the formation of the thick disk is also possible, where the stars of the thick disk were formed outside the Milky Way and only became constituents of the disk later, through accretion of satellite galaxies. This model is supported, among other reasons, by the fact that the rotational velocity of the thick disk around the Galactic center is smaller by ~ 50 km/s than that of the thin disk. In other spirals, in which a thick disk component was found and kinematically analyzed, the discrepancy between the rotation curves of the thick and thin disks is sometimes even stronger. In one case, the thick disk has been observed to rotate around the center of the galaxy in the opposite direction to the gas disk. In such a case, the aforementioned model of the evolution of the thick disk by kinematic heating of stars would definitely not apply.

Mass-to-Light Ratio. The total stellar mass of the thin disk is $\sim 6 \times 10^{10} M_\odot$, to which $\sim 0.5 \times 10^{10} M_\odot$ in the form of dust and gas has to be added. The luminosity of the stars in the thin disk is $L_B \approx 1.8 \times 10^{10} L_\odot$. Together, this yields a mass-to-light ratio of

$$\boxed{\frac{M}{L_B} \approx 3 \frac{M_\odot}{L_\odot} \quad \text{in thin disk}} \quad . \quad (2.36)$$

The M/L ratio in the thick disk is higher. For this component, one has $M \sim 3 \times 10^9 M_\odot$ and $L_B \approx 2 \times 10^8 L_\odot$, so that $M/L_B \sim 15$ in Solar units. The thick disk thus does not play any significant role for the total mass budget of the Galactic disk, and even less for its total luminosity. On the other hand, the thick disk is invaluable for the diagnosis of the dynamical evolution of the disk. If the Milky Way were to be observed from the outside, one would find a M/L value for the disk of about 4 in Solar units; this is a characteristic value for spiral galaxies.

2.3.3 The Galactic Disk: Dust and Gas

The spiral structure of the Milky Way and other spiral galaxies is delineated by very young objects like O- and

B-stars and HII regions.⁷ This is the reason why spiral arms appear blue. Obviously, star formation in our Milky Way takes place mainly in the spiral arms. Here, the molecular clouds – gas clouds which are sufficiently dense and cool for molecules to form in large abundance – contract under their own gravity and form new stars. The spiral arms are much less prominent in red light. Emission in the red is dominated by an older stellar population, and these old stars have had time to move away from the spiral arms. The Sun is located close to, but not in, a spiral arm – the so-called Orion arm.

Observing the gas in the Galaxy is made possible mainly by the 21-cm line emission of HI (neutral atomic hydrogen) and by the emission of CO, the second-most abundant molecule after H₂ (molecular hydrogen). H₂ is a symmetric molecule and thus has no electric dipole moment, which is the reason why it does not radiate strongly. In most cases it is assumed that the ratio of CO to H₂ is a universal constant (called the “X-factor”). Under this assumption, the distribution of CO can be converted into that of the molecular gas. The Milky Way is optically thin at 21 cm, i.e., 21-cm radiation is not absorbed along its path from the source to the observer. With radio-astronomical methods it is thus possible to observe atomic gas throughout the entire Galaxy.

To examine the distribution of dust, two options are available. First, dust is detected by the extinction it causes. This effect can be analyzed quantitatively, for instance by star counts or by investigating the reddening of stars (an example of this can be seen in Fig. 2.7). Second, dust emits thermal radiation observable in the FIR part of the spectrum, which was mapped by several satellites such as IRAS and COBE. By combining the sky maps of these two satellites at different frequencies the Galactic distribution of dust was determined. The dust temperature varies in a relatively narrow range between ~ 17 K and ~ 21 K, but even across this small range, the dust emission varies, for fixed column density, by a factor ~ 5 at a wavelength of $100 \mu\text{m}$. Therefore, one needs to combine maps at different frequencies in order to determine column densities and temperatures. In addition, the zodiacal light caused by the reflection of solar radiation by dust inside our Solar system has to be subtracted

before the Galactic FIR emission can be analyzed. This is possible with multifrequency data because of the different spectral shapes. The resulting distribution of dust is displayed in Fig. 2.11. It shows the concentration of dust around the Galactic plane, as well as large-scale anisotropies at high Galactic latitudes. The dust map shown here is routinely used for extinction correction when observing extragalactic sources.

Besides a strong concentration towards the Galactic plane, gas and dust are preferentially found in spiral arms where they serve as raw material for star formation. Molecular hydrogen (H₂) and dust are generally found at $3 \text{ kpc} \lesssim R \lesssim 8 \text{ kpc}$, within $|z| \lesssim 90 \text{ pc}$ of both sides of the Galactic plane. In contrast, the distribution of atomic hydrogen (HI) is observed out to much larger distances from the Galactic center ($R \lesssim 25 \text{ kpc}$), with a scale-height of $\sim 160 \text{ pc}$ inside the Solar orbit, $R \lesssim R_0$. At larger distances from the Galactic center, $R \gtrsim 12 \text{ kpc}$, the scale-height increases substantially to $\sim 1 \text{ kpc}$. The gaseous disk is warped at these large radii though the origin of this warp is unclear. For example, it may be caused by the gravitational field of the Magellanic Clouds. The total mass in the two components of hydrogen is about $M(\text{HI}) \approx 4 \times 10^9 M_\odot$ and $M(\text{H}_2) \approx 10^9 M_\odot$, respectively, i.e., the gas mass in our Galaxy is less than $\sim 10\%$ of the stellar mass. The density of the gas in the Solar neighborhood is about $\rho(\text{gas}) \sim 0.04 M_\odot/\text{pc}^3$.

2.3.4 Cosmic Rays

The Magnetic Field of the Galaxy. Like many other cosmic objects, the Milky Way has a magnetic field. The properties of this field can be analyzed using a variety of methods and we list some of them in the following.

- Polarization of stellar light. The light of distant stars is partially polarized, with the degree of polarization being strongly related to the extinction, or reddening, of the star. This hints at the polarization being linked to the dust causing the extinction. The light scattered by dust particles is partially linearly polarized, with the direction of polarization depending on the alignment of the dust grains. If their orientation were random, the superposition of the scattered radiation from different dust particles would add up to a vanishing net polarization. However, a net polarization

⁷HII regions are nearly spherical regions of fully ionized hydrogen (thus the name HII region) surrounding a young hot star which photoionizes the gas. They emit strong emission lines of which the Balmer lines of hydrogen are strongest.

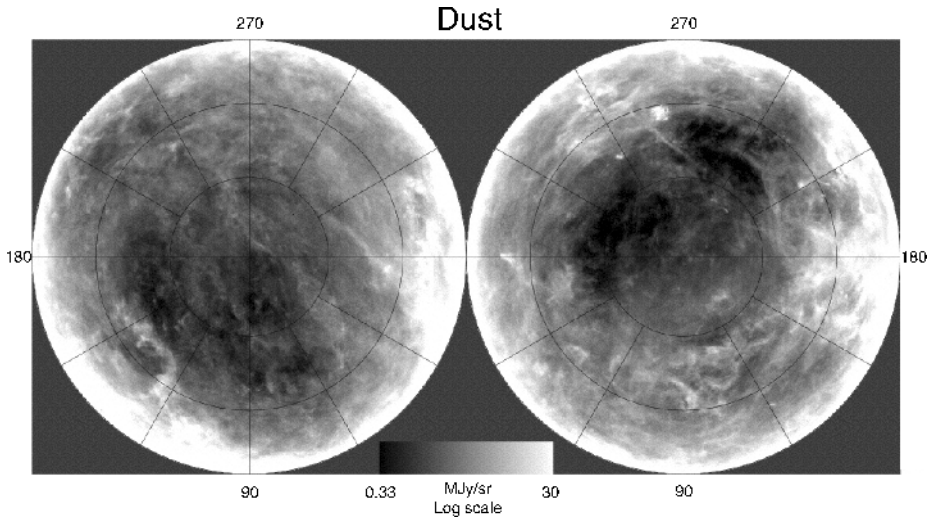


Fig. 2.11. Distribution of dust in the Galaxy, derived from a combination of IRAS and COBE sky maps. The northern Galactic sky in Galactic coordinates is displayed on the left, the southern on the right. We can clearly see the concentra-

tion of dust towards the Galactic plane, as well as regions with a very low column density of dust; these regions in the sky are particularly well suited for very deep extragalactic observations

is measured, so the orientation of dust particles cannot be random, rather it must be coherent on large scales. Such a coherent alignment is provided by a large-scale magnetic field, whereby the orientation of dust particles, measurable from the polarization direction, indicates the (projected) direction of the magnetic field.

- The Zeeman effect. The energy levels in an atom change if the atom is placed in a magnetic field. Of particular importance in the present context is the fact that the 21-cm transition line of neutral hydrogen is split in a magnetic field. Because the amplitude of the line split is proportional to the strength of the magnetic field, the field strength can be determined from observations of this Zeeman effect.
- Synchrotron radiation. When relativistic electrons move in a magnetic field they are subject to the Lorentz force. The corresponding acceleration is perpendicular both to the velocity vector of the particles and to the magnetic field vector. As a result, the electrons follow a helical (i.e., corkscrew) track, which is a superposition of circular orbits perpendicular to the field lines and a linear motion along the field. Since accelerated charges emit electromagnetic radiation, this helical movement is the source of the so-called synchrotron radiation (which will be discussed in

more detail in Sect. 5.1.2). This radiation, which is observable at radio frequencies, is linearly polarized, with the direction of the polarization depending on the direction of the magnetic field.

- Faraday rotation. If polarized radiation passes through a magnetized plasma, the direction of the polarization rotates. The rotation angle depends quadratically on the wavelength of the radiation,

$$\Delta\theta = RM\lambda^2. \quad (2.37)$$

The *rotation measure* RM is the integral along the line-of-sight towards the source over the electron density and the component B_{\parallel} of the magnetic field in direction of the line-of-sight,

$$RM = 81 \frac{\text{rad}}{\text{cm}^2} \int_0^D \frac{d\ell}{\text{pc}} \frac{n_e}{\text{cm}^{-3}} \frac{B_{\parallel}}{\text{G}}. \quad (2.38)$$

The dependence of the rotation angle (2.37) on λ allows us to determine the rotation measure RM, and thus to estimate the product of electron density and magnetic field. If the former is known, one immediately gets information about B . By measuring the RM for sources in different directions and at different distances the magnetic field of the Galaxy can be mapped.

From applying the methods discussed above, we know that a magnetic field exists in the disk of our Milky Way. This field has a strength of about 4×10^{-6} G and mainly follows the spiral arms.

Cosmic Rays. We obtain most of the information about our Universe from the electromagnetic radiation that we observe. However, we receive an additional radiation component, the energetic cosmic rays. They consist primarily of electrically charged particles, mainly electrons and nuclei. In addition to the particle radiation that is produced in energetic processes at the Solar surface, a much more energetic cosmic ray component exists that can only originate in sources outside the Solar system.

The energy spectrum of the cosmic rays is, to a good approximation, a power law: the flux of particles with energy larger than E can be written as $S(> E) \propto E^{-q}$, with $q \approx 1.7$. However, the slope of the spectrum changes slightly, but significantly, at some energy scales: at $E \sim 10^{15}$ eV the spectrum becomes steeper, and at $E \gtrsim 10^{18}$ eV it flattens again.⁸ Measurements of the spectrum at these high energies are rather uncertain, however, because of the strongly decreasing flux with increasing energy. This implies that only very few particles are detected.

Cosmic Ray Acceleration and Confinement. To accelerate particles to such high energies, highly energetic processes are necessary. For energies below 10^{15} eV, very convincing arguments suggest SN remnants as the sites of the acceleration. The SN explosion drives a shock front⁹ into the ISM with an initial velocity of $\sim 10\,000$ km/s. Plasma processes in a shock front can accelerate some particles to very high energies. The theory of this diffuse shock acceleration predicts that

the resulting energy spectrum of the particles follows a power law, the slope of which depends only on the strength of the shock (i.e., the ratio of the densities on both sides of the shock front). This power law agrees very well with the slope of the observed cosmic ray spectrum, if additional propagation processes in the Milky Way are taken into account. The presence of very energetic electrons in SN remnants is observed directly by their synchrotron emission, so that the slope of the produced spectrum is also directly observable.

Accelerated particles then propagate through the Galaxy where, due to the magnetic field, they move along complicated helical tracks. Therefore, the direction from which a particle arrives at Earth cannot be identified with the direction to its source of origin. The magnetic field is also the reason why particles do not leave the Milky Way along a straight path, but instead are stored for a long time ($\sim 10^7$ yr) before they eventually diffuse out, an effect also called confinement.

The sources of the particles with energy between $\sim 10^{15}$ eV and $\sim 10^{18}$ eV are likewise presumed to be located inside our Milky Way, because the magnetic field is sufficiently strong to confine them in the Galaxy. However, SN remnants are not likely sources for particles at these energies; in fact, the origin of these rays is largely unknown. Particles with energies larger than $\sim 10^{18}$ eV are probably of extragalactic origin. The radius of the helical tracks in the magnetic field of the Galaxy, i.e., their Larmor radius, is larger than the radius of the Milky Way itself, so they cannot be confined. Their origin is also unknown, but AGNs are the most probable source of these particles. Finally, one of the largest puzzles of high-energy astrophysics is the origin of cosmic rays with $E \gtrsim 10^{19}$ eV. The energy of these particles is so large that they are able to interact with the cosmic microwave background to produce pions and other particles, losing much of their energy in this process. These particles cannot propagate much further than ~ 10 Mpc through the Universe before they lose most of their energy. This implies that their acceleration sites should be located in the close vicinity of the Milky Way. Since the curvature of the orbits of such highly energetic particles is very small, it should, in principle, be possible to identify their origin: there are not many AGNs within 10 Mpc that are promising candidates for the origin of these ultra-high-energy cosmic rays. However, the observed number of these particles

⁸These energies should be compared with those reached in particle accelerators: LEP at CERN reached ~ 100 GeV = 10^{11} eV. Hence, cosmic accelerators are much more efficient than man-made machines.

⁹Shock fronts are surfaces in a gas flow where the parameters of state for the gas, such as pressure, density, and temperature, change discontinuously. The standard example for a shock front is the bang in an explosion, where a spherical shock wave propagates outwards from the point of explosion. Another example is the sonic boom caused, for example, by airplanes that move at a speed exceeding the velocity of sound. Such shock fronts are solutions of the hydrodynamic equations. They occur frequently in astrophysics, e.g., in explosion phenomena such as supernovae or in rapid (i.e., supersonic) flows such as those we will discuss in the context of AGNs.

is so small that no reliable information on these sources has thus far been obtained.

Energy Density. It is interesting to realize that the energy densities of cosmic rays, the magnetic field, the turbulent energy of the ISM, and the electromagnetic radiation of the stars are about the same – as if an equilibrium between these different components has been established. Since these components interact with each other – e.g., the turbulent motions of the ISM can amplify the magnetic field, and vice versa, the magnetic field affects the velocity of the ISM and of cosmic rays – it is not improbable that these interaction processes can establish an equipartition of the energy densities.

Gamma Radiation from the Milky Way. The Milky Way emits γ -radiation, as can be seen in Fig. 1.5. There is diffuse γ -ray emission which can be traced back to the cosmic rays in the Galaxy. When these energetic particles collide with nuclei in the interstellar medium, radiation is released. This gives rise to a continuum radiation which closely follows a power-law spectrum, such that the observed flux S_ν is $\propto \nu^{-\alpha}$, with $\alpha \sim 2$. The quantitative analysis of the distribution of this emission provides the most important information about the spatial distribution of cosmic rays in the Milky Way.

Gamma-Ray Lines. In addition to the continuum radiation, one also observes line radiation in γ -rays, at energies below ~ 10 MeV. The first detected and most prominent line has an energy of 1.809 MeV and corresponds to a radioactive decay of the Al^{26} nucleus. The spatial distribution of this emission is strongly concentrated towards the Galactic disk and thus follows the young stellar population in the Milky Way. Since the lifetime of the Al^{26} nucleus is short ($\sim 10^6$ yr), it must be produced near the emission site, which then implies that it is produced by the young stellar population. It is formed in hot stars and released to the interstellar medium either through stellar winds or core-collapse supernovae. Gamma lines from other radioactive nuclei have been detected as well.

Annihilation Radiation from the Galaxy. Furthermore, line radiation with an energy of 511 keV has been detected in the Galaxy. This line is produced when an electron and a positron annihilate into two photons, each

with an energy corresponding to the rest-mass energy of an electron, i.e., 511 keV.¹⁰ This annihilation radiation was identified first in the 1970s. With the Integral satellite, its emission morphology has been mapped with an angular resolution of $\sim 3^\circ$. The 511 keV line emission is detected both from the Galactic disk and the bulge. The angular resolution is not sufficient to tell whether the annihilation line traces the young stellar population (i.e., the thin disk) or the older population in the thick disk. However, one can compare the distribution of the annihilation radiation with that of Al^{26} and other radioactive species. In about 85% of all decays Al^{26} emits a positron. If this positron annihilates close to its production site one can predict the expected annihilation radiation from the distribution of the 1.809 MeV line. In fact, the intensity and angular distribution of the 511 keV line from the disk is compatible with this scenario for the generation of positrons.

The origin of the annihilation radiation from the bulge, which has a luminosity larger than that from the disk by a factor ~ 5 , is unknown. One needs to find a plausible source for the production of positrons in the bulge. There is no unique answer to this problem at present, but Type Ia supernovae and energetic processes near low-mass X-ray binaries are prime candidates for this source.

2.3.5 The Galactic Bulge

The Galactic bulge is the central thickening of our Galaxy. Figure 1.2 shows another spiral galaxy from its side, with its bulge clearly visible. The characteristic scale-length of the bulge is ~ 1 kpc. Owing to the strong extinction in the disk, the bulge is best observed in the IR, for instance with the IRAS and COBE satellites. The extinction to the Galactic Center in the visual is $A_V \sim 28$ mag. However, some lines-of-sight close to the Galactic center exist where A_V is significantly smaller, so that observations in optical and near IR light are possible, e.g., in Baade's window, located about 4° below the Galactic center at $\ell \sim 1^\circ$, for which $A_V \sim 2$ mag (also see Sect. 2.6).

From the observations by COBE, and also from Galactic microlensing experiments (see Sect. 2.5), we know

¹⁰ In addition to the two-photon annihilation, there is also an annihilation channel in which three photons are produced; the corresponding radiation forms a continuum spectrum, i.e., no spectral lines.

that our bulge has the shape of a bar, with the major axis pointing away from us by about 30° . The scale-height of the bulge is ~ 400 pc, with an axis ratio of ~ 0.6 .

As is the case for the exponential profiles that describe the light distribution in the disk, the functional form of the brightness distribution in the bulge is also suggested from observations of other spiral galaxies. The profiles of their bulges, observed from the outside, are much better determined than in our Galaxy where we are located amid its stars.

The de Vaucouleurs Profile. The brightness profile of our bulge can be approximated by the de Vaucouleurs law which describes the surface brightness I as a function of the distance R from the center,

$$\log\left(\frac{I(R)}{I_e}\right) = -3.3307 \left[\left(\frac{R}{R_e}\right)^{1/4} - 1 \right], \quad (2.39)$$

with $I(R)$ being the measured surface brightness, e.g., in $[I] = L_\odot/\text{pc}^2$. R_e is the effective radius, defined such that half of the luminosity is emitted from within R_e ,

$$\int_0^{R_e} dR R I(R) = \frac{1}{2} \int_0^\infty dR R I(R). \quad (2.40)$$

This definition of R_e also leads to the numerical factor on the right-hand side of (2.39). As one can easily see from (2.39), $I_e = I(R_e)$ is the surface brightness at the effective radius. An alternative form of the de Vaucouleurs law is

$$I(R) = I_e \exp\left(-7.669 \left[(R/R_e)^{1/4} - 1\right]\right). \quad (2.41)$$

Because of its mathematical form, it is also called an $r^{1/4}$ law. The $r^{1/4}$ law falls off significantly more slowly than an exponential law for large R . For the Galactic bulge, one finds an effective radius of $R_e \approx 0.7$ kpc. With the de Vaucouleurs profile, a relation between luminosity, effective radius, and surface brightness is obtained by integrating over the surface brightness,

$$L = \int_0^\infty dR 2\pi R I(R) = 7.215\pi I_e R_e^2. \quad (2.42)$$

Stellar Age Distribution in the Bulge. The stars in the bulge cover a large range in metallicity, $-1 \lesssim [\text{Fe}/\text{H}] \lesssim +1$, with a mean of about 0.3, i.e., the mean metallicity is about twice that of the Sun. This high metallicity hints at a contribution by a rather young population, whereas the color of the bulge stars points towards a predominantly old stellar population. The bulge also contains about $10^8 M_\odot$ in molecular gas. On the other hand, one finds very metal-poor RR Lyrae stars, i.e., old stars. However, the distinction in membership between bulge and disk stars is not easy, so it is possible that the young component may actually be part of the inner disk.

The mass of the bulge is about $M_{\text{bulge}} \sim 10^{10} M_\odot$ and its luminosity is $L_{B,\text{bulge}} \sim 3 \times 10^9 L_\odot$, which results in a mass-to-light ratio of

$$\frac{M}{L} \approx 3 \frac{M_\odot}{L_\odot} \quad \text{in the bulge}, \quad (2.43)$$

very similar to that of the thin disk.

2.3.6 The Visible Halo

The visible halo of our Galaxy consists of about 150 *globular clusters* and field stars with a high velocity component perpendicular to the Galactic plane. A globular cluster is a collection of typically several hundred thousand stars, contained within a spherical region of radius ~ 20 pc. The stars in the cluster are gravitationally bound and orbit in the common gravitational field. The old globular clusters with $[\text{Fe}/\text{H}] < -0.8$ have an approximately spherical distribution around the Galactic center. A second population of globular clusters exists that contains younger stars with a higher metallicity, $[\text{Fe}/\text{H}] > -0.8$. They have a more oblate geometrical distribution and are possibly part of the thick disk because they show roughly the same scale-height.

Most globular clusters are at a distance of $r \lesssim 35$ kpc (with $r = \sqrt{R^2 + z^2}$) from the Galactic center, but some are also found at $r > 60$ kpc. At these distances it is hard to judge whether these objects are part of the Galaxy or whether they have been captured from a neighboring galaxy, such as the Magellanic Clouds. Also, field stars have been found at distances out to $r \sim 50$ kpc, which is the reason why one assumes a characteristic value of $r_{\text{halo}} \sim 50$ kpc for the extent of the visible halo.

The *density distribution* of metal-poor globular clusters and field stars in the halo is described by

$$n(r) \propto r^{-3.5}. \quad (2.44)$$

Alternatively, one can fit a de Vaucouleurs profile to the density distribution, which results in an effective radius of $r_e \sim 2.7$ kpc.

At large distances from the disk, neutral hydrogen is also found, in the form of clouds. Most of these clouds, visible in 21-cm line emission, have a negative radial velocity, i.e., they are moving towards us, with velocities of up to $v_r \sim -400$ km/s. These *high-velocity clouds* (HVCs) cannot be following the general Galactic rotation. We have virtually no means of determining the distances of these clouds, and thus their origin and nature are still subject to discussion. There is one exception, however: the Magellanic Stream is a narrow band of HI emission which follows the Magellanic Clouds along their orbit around the Galaxy (also see Fig. 6.6). This gas stream may be the result of a close encounter of the Magellanic Clouds with the Milky Way in the past. The (tidal) gravitational force that the Milky Way had imposed on our neighboring galaxies in such an encounter could strip away part of the interstellar gas from them.

2.3.7 The Distance to the Galactic Center

As already mentioned, our distance from the Galactic center is rather difficult to measure and thus not very precisely known. The general problem with such a measurement is the high extinction in the disk, prohibiting measurements of the distance of individual stars close to the Galactic center. Thus, one has to rely on more indirect methods, and the most important ones will be outlined here.

The visible halo of our Milky Way is populated by globular clusters and also by field stars. They have a spherical, or, more generally, a spheroidal distribution. The center of this distribution is obviously the center of gravity of the Milky Way, around which the halo objects are moving. If one measures the three-dimensional distribution of the halo population, the geometrical center of this distribution should correspond to the Galactic center.

This method can indeed be applied because, due to their extended distribution, halo objects can be observed

at relatively large Galactic latitudes where they are not too strongly affected by extinction. As was discussed in Sect. 2.2, the distance determination of globular clusters is possible using photometric methods. On the other hand, one also finds RR Lyrae stars in globular clusters to which the period–luminosity relation can be applied. Therefore, the spatial distribution of the globular clusters can be determined. However, at about 150, the number of known globular clusters is relatively small, resulting in a fairly large statistical error for the determination of the common center. Much more numerous are the RR Lyrae field stars in the halo, for which distances can be measured using the period–luminosity relation. The statistical error in determining the center of their distribution is therefore much smaller. On the other hand, this distance to the Galactic center is based only on the calibration of the period–luminosity relation, and any uncertainty in this will propagate into a systematic error on R_0 . Effects of the extinction add to this. However, such effects can be minimized by observing the RR Lyrae stars in the NIR, which in addition benefits from the narrower luminosity distribution of RR Lyrae stars in this wavelength regime. These analyses yield a value of $R_0 \approx 8.0$ kpc (see Fig. 2.12).

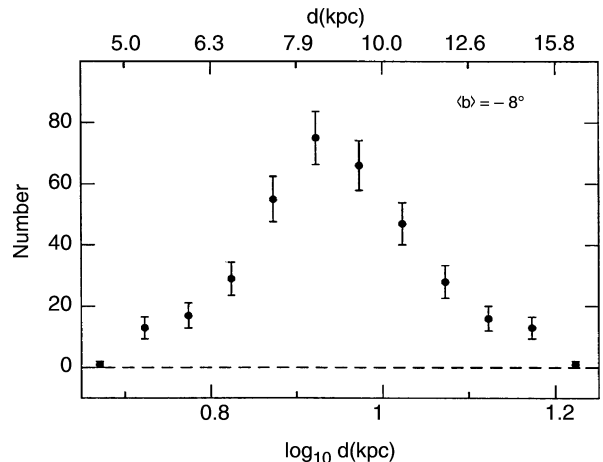


Fig. 2.12. The number of RR Lyrae stars as a function of distance, measured in a direction that closely passes the Galactic center, at $\ell = 0^\circ$ and $b = -8^\circ$. If we assume a spherically symmetric distribution of the RR Lyrae stars, concentrated towards the center, the distance to the Galactic center can be identified with the maximum of this distribution

2.4 Kinematics of the Galaxy

Unlike a solid body, the Galaxy rotates differentially. This means that the angular velocity is a function of the distance R from the Galactic center. Seen from above, i.e., from the NGP, the rotation is clockwise. To describe the velocity field quantitatively we will in the following introduce velocity components in the coordinate system (R, θ, z) , as shown in Fig. 2.13. An object following a track $[R(t), \theta(t), z(t)]$ then has the velocity components

$$U := \frac{dR}{dt}, \quad V := R \frac{d\theta}{dt}, \quad W := \frac{dz}{dt}. \quad (2.45)$$

For example, the Sun is not moving on a simple circular orbit around the Galactic center, but currently inwards, $U < 0$, and with $W > 0$, so that it is moving away from the Galactic plane.

In this section we will examine the rotation of the Milky Way. We start with the determination of the velocity components of the Sun. Then we will consider the rotation curve of the Galaxy, which describes the rotational velocity $V(R)$ as a function of the distance R from the Galactic center. We will find the intriguing result that the velocity V does not decline towards large distances, but that it virtually remains constant. Because this result is of extraordinary importance, we will discuss the methods needed to derive it in some detail.

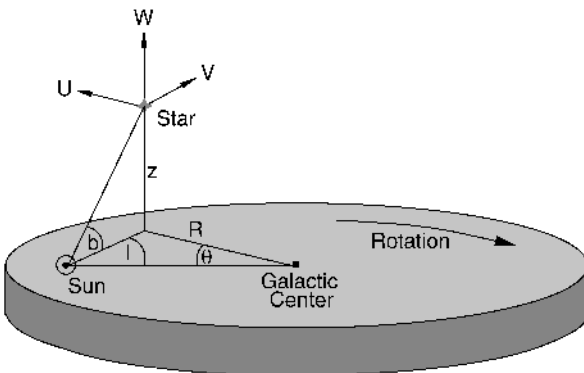


Fig. 2.13. Cylindrical coordinate system (R, θ, z) with the Galactic center at its origin. Note that θ increases in the clockwise direction if the disk is viewed from above. The corresponding velocity components (U, V, W) of a star are indicated

2.4.1 Determination of the Velocity of the Sun

Local Standard of Rest. To link local measurements to the Galactic coordinate system (R, θ, z) , the *local standard of rest* is defined. It is a fictitious rest-frame in which velocities are measured. For this purpose, we consider a point that is located today at the position of the Sun and that moves along a perfectly circular orbit in the plane of the Galactic disk. The velocity components in the LSR are then by definition,

$$U_{\text{LSR}} \equiv 0, \quad V_{\text{LSR}} \equiv V_0, \quad W_{\text{LSR}} \equiv 0, \quad (2.46)$$

with $V_0 \equiv V(R_0)$ being the orbital velocity at the location of the Sun. Although the LSR changes over time, the time-scale of this change is so large (the orbital period is $\sim 230 \times 10^6$ yr) that this effect is negligible.

Peculiar Velocity. The velocity of an object relative to the LSR is called its peculiar velocity. It is denoted by \mathbf{v} , and its components are given as

$$\mathbf{v} \equiv (u, v, w) = (U - U_{\text{LSR}}, V - V_{\text{LSR}}, W - W_{\text{LSR}}) \\ = (U, V - V_0, W) \quad (2.47)$$

The velocity of the Sun relative to the LSR is denoted by \mathbf{v}_\odot . If \mathbf{v}_\odot is known, any velocity measured relative to the Sun can be converted into a velocity relative to the LSR: let $\Delta \mathbf{v}$ be the velocity of a star relative to the Sun, which is directly measurable using the methods discussed in Sect. 2.2, then the peculiar velocity of this star is

$$\mathbf{v} = \mathbf{v}_\odot + \Delta \mathbf{v}. \quad (2.48)$$

Peculiar Velocity of the Sun. We consider now an ensemble of stars in the immediate vicinity of the Sun, and assume the Galaxy to be axially symmetric and stationary. Under these assumptions, the number of stars that move outwards to larger radii R equals the number of stars moving inwards. Likewise, as many stars move upwards through the Galactic plane as downwards. If these conditions are not satisfied, the assumption of a stationary distribution would be violated. The mean values of the corresponding peculiar velocity components must therefore vanish,

$$\langle u \rangle = 0, \quad \langle w \rangle = 0, \quad (2.49)$$

where the brackets denote an average over the ensemble considered. The analog argument is not valid for the v component because the mean value of v depends on the distribution of the orbits: if only circular orbits in the disk existed, we would also have $\langle v \rangle = 0$ (this is trivial, since then all stars would have $v = 0$), but this is not the case. From a statistical consideration of the orbits in the framework of stellar dynamics, one deduces that $\langle v \rangle$ is closely linked to the radial velocity dispersion of the stars: the larger it is, the more $\langle v \rangle$ deviates from zero. One finds that

$$\langle v \rangle = -C \langle u^2 \rangle, \quad (2.50)$$

where C is a positive constant that depends on the density distribution and on the local velocity distribution of the stars. The sign in (2.50) follows from noting that a circular orbit has a higher tangential velocity than elliptical orbits, which in addition have a non-zero radial component. Equation (2.50) expresses the fact that the mean rotational velocity of a stellar population around the Galactic center deviates from the corresponding circular orbit velocity, and that the deviation is stronger for a larger radial velocity dispersion. This phenomenon is also known as asymmetric drift. From the mean of (2.48) over the ensemble considered and by using (2.49) and (2.50), one obtains

$$\mathbf{v}_{\odot} = (-\langle \Delta u \rangle, -C \langle u^2 \rangle - \langle \Delta v \rangle, -\langle \Delta w \rangle). \quad (2.51)$$

One still needs to determine the constant C in order to make use of this relation. This is done by considering different stellar populations and measuring $\langle u^2 \rangle$ and $\langle \Delta v \rangle$ separately for each of them. If these two quantities are then plotted in a diagram (see Fig. 2.14), a linear relation is obtained, as expected from (2.50). The slope C can be determined directly from this diagram. Furthermore, from the intersection with the $\langle \Delta v \rangle$ -axis, v_{\odot} is readily read off. The other velocity components in (2.51) follow by simply averaging, yielding the result:

$$\mathbf{v}_{\odot} = (-10, 5, 7) \text{ km/s}. \quad (2.52)$$

Hence, the Sun is currently moving inwards, upwards, and faster than it would on a circular orbit at its location. We have therefore determined \mathbf{v}_{\odot} , so we are now able to analyze any measured stellar velocities relative to the

LSR. However, we have not yet discussed how V_0 , the rotational velocity of the LSR itself, is determined.

Velocity Dispersion of Stars. The dispersion of the stellar velocities relative to the LSR can now be determined, i.e., the mean square deviation of their velocities from the velocity of the LSR. For young stars (A stars, for example), this dispersion happens to be small. For older K giants it is larger, and is larger still for old, metal-poor red dwarf stars. We observe a very well-defined velocity-metallicity relation. When this is combined with the age-metallicity relation it appears that the oldest stars have the highest peculiar velocities. This effect is observed in all three coordinates. This result is in agreement with the relation between the age of a stellar population and its scale-height (discussed in Sect. 2.3.1), the latter being linked to the velocity dispersion via σ_z .

Asymmetric Drift. If one considers high-velocity stars, only a few are found that have $v > 65$ km/s and which are thus moving much faster around the Galactic center than the LSR. However, quite a few stars are found that have $v < -250$ km/s, so their orbital velocity is opposite to the direction of rotation of the LSR. Plotted in a $(u - v)$ -diagram, a distribution is found which is narrowly concentrated around $u = 0$ km/s $= v$ for young stars, as already mentioned above, and which gets increasingly wider for older stars. For the oldest stars,

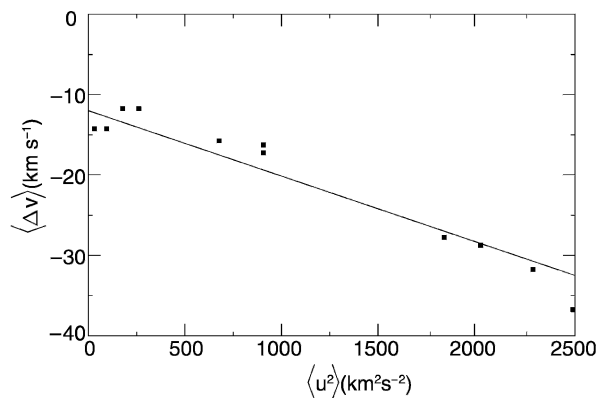


Fig. 2.14. The velocity components $\langle \Delta v \rangle = \langle v \rangle - v_{\odot}$ are plotted against $\langle u^2 \rangle$ for stars in the Solar neighborhood. Because of the linear relation, v_{\odot} can be read off from the intersection with the x -axis, and C from the slope

which belong to the halo population, one obtains a circular envelope with its center located at $u = 0$ km/s and $v \approx -220$ km/s (see Fig. 2.15). If we assume that the Galactic halo, to which these high-velocity stars belong, does not rotate (or only very slowly), this asymmetry in the v -distribution can only be caused by the rotation of the LSR. The center of the envelope then has to be at $-V_0$. This yields the orbital velocity of the LSR

$$V_0 \equiv V(R_0) = 220 \text{ km/s} . \quad (2.53)$$

Knowing this velocity, we can then compute the mass of the Galaxy inside the Solar orbit. A circular orbit is characterized by an equilibrium between centrifugal and gravitational acceleration, $V^2/R = GM(< R)/R^2$, so that

$$M(< R_0) = \frac{V_0^2 R_0}{G} = 8.8 \times 10^{10} M_\odot . \quad (2.54)$$

Furthermore, for the orbital period of the LSR, which is similar to that of the Sun, one obtains

$$P = \frac{2\pi R_0}{V_0} = 230 \times 10^6 \text{ yr} . \quad (2.55)$$

Hence, during the lifetime of the Solar System, estimated to be $\sim 4.6 \times 10^9$ yr, it has completed about 20 orbits around the Galactic center.

2.4.2 The Rotation Curve of the Galaxy

From observations of the velocity of stars or gas around the Galactic center, the rotational velocity V can be determined as a function of the distance R from the Galactic center. In this section, we will describe methods to determine this *rotation curve* and discuss the result.

We consider an object at distance R from the Galactic center which moves along a circular orbit in the Galactic plane, has a distance D from the Sun, and is located at a Galactic longitude ℓ (see Fig. 2.16). In a Cartesian coordinate system with the Galactic center at the origin, the positional and velocity vectors (we only consider the two components in the Galactic plane because we assume a motion in the plane) are given by

$$\mathbf{r} = R \begin{pmatrix} \sin \theta \\ \cos \theta \end{pmatrix}, \quad \mathbf{V} = \dot{\mathbf{r}} = V(R) \begin{pmatrix} \cos \theta \\ -\sin \theta \end{pmatrix},$$

where θ denotes the angle between the Sun and the object as seen from the Galactic center. From the geometry shown in Fig. 2.16 it follows that

$$\mathbf{r} = \begin{pmatrix} D \sin \ell \\ R_0 - D \cos \ell \end{pmatrix}.$$

If we now identify the two expressions for the components of \mathbf{r} , we obtain

$$\begin{aligned} \sin \theta &= (D/R) \sin \ell, \\ \cos \theta &= (R_0/R) - (D/R) \cos \ell. \end{aligned}$$

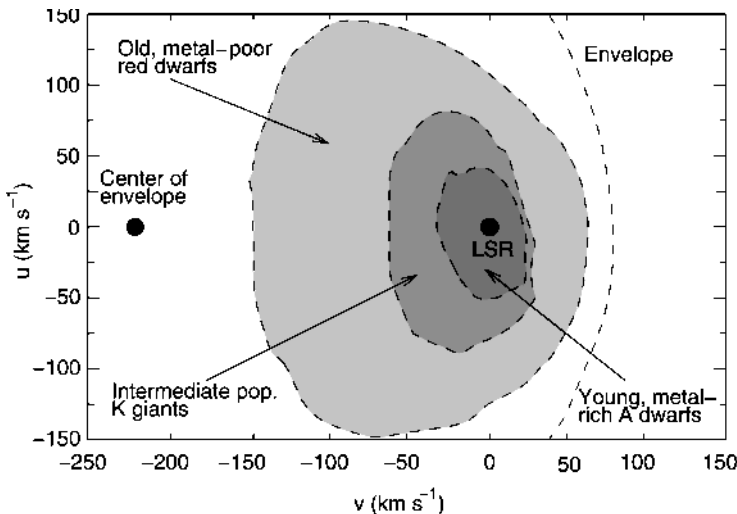


Fig. 2.15. The motion of the Sun around the Galactic center is reflected in the asymmetric drift: while young stars in the Solar vicinity have velocities very similar to the Solar velocity, i.e., small relative velocities, members of other populations (and of other Milky Way components) have different velocities – e.g., for halo objects $v = -220$ km/s on average. Thus, different velocity ellipses show up in a $(u - v)$ -diagram

If we disregard the difference between the velocities of the Sun and the LSR we get $\mathbf{V}_\odot \approx \mathbf{V}_{\text{LSR}} = (V_0, 0)$ in this coordinate system. Thus the relative velocity between the object and the Sun is, in Cartesian coordinates,

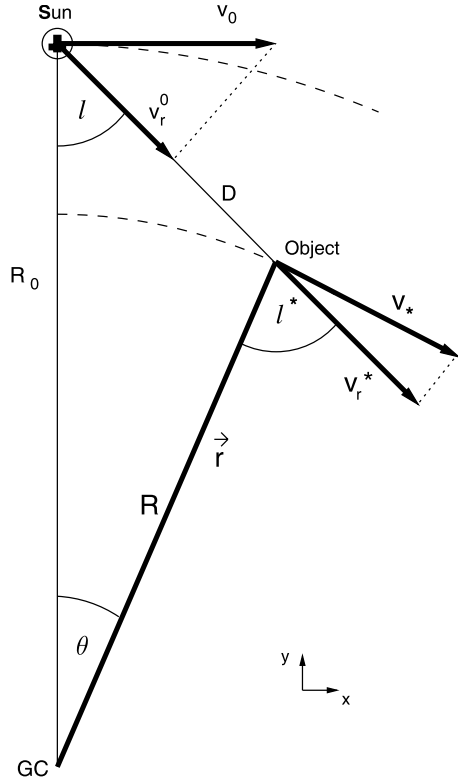


Fig. 2.16. Geometric derivation of the formalism of differential rotation:

$$\begin{aligned} v_r &= v_r^* - v_r^\odot = v_* \sin \ell^* - v_\odot \sin \ell, \\ v_t &= v_t^* - v_t^\odot = v_* \cos \ell^* - v_\odot \cos \ell. \end{aligned}$$

One has:

$$\begin{aligned} R \sin \theta &= D \sin \ell, \\ R \cos \theta + D \cos \ell &= R_0, \end{aligned}$$

which implies

$$\begin{aligned} v_r &= R_0 \left(\frac{v_*}{R} - \frac{v_\odot}{R_0} \right) \sin \ell \\ &= (\Omega - \Omega_0) R_0 \sin \ell, \\ v_t &= R_0 \left(\frac{v_*}{R} - \frac{v_\odot}{R_0} \right) \cos \ell - D \frac{v_*}{R} \\ &= (\Omega - \Omega_0) R_0 \cos \ell - \Omega D. \end{aligned}$$

$$\begin{aligned} \Delta \mathbf{V} &= \mathbf{V} - \mathbf{V}_\odot \\ &= \begin{pmatrix} V(R_0/R) - V(D/R) \cos \ell - V_0 \\ -V(D/R) \sin \ell \end{pmatrix}. \end{aligned}$$

With the angular velocity defined as

$$\Omega(R) = \frac{V(R)}{R}, \quad (2.56)$$

we obtain for the relative velocity

$$\Delta \mathbf{V} = \begin{pmatrix} R_0(\Omega - \Omega_0) - \Omega D \cos \ell \\ -D \Omega \sin \ell \end{pmatrix},$$

where $\Omega_0 = V_0/R_0$ is the angular velocity of the Sun. The radial and tangential velocities of this relative motion then follow by projection of $\Delta \mathbf{V}$ along the direction parallel or perpendicular, respectively, to the separation vector,

$$v_r = \Delta \mathbf{V} \cdot \begin{pmatrix} \sin \ell \\ -\cos \ell \end{pmatrix} = (\Omega - \Omega_0) R_0 \sin \ell, \quad (2.57)$$

$$v_t = \Delta \mathbf{V} \cdot \begin{pmatrix} \cos \ell \\ \sin \ell \end{pmatrix} = (\Omega - \Omega_0) R_0 \cos \ell - \Omega D. \quad (2.58)$$

A purely geometric derivation of these relations is given in Fig. 2.16.

Rotation Curve near R_0 ; Oort Constants. Using (2.57) one can derive the angular velocity by means of measuring v_r , but not the radius R to which it corresponds. Therefore, by measuring the radial velocity alone $\Omega(R)$ cannot be determined. If one measures v_r and, in addition, the proper motion $\mu = v_t/D$ of stars, then Ω and D can be determined from the equations above, and from D and ℓ one obtains $R = \sqrt{R_0^2 + D^2 - 2R_0D \cos \ell}$. The effects of extinction prohibits the use of this method for large distances D , since we have considered objects in the Galactic disk. For small distances $D \ll R_0$, which implies $|R - R_0| \ll R_0$, we can make a local approximation by evaluating the expressions above only up to first order in $(R - R_0)/R_0$. In this linear approximation we get

$$\Omega - \Omega_0 \approx \left(\frac{d\Omega}{dR} \right)_{|R_0} (R - R_0), \quad (2.59)$$

where the derivative has to be evaluated at $R = R_0$. Hence

$$v_r = (R - R_0) \left(\frac{d\Omega}{dR} \right)_{|R_0} R_0 \sin \ell ,$$

and furthermore, with (2.56),

$$\begin{aligned} R_0 \left(\frac{d\Omega}{dR} \right)_{|R_0} &= \frac{R_0}{R} \left[\left(\frac{dV}{dR} \right)_{|R_0} - \frac{V}{R} \right] \\ &\approx \left(\frac{dV}{dR} \right)_{|R_0} - \frac{V_0}{R_0} , \end{aligned}$$

in zeroth order in $(R - R_0)/R_0$. Combining the last two equations yields

$$v_r = \left[\left(\frac{dV}{dR} \right)_{|R_0} - \frac{V_0}{R_0} \right] (R - R_0) \sin \ell ; \quad (2.60)$$

in analogy to this, we obtain for the tangential velocity

$$v_t = \left[\left(\frac{dV}{dR} \right)_{|R_0} - \frac{V_0}{R_0} \right] (R - R_0) \cos \ell - \Omega_0 D . \quad (2.61)$$

For $|R - R_0| \ll R_0$ it follows that $R_0 - R \approx D \cos \ell$; if we insert this into (2.60) and (2.61) we get

$$\boxed{v_r \approx A D \sin 2\ell , \quad v_t \approx A D \cos 2\ell + B D} , \quad (2.62)$$

where A and B are the *Oort constants*

$$\boxed{\begin{aligned} A &:= -\frac{1}{2} \left[\left(\frac{dV}{dR} \right)_{|R_0} - \frac{V_0}{R_0} \right] , \\ B &:= -\frac{1}{2} \left[\left(\frac{dV}{dR} \right)_{|R_0} + \frac{V_0}{R_0} \right] . \end{aligned}} \quad (2.63)$$

The radial and tangential velocity fields relative to the Sun show a sine curve with period π , where v_t and v_r are phase-shifted by $\pi/4$. This behavior of the velocity field in the Solar neighborhood is indeed observed (see Fig. 2.17). By fitting the data for $v_r(\ell)$ and $v_t(\ell)$ for stars of equal distance D one can determine A and B , and thus

$$\boxed{\Omega_0 = \frac{V_0}{R_0} = A - B, \quad \left(\frac{dV}{dR} \right)_{|R_0} = -(A + B)} . \quad (2.64)$$

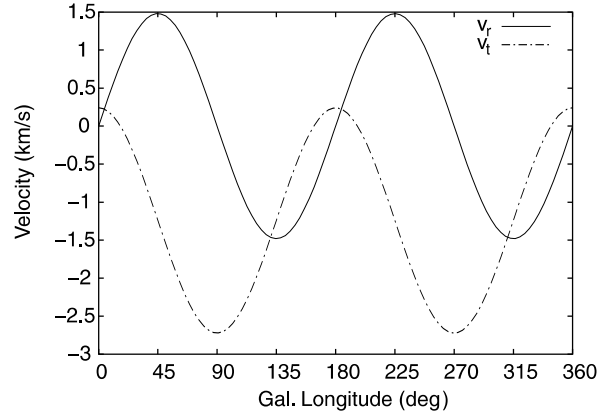


Fig. 2.17. The radial velocity v_r of stars at a fixed distance D is proportional to $\sin 2\ell$; the tangential velocity v_t is a linear function of $\cos 2\ell$. From the amplitude of the oscillating curves and from the mean value of v_t the Oort constants A and B can be derived, respectively (see (2.62))

The Oort constants thus yield the angular velocity of the Solar orbit and its derivative, and therefore the local kinematical information. If our Galaxy was rotating rigidly so that Ω was independent of the radius, $A = 0$ would follow. But the Milky Way rotates differentially, i.e., the angular velocity depends on the radius. Measurements yield the following values for A and B ,

$$\boxed{\begin{aligned} A &= (14.8 \pm 0.8) \text{ km s}^{-1} \text{ kpc}^{-1} , \\ B &= (-12.4 \pm 0.6) \text{ km s}^{-1} \text{ kpc}^{-1} . \end{aligned}} \quad (2.65)$$

Galactic Rotation Curve for $R < R_0$; Tangent Point Method. To measure the rotation curve for radii that are significantly smaller than R_0 , one has to turn to large wavelengths due to extinction in the disk. Usually the 21-cm emission line of neutral hydrogen is used, which can be observed over large distances, or the emission of CO in molecular gas. These gas components are found throughout the disk and are strongly concentrated towards the plane. Furthermore, the radial velocity can easily be measured from the Doppler effect. However, since the distance to a hydrogen cloud cannot be determined directly, a method is needed to link the measured radial velocities to the distance of the gas from the Galactic center. For this purpose the *tangent point method* is used.

Consider a line-of-sight at fixed Galactic longitude ℓ , with $\cos \ell > 0$ (thus “inwards”). The radial velocity v_r along this line-of-sight for objects moving on circular orbits is a function of the distance D , according to (2.57). If $\Omega(R)$ is a monotonically decreasing function, v_r attains a maximum where the line-of-sight is tangent to the local orbit, and thus its distance R from the Galactic center attains the minimum value R_{\min} . This is the case at

$$D = R_0 \cos \ell, \quad R_{\min} = R_0 \sin \ell \quad (2.66)$$

(see Fig. 2.18). The maximum radial velocity there, according to (2.57), is

$$\begin{aligned} v_{r,\max} &= [\Omega(R_{\min}) - \Omega_0] R_0 \sin \ell \\ &= V(R_{\min}) - V_0 \sin \ell, \end{aligned} \quad (2.67)$$

so that from the measured value of $v_{r,\max}$ as a function of direction ℓ , the rotation curve inside R_0 can be determined,

$$V(R) = \left(\frac{R}{R_0} \right) V_0 + v_{r,\max} (\sin \ell = R/R_0). \quad (2.68)$$

In the optical regime of the spectrum this method can only be applied locally, i.e., for small D , due to extinction. This is the case if one observes in a direction nearly tangential to the orbit of the Sun, i.e., if

$0 < \pi/2 - \ell \ll 1$ or $0 < \ell - 3\pi/2 \ll 1$, or $|\sin \ell| \approx 1$, so that $R_0 - R_{\min} \ll R_0$. In this case we get, to first order in $(R_0 - R_{\min})$, using (2.66),

$$\begin{aligned} V(R_{\min}) &\approx V_0 + \left(\frac{dV}{dR} \right)_{|R_0} (R_{\min} - R_0) \\ &= V_0 - \left(\frac{dV}{dR} \right)_{|R_0} R_0 (1 - \sin \ell), \end{aligned} \quad (2.69)$$

so that with (2.67)

$$\begin{aligned} v_{r,\max} &= \left[V_0 - \left(\frac{dV}{dR} \right)_{|R_0} R_0 \right] (1 - \sin \ell) \\ &= 2 A R_0 (1 - \sin \ell) \end{aligned}, \quad (2.70)$$

where (2.63) was used in the last step. This relation can also be used for determining the Oort constant A .

To determine $V(R)$ for smaller R by employing the tangent point method, we have to observe in wavelength regimes in which the Galactic plane is transparent, using radio emission lines of gas. In Fig. 2.18, a typical intensity profile of the 21-cm line along a line-of-sight is sketched; according to the Doppler effect this can be converted directly into a velocity profile using $v_r = (\lambda - \lambda_0)/\lambda_0$. It consists of several maxima that originate in individual gas clouds. The radial velocity of each cloud is defined by its distance R from the Galactic

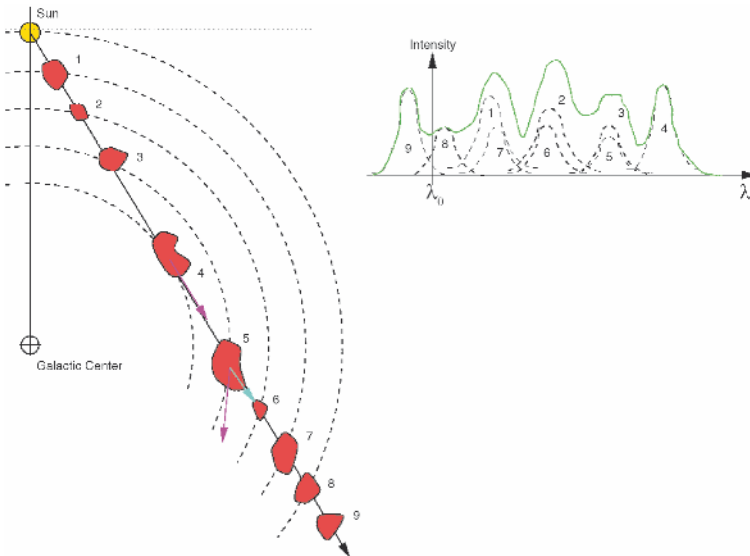


Fig. 2.18. The ISM is optically thin for 21-cm radiation, and thus we receive the 21-cm emission of HI regions from everywhere in the Galaxy. Due to the motion of an HI cloud relative to us, the wavelength is shifted. This can be used to measure the radial velocity of the cloud. With the assumption that the gas is moving on a circular orbit around the Galactic center, one expects that for the cloud in the tangent point (cloud 4), the full velocity is projected along the line-of-sight so that this cloud will therefore have the largest radial velocity. If the distance of the Sun to the Galactic center is known, the velocity of a cloud and its distance from the Galactic center can then be determined

center (if the gas follows the Galactic rotation), so that the largest radial velocity will occur for gas closest to the tangent point, which will be identified with $v_{r,\max}(\ell)$. Figure 2.19 shows the observed intensity profile of the ^{12}CO line as a function of the Galactic longitude, from which the rotation curve for $R < R_0$ can be read off.

With the tangent point method, applied to the 21-cm line of neutral hydrogen or to radio emission lines of molecular gas, the rotation curve of the Galaxy inside the Solar orbit can be measured.

Rotation Curve for $R > R_0$. The tangent point method cannot be applied for $R > R_0$ because for lines-of-sight at $\pi/2 < \ell < 3\pi/2$, the radial velocity v_r attains no maximum. In this case, the line-of-sight is nowhere parallel to a circular orbit.

Measuring $V(R)$ for $R > R_0$ requires measuring v_r for objects whose distance can be determined directly, e.g., Cepheids, for which the period–luminosity relation (Sect. 2.2.7) is used, or O- and B-stars in HII regions. With ℓ and D known, R can then be calculated, and with (2.57) we obtain $\Omega(R)$ or $V(R)$, respectively. Any object with known D and v_r thus contributes one data point to the Galactic rotation curve. Since the distance estimates of individual objects are always affected by

uncertainties, the rotation curve for large values of R is less accurately known than that inside the Solar circle.

It turns out that the rotation curve for $R > R_0$ does not decline outwards (see Fig. 2.20) as we would expect from the distribution of visible matter in the Milky Way. Both the stellar density and the gas density of the Galaxy decline exponentially for large R – e.g., see (2.34). This steep radial decline of the visible matter density should imply that $M(R)$, the mass inside R , is nearly constant for $R \gtrsim R_0$, from which a velocity profile like $V \propto R^{-1/2}$ would follow, according to Kepler’s law. However, this is not the case: $V(R)$ is virtually constant for $R > R_0$, indicating that $M(R) \propto R$. Thus, to get a constant rotational velocity of the Galaxy much more matter has to be present than we observe in gas and stars.

The Milky Way contains, besides stars and gas, an additional component of matter that dominates the mass at $R \gtrsim R_0$ but which has not yet been observed directly. Its presence is known only by its gravitational effect – hence, it is called dark matter.

In Sect. 3.3.3 we will see that this is a common phenomenon. The rotation curves of spiral galaxies are flat at large radii up to the maximum radius at which it can be measured; *spiral galaxies contain dark matter*.

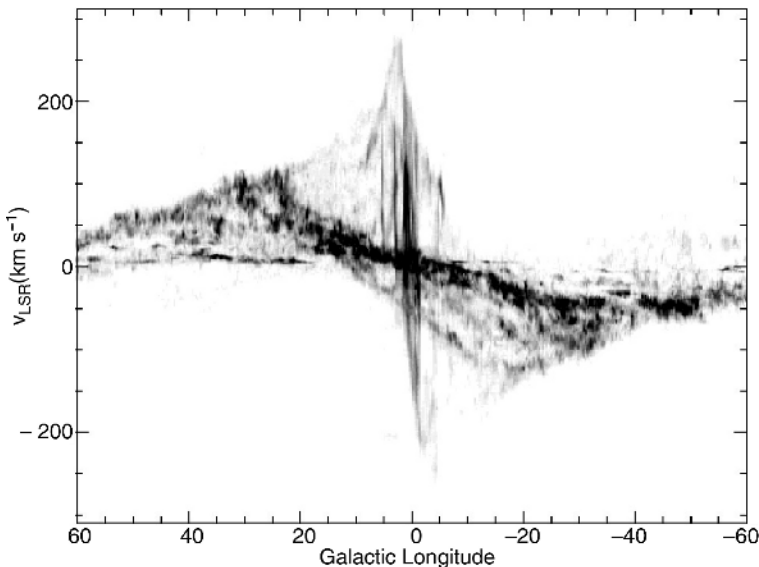


Fig. 2.19. ^{12}CO emission of molecular gas in the Galactic disk. For each ℓ , the intensity of the emission in the $\ell - v_r$ plane is plotted, integrated over the range $-2^\circ \leq b \leq 2^\circ$ (i.e., very close to the middle of the plane). Since v_r depends on the distance along each line-of-sight, characterized by ℓ , this diagram contains information on the rotation curve of the Galaxy as well as on the spatial distribution of the gas. The maximum velocity at each ℓ is rather well defined and forms the basis for the tangent point method

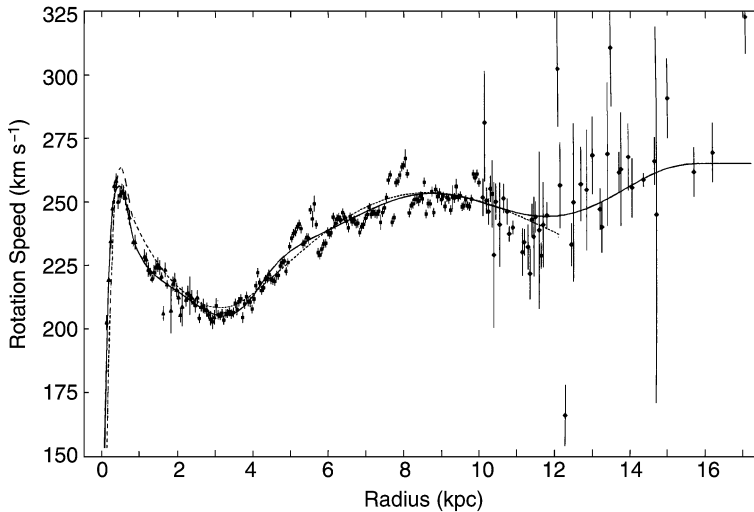


Fig. 2.20. Rotation curve of the Milky Way. Inside the “Solar circle”, that is at $R < R_0$, the radial velocity is determined quite accurately using the tangent point method; the measurements outside have larger uncertainties

The nature of dark matter is thus far unknown; in principle, we can distinguish two totally different kinds of dark matter candidates:

- *Astrophysical dark matter*, consisting of compact objects – e.g., faint stars like white dwarfs, brown dwarfs, black holes, etc. Such objects were assigned the name MACHOs, which stands for “MASSive Compact Halo Objects”.
- *Particle physics dark matter*, consisting of elementary particles which have thus far escaped detection in accelerator laboratories.

Although the origin of astrophysical dark matter would be difficult to understand (not least because of the baryon abundance in the Universe – see Sect. 4.4.4 – and because of the metal abundance in the ISM), a direct distinction between the two alternatives through observation would be of great interest. In the following section we will describe a method which is able to probe whether the dark matter in our Galaxy consists of MACHOs.

2.5 The Galactic Microlensing Effect: The Quest for Compact Dark Matter

In 1986, Bohdan Paczyński proposed to test the possible presence of MACHOs by performing microlensing experiments. As we will soon see, this was a daring idea

at that time, but since then such experiments have been carried out. In this section we will mainly summarize and discuss the results of these searches for MACHOs. We will start with a description of the microlensing effect and then proceed with its specific application to the search for MACHOs.

2.5.1 The Gravitational Lensing Effect I

Einstein’s Deflection Angle. *Light, just like massive particles, is deflected in a gravitational field.* This is one of the specific predictions by Einstein’s theory of gravity, General Relativity. Quantitatively it predicts that a light beam which passes a point mass M at a distance ξ is deflected by an angle $\hat{\alpha}$, which amounts to

$$\hat{\alpha} = \frac{4 G M}{c^2 \xi}. \quad (2.71)$$

The deflection law (2.71) is valid as long as $\hat{\alpha} \ll 1$, which is the case for weak gravitational fields. If we now set $M = M_\odot$, $R = R_\odot$ in the foregoing equation, we obtain

$$\hat{\alpha}_\odot \approx 1''.74$$

for the light deflection at the limb of the Sun. This deflection of light was measured during a Solar eclipse in 1919 from the shift of the apparent positions of stars

close to the shaded Solar disk. Its agreement with the value predicted by Einstein made him world-famous over night, because this was the first real and challenging test of General Relativity. Although the precision of the measured value back then was only $\sim 30\%$, it was sufficient to confirm Einstein's theory. By now the law (2.71) has been measured in the Solar System with a precision of about 0.1%, and Einstein's prediction has been confirmed.

Not long after the discovery of gravitational light deflection at the Sun, the following scenario was considered. If the deflection of the light were sufficiently strong, light from a very distant source could be visible at two positions in the sky: one light ray could pass a mass concentration, located between us and the source, "to the right", and the second one "to the left", as sketched in Fig. 2.21. The astrophysical consequence of this gravitational light deflection is also called the *gravitational lens effect*. We will discuss various aspects of

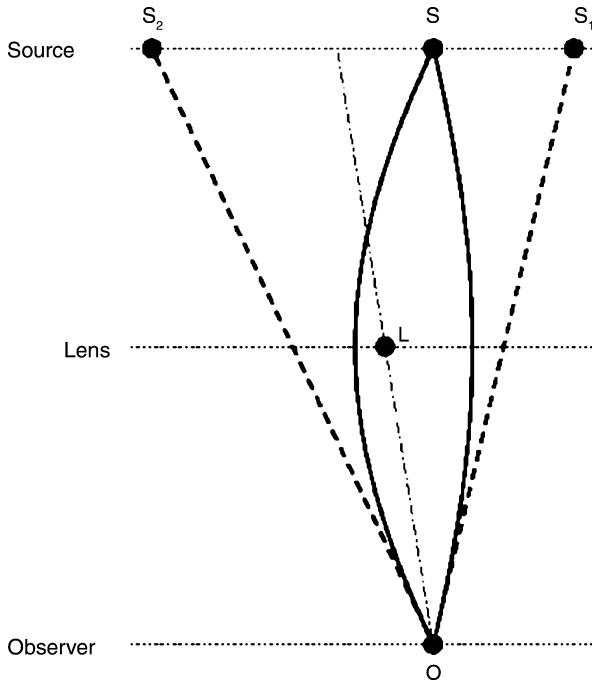


Fig. 2.21. Sketch of a gravitational lens system. If a sufficiently massive mass concentration is located between us and a distant source, it may happen that we observe this source at two different positions on the sphere

the lens effect in the course of this book, and we will review its astrophysical applications.

The Sun is not able to cause multiple images of distant sources. The maximum deflection angle $\hat{\alpha}_\odot$ is much smaller than the angular radius of the Sun, so that two beams of light that pass the Sun to the left and to the right cannot converge by light deflection at the position of the Earth. Given its radius, the Sun is too close to produce multiple images, since its angular radius is (far) larger than the deflection angle $\hat{\alpha}_\odot$. However, the light deflection by more distant stars (or other massive celestial bodies) can produce multiple images of sources located behind them.

Lens Geometry. The geometry of a gravitational lens system is depicted in Fig. 2.22. We consider light rays from a source at distance D_s from us that pass a mass concentration (called a lens or deflector) at a separation ξ . The deflector is at a distance D_d from us. In Fig. 2.22 η denotes the true, two-dimensional position of the source in the source plane, and β is the true angular position of the source, that is the angular position at which it would be observed in the absence of light deflection,

$$\beta = \frac{\eta}{D_s}. \quad (2.72)$$

The position of the light ray in the lens plane is denoted by ξ , and θ is the corresponding angular position,

$$\theta = \frac{\xi}{D_d}. \quad (2.73)$$

Hence, θ is the observed position of the source on the sphere relative to the position of the "center of the lens" which we have chosen as the origin of the coordinate system, $\xi = 0$. D_{ds} is the distance of the source plane from the lens plane. As long as the relevant distances are much smaller than the "radius of the Universe" c/H_0 , which is certainly the case within our Galaxy and in the Local Group, we have $D_{ds} = D_s - D_d$. However, this relation is no longer valid for cosmologically distant sources and lenses; we will come back to this in Sect. 4.3.3.

Lens Equation. From Fig. 2.22 we can deduce the condition that a light ray from the source will reach us from the direction θ (or ξ),

$$\eta = \frac{D_s}{D_d} \xi - D_{ds} \hat{\alpha}(\xi), \quad (2.74)$$

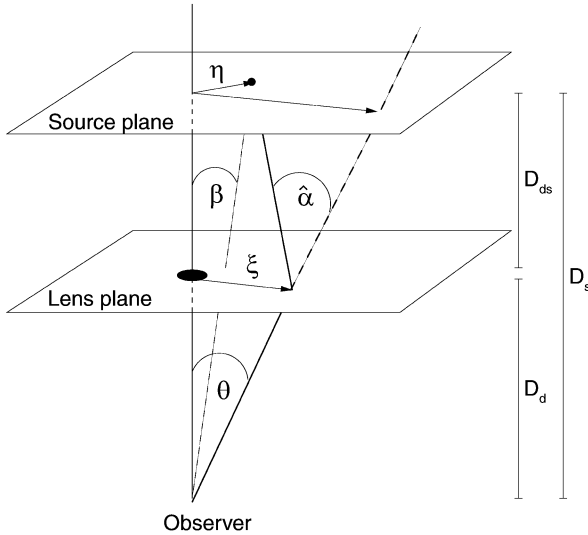


Fig. 2.22. Geometry of a gravitational lens system. Consider a source to be located at a distance D_s from us and a mass concentration at distance D_d . An optical axis is defined that connects the observer and the center of the mass concentration; its extension will intersect the so-called source plane, a plane perpendicular to the optical axis at the distance of the source. Accordingly, the lens plane is the plane perpendicular to the line-of-sight to the mass concentration at distance D_d from us. The intersections of the optical axis and the planes are chosen as the origins of the respective coordinate systems. Let the source be at the point η in the source plane; a light beam that encloses an angle θ to the optical axis intersects the lens plane at the point ξ and is deflected by an angle $\hat{\alpha}(\xi)$. All these quantities are two-dimensional vectors. The condition that the source is observed in the direction θ is given by the lens equation (2.74) which follows from the theorem of intersecting lines

or, after dividing by D_s and using (2.72) and (2.73):

$$\beta = \theta - \frac{D_{ds}}{D_s} \hat{\alpha}(D_d \theta). \quad (2.75)$$

Due to the factor multiplying the deflection angle in (2.75), it is convenient to define the *reduced deflection angle*

$$\alpha(\theta) := \frac{D_{ds}}{D_s} \hat{\alpha}(D_d \theta), \quad (2.76)$$

so that the lens equation (2.75) attains the simple form

$$\beta = \theta - \alpha(\theta). \quad (2.77)$$

The deflection angle $\alpha(\theta)$ depends on the mass distribution of the deflector. We will discuss the deflection angle for an arbitrary density distribution of a lens in Sect. 3.8. Here we will first concentrate on point masses, which is – in most cases – a good approximation for the lensing effect on stars.

For a point mass, we get – see (2.71)

$$|\alpha(\theta)| = \frac{D_{ds}}{D_s} \frac{4GM}{c^2 D_d} \frac{1}{|\theta|},$$

or, if we account for the direction of the deflection (the deflection angle always points towards the point mass),

$$\alpha(\theta) = \frac{4GM}{c^2} \frac{D_{ds}}{D_s D_d} \frac{\theta}{|\theta|^2}. \quad (2.78)$$

Multiple Images of a source occur if the lens equation (2.77) has multiple solutions θ_i for a (true) source position β – in this case, the source is observed at the positions θ_i on the sphere.

Explicit Solution of the Lens Equation for a Point Mass. The lens equation for a point mass is simple enough to be solved analytically which means that for each source position β the respective image positions θ_i can be determined. If we define the so-called *Einstein angle* of the lens,

$$\theta_E := \sqrt{\frac{4GM}{c^2} \frac{D_{ds}}{D_s D_d}}, \quad (2.79)$$

then the lens equation (2.77) for the point-mass lens with a deflection angle (2.78) can be written as

$$\beta = \theta - \theta_E^2 \frac{\theta}{|\theta|^2}.$$

Obviously, θ_E is a characteristic angle in this equation, so that for practical reasons we will use the scaling

$$y := \frac{\beta}{\theta_E}; \quad x := \frac{\theta}{\theta_E}.$$

Hence the lens equation simplifies to

$$y = x - \frac{x}{|x|^2}. \quad (2.80)$$

After multiplication with x , this becomes a quadratic equation, whose solutions are

$$\mathbf{x} = \frac{1}{2} \left(|\mathbf{y}| \pm \sqrt{4 + |\mathbf{y}|^2} \right) \frac{\mathbf{y}}{|\mathbf{y}|}. \quad (2.81)$$

From this solution of the lens equation one can immediately draw a number of conclusions:

- For each source position \mathbf{y} , the lens equation for a point-mass lens has two solutions – any source is (formally, at least) imaged twice. The reason for this is the divergence of the deflection angle for $\theta \rightarrow 0$. This divergence does not occur in reality because of the finite geometric extent of the lens (e.g., the radius of the star), as the solutions are of course physically relevant only if $\xi = D_d \theta_E |\mathbf{x}|$ is larger than the radius of the star. We need to point out again that we explicitly exclude the case of strong gravitational fields such as the light deflection near a black hole or a neutron star, for which the equation for the deflection angle has to be modified.
- The two images \mathbf{x}_i are collinear with the lens and the source. In other words, the observer, lens, and source define a plane, and light rays from the source that reach the observer are located in this plane as well. One of the two images is located on the same side of the lens as the source ($\mathbf{x} \cdot \mathbf{y} > 0$), the second image is located on the other side – as is already indicated in Fig. 2.21.
- If $\mathbf{y} = 0$, so that the source is positioned exactly behind the lens, the full circle $|\mathbf{x}| = 1$, or $|\theta| = \theta_E$, is a solution of the lens equation (2.80) – the source is seen as a circular image. In this case, the source, lens, and observer no longer define a plane, and the problem becomes axially symmetric. Such a circular image is called an *Einstein ring*. Ring-shaped images have indeed been observed, as we will discuss in Sect. 3.8.3.
- The angular diameter of this ring is then $2\theta_E$. From the solution (2.81), one can easily see that the distance between the two images is about $\Delta x = |\mathbf{x}_1 - \mathbf{x}_2| \gtrsim 2$ (as long as $|\mathbf{y}| \lesssim 1$), hence

$$\Delta\theta \gtrsim 2\theta_E;$$

the Einstein angle thus specifies the characteristic image separation. Situations with $|\mathbf{y}| \gg 1$, and hence angular separations significantly larger than $2\theta_E$, are

astrophysically of only minor relevance, as will be shown below.

Magnification: The Principle. Light beams are not only deflected as a whole, but they are also subject to differential deflection. For instance, those rays of a light beam (also called light bundle) that are closer to the lens are deflected more than rays at the other side of the beam. The differential deflection is an effect of the tidal component of the deflection angle; this is sketched in Fig. 2.23. By differential deflection, the solid angle which the image of the source subtends on the sky changes. Let ω_s be the solid angle the source would subtend if no lens were present, and ω the observed solid angle of the image of the source in the presence of a deflector. Since gravitational light deflection is not linked to emission or absorption of radiation, the sur-

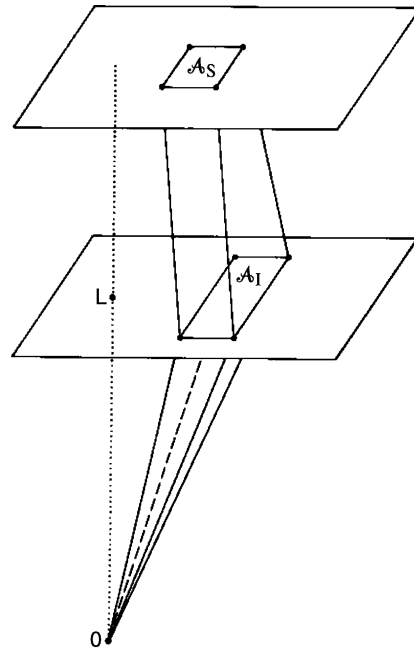


Fig. 2.23. Light beams are deflected differentially, leading to changes of the shape and the cross-sectional area of the beam. As a consequence, the observed solid angle subtended by the source, as seen by the observer, is modified by gravitational light deflection. In the example shown, the observed solid angle \mathcal{A}_I/D_d^2 is larger than the one subtended by the undeflected source, \mathcal{A}_S/D_s^2 – the image of the source is thus magnified

face brightness (or specific intensity) is preserved. The flux of a source is given as the product of surface brightness and solid angle. Since the former of the two factors is unchanged by light deflection, but the solid angle changes, the observed flux of the source is modified. If S_0 is the flux of the unlensed source and S the flux of an image of the source, then

$$\mu := \frac{S}{S_0} = \frac{\omega}{\omega_s} \quad (2.82)$$

describes the change in flux that is caused by a magnification (or a diminution) of the image of a source. Obviously, the magnification is a purely geometrical effect.

Magnification for “Small” Sources. For sources and images that are much smaller than the characteristic scale of the lens, the magnification μ is given by the differential area distortion of the lens mapping (2.77),

$$\mu = \left| \det \left(\frac{\partial \beta}{\partial \theta} \right) \right|^{-1} \equiv \left| \det \left(\frac{\partial \beta_i}{\partial \theta_j} \right) \right|^{-1}. \quad (2.83)$$

Hence for small sources, the ratio of solid angles of the lensed image and the unlensed source is described by the determinant of the local Jacobi matrix.¹¹

The magnification can therefore be calculated for each individual image of the source, and the total magnification of a source, given by the ratio of the sum of the fluxes of the individual images and the flux of the unlensed source, is the sum of the magnifications for the individual images.

Magnification for the Point-Mass Lens. For a point-mass lens, the magnifications for the two images (2.81) are

$$\mu_{\pm} = \frac{1}{4} \left(\frac{y}{\sqrt{y^2 + 4}} + \frac{\sqrt{y^2 + 4}}{y} \pm 2 \right). \quad (2.84)$$

From this it follows that for the “+”-image $\mu_+ > 1$ for all source positions $y = |y|$, whereas the “-”-image can

have magnification either larger or less than unity, depending on y . The magnification of the two images is illustrated in Fig. 2.24, while Fig. 2.25 shows the magnification for several different source positions y . For $y \gg 1$, one has $\mu_+ \gtrsim 1$ and $\mu_- \sim 0$, from which we draw the following conclusion: if the source and lens are not sufficiently well aligned, the secondary image is strongly demagnified and the primary image has magnification very close to unity. For this reason, situations with $y \gg 1$ are of little relevance since then essentially only one image is observed which has about the same flux as the unlensed source.

For $y \rightarrow 0$, the two magnifications diverge, $\mu_{\pm} \rightarrow \infty$. The reason for this is purely geometric: in this case, out of a zero-dimensional point source a one-dimensional image, the Einstein ring, is formed. This divergence is not physical, of course, since infinite magnifications do not occur in reality. The magnifications remain finite even for $y = 0$, for two reasons. First, real sources have a finite extent, and for these the magnifi-

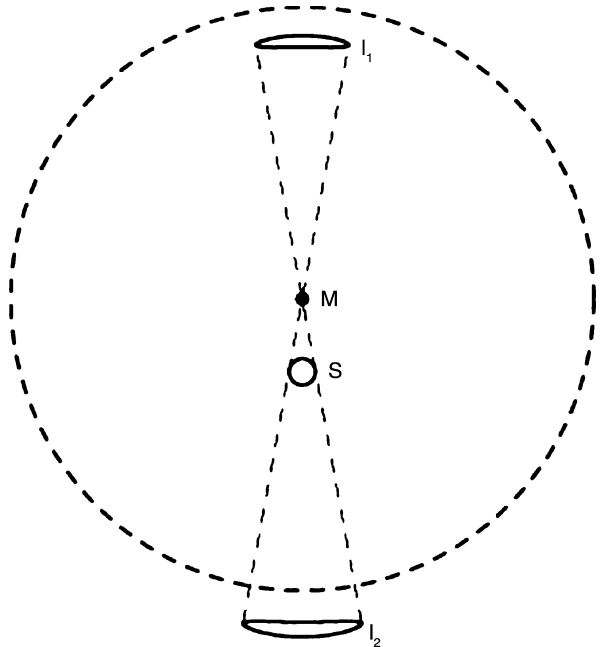


Fig. 2.24. Illustration of the lens mapping by a point mass M . The unlensed source S and the two images I_1 and I_2 of the lensed source are shown. We see that the two images have a solid angle different from the unlensed source, and they also have a different shape. The dashed circle shows the Einstein radius of the lens

¹¹The determinant in (2.83) is a generalization of the derivative in one spatial dimension to higher dimensional mappings. Consider a scalar mapping $y = y(x)$; through this mapping, a “small” interval Δx is mapped onto a small interval Δy , where $\Delta y \approx (dy/dx) \Delta x$. The Jacobian determinant occurring in (2.83) generalizes this result for a two-dimensional mapping from the lens plane to the source plane.

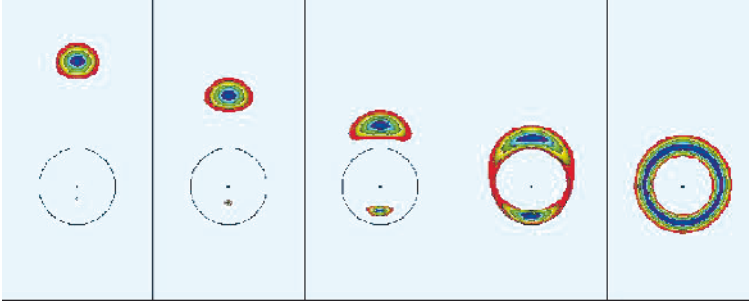


Fig. 2.25. Image of a circular source with a radial brightness profile – indicated by colors – for different relative positions of the lens and source. y decreases from left to right; in the rightmost figure $y = 0$ and an Einstein ring is formed

cation is finite. Second, even if one had a point source, wave effects of the light (interference) would lead to a finite value of μ . The total magnification of a point source by a point-mass lens follows from the sum of the magnifications (2.84),

$$\mu(y) = \mu_+ + \mu_- = \frac{y^2 + 2}{y\sqrt{y^2 + 4}}. \quad (2.85)$$

2.5.2 Galactic Microlensing Effect

After these theoretical considerations we will now return to the starting point of our discussion, employing the lensing effect as a potential diagnostic for dark matter in our Milky Way, if this dark matter were to consist of compact mass concentrations, e.g., very faint stars.

Image Splitting. Considering a star in our Galaxy as the lens, (2.79) yields the Einstein angle

$$\theta_E = 0.902 \text{ mas} \left(\frac{M}{M_\odot} \right)^{1/2} \times \left(\frac{D_d}{10 \text{ kpc}} \right)^{-1/2} \left(1 - \frac{D_d}{D_s} \right)^{1/2}. \quad (2.86)$$

Since the angular separation $\Delta\theta$ of the two images is about $2\theta_E$, the typical image splittings are about a milliarcsecond (mas) for lens systems including Galactic stars; such angular separations are as yet not observable with optical telescopes. This insight made Einstein believe in 1936, after he conducted a detailed quantitative analysis of gravitational lensing by point masses, that the lens effect will not be observable.¹²

Magnification. Bohdan Paczyński pointed out in 1986 that, although image splitting was unobservable, the magnification by the lens should nevertheless be measurable. To do this, we have to realize that the absolute magnification is observable only if the unlensed flux of the source is known – which is not the case, of course (for nearly all sources). However, the magnification, and therefore also the observed flux, changes with time by the relative motion of source, lens, and ourselves. Therefore, the flux is a function of time, caused by the time-dependent magnification.

Characteristic Time-Scale of the Variation. Let v be a typical transverse velocity of the lens, then its angular velocity is

$$\dot{\theta} = \frac{v}{D_d} = 4.22 \text{ mas yr}^{-1} \left(\frac{v}{200 \text{ km/s}} \right) \left(\frac{D_d}{10 \text{ kpc}} \right)^{-1}, \quad (2.87)$$

if we consider the source and the observer to be at rest. The characteristic time-scale of the variability is then given by

$$t_E := \frac{\theta_E}{\dot{\theta}} = 0.214 \text{ yr} \left(\frac{M}{M_\odot} \right)^{1/2} \left(\frac{D_d}{10 \text{ kpc}} \right)^{1/2} \times \left(1 - \frac{D_d}{D_s} \right)^{1/2} \left(\frac{v}{200 \text{ km/s}} \right)^{-1}. \quad (2.88)$$

This time-scale is of the order of a month for lenses with $M \sim M_\odot$ and typical Galactic velocities. Hence,

¹² The expression “microlens” has its origin in the angular scale (2.86) that was discussed in the context of the lens effect on quasars by stars at cosmological distances, for which one obtains image splittings of about one microarcsecond.

the effect is measurable in principle. In the general case that source, lens, and observer are all moving, v has to be considered as an effective velocity. Alternatively, the motion of the source in the source plane can be considered.

Light Curves. In most cases, the relative motion can be considered linear, so that the position of the source in the source plane can be written as

$$\boldsymbol{\beta} = \boldsymbol{\beta}_0 + \dot{\boldsymbol{\beta}}(t - t_0).$$

Using the scaled position $y = \boldsymbol{\beta}/\theta_E$, for $y = |y|$ we obtain

$$y(t) = \sqrt{p^2 + \left(\frac{t - t_{\max}}{t_E}\right)^2}, \quad (2.89)$$

where $p = y_{\min}$ specifies the minimum distance from the optical axis, and t_{\max} is the time at which $y = p$ attains this minimum value, thus when the magnification $\mu = \mu(p) = \mu_{\max}$ is maximized. From this, and using (2.85), one obtains the light curve

$$S(t) = S_0 \mu(y(t)) = S_0 \frac{y^2(t) + 2}{y(t) \sqrt{y^2(t) + 4}}. \quad (2.90)$$

Examples for such light curves are shown in Fig. 2.26. They depend on only four parameters: the flux of the unlensed source S_0 , the time of maximum magnification t_{\max} , the smallest distance of the source from the optical axis p , and the characteristic time-scale t_E . All these values are directly observable in a light curve. One obtains t_{\max} from the time of the maximum of the light curve, S_0 is the flux that is measured for very large and small times, $S_0 = S(t \rightarrow \pm\infty)$, or $S_0 \approx S(t)$ for $|t - t_{\max}| \gg t_E$. Furthermore, p follows from the maximum magnification $\mu_{\max} = S_{\max}/S_0$ by inversion of (2.85), and t_E from the width of the light curve.

Only t_E contains information of astrophysical relevance, because the time of the maximum, the unlensed flux of the source, and the minimum separation p provide no information about the lens. Since $t_E \propto \sqrt{M D_d}/v$, this time-scale contains the combined information on the lens mass, the distances to the lens and the source, and the transverse velocity: *Only the combination $t_E \propto \sqrt{M D_d}/v$ can be derived from the light curve, but not mass, distance, or velocity individually.*

Paczynski's idea can be expressed as follows: if the halo of our Milky Way consists (partially) of compact objects, a distant compact source should, from time to time, be lensed by one of these MACHOs and thus show characteristic changes in flux, corresponding to a light curve similar to those in Fig. 2.26. The number density of MACHOs is proportional to the probability or abundance of lens events, and the characteristic mass of the MACHOs is proportional to the square of the typical variation time-scale t_E . All one has to do is measure the light curves of a sufficiently large number of background sources and extract all lens events from those light curves to obtain information on the population of potential MACHOs in the halo. A given halo model predicts the spatial density distribution and the distribution of velocities of the MACHOs and can therefore be compared to the observations in a statistical way. However, one faces the problem that the abundance of such lensing events is very small.

Probability of a Lens Event. In practice, a system of a foreground object and a background source is considered a lens system if $p < 1$ and hence $\mu_{\max} > 3/\sqrt{5} \approx 1.34$, i.e., if the relative trajectory of the source passes within the Einstein circle of the lens.

If the dark halo of the Milky Way consisted solely of MACHOs, the probability that a very distant source is lensed (in the sense of $|\boldsymbol{\beta}| \leq \theta_E$) would be $\sim 10^{-7}$, where the exact value depends on the direction to the source. At any one time, one of $\sim 10^7$ distant sources would be located within the Einstein radius of a MACHO in our halo. The immediate consequence of this is that the light curves of millions of sources have to be monitored to detect this effect. Furthermore, these sources have to be located within a relatively small region on the sphere to keep the total solid angle that has to be photometrically monitored relatively small. This condition is needed to limit the required observing time, so that many such sources should be present within the field-of-view of the camera used. The stars of the Magellanic Clouds are well suited for such an experiment: they are close together on the sphere, but can still be resolved into individual stars.

Problems, and their Solution. From this observational strategy, a large number of problems arise immediately; they were discussed in Paczynski's original paper. First,

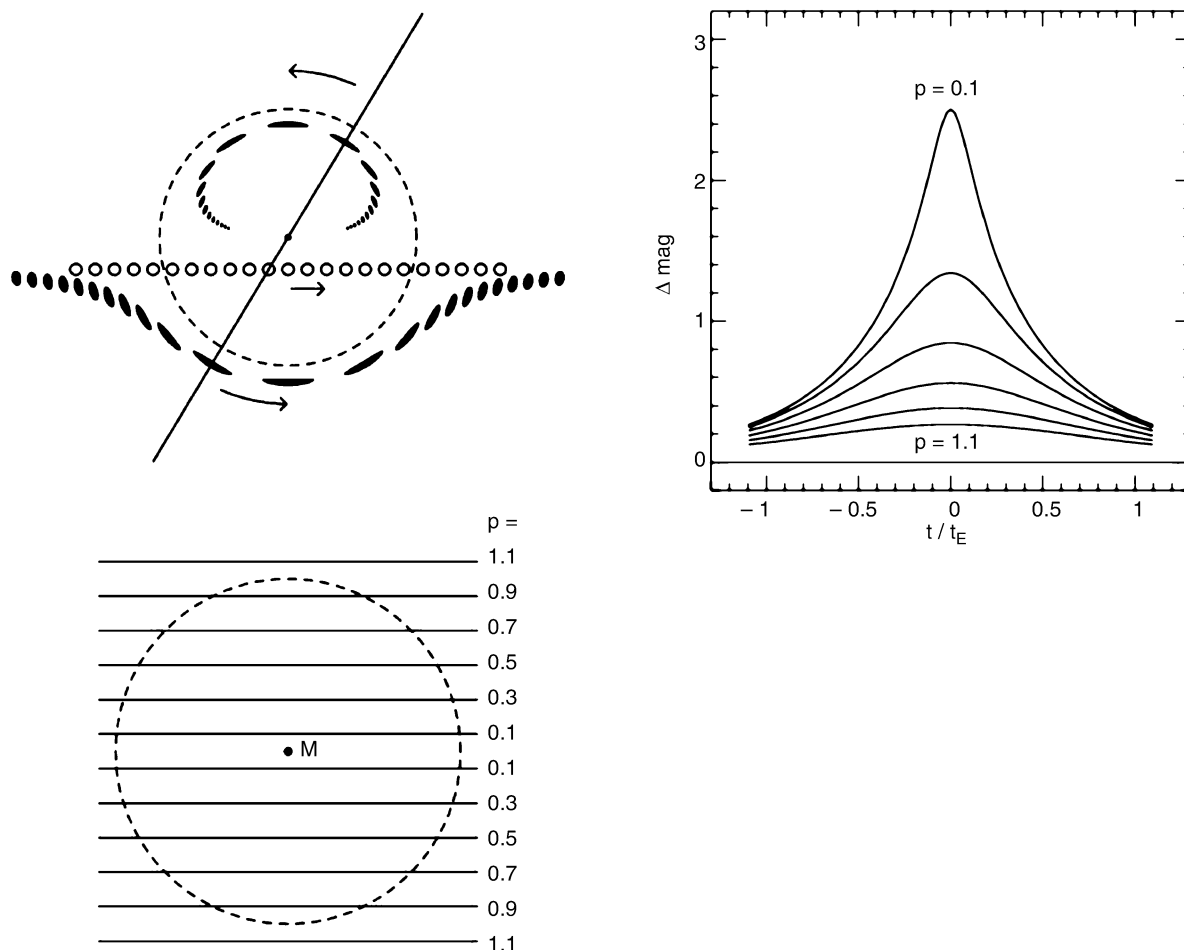


Fig. 2.26. Illustration of a Galactic microlensing event: In the upper left panel a source (depicted by the open circles) moves behind a point-mass lens; for each source position two images of the source are formed, which are indicated by the black ellipses. The identification of the corresponding image pair with the source position follows from the fact that, in projection, the source, the lens, and the two images are located on a straight line, which is indicated for one source position.

the photometry of so many sources over many epochs produces a huge amount of data that need to be handled; they have to be stored and reduced. Second, one has the problem of “crowding”: the stars in the Magellanic Clouds are densely packed on the sky, which renders the photometry of individual stars difficult. Third, stars also show intrinsic variability – about 1% of all stars are variable. This intrinsic variability has to be distinguished from that due to the lens effect. Due to the

The dashed circle represents the Einstein ring. In the lower left panel, different trajectories of the source are shown, each characterized by the smallest projected separation p to the lens. The light curves resulting from these relative motions, which can be calculated using equation (2.90), are then shown in the right-hand panel for different values of p . The smaller p is, the larger the maximum magnification will be, here measured in magnitudes

small abundance of the latter, selecting the lens events is comparable to searching for a needle in a haystack. Finally, it should be mentioned that one has to ensure that the experiment is indeed sensitive enough to detect lens events. A “calibration experiment” would therefore be desirable.

Faced with these problems, it seemed daring to seriously think about the realization of such an observing program. However, a fortunate event helped, in the mag-

nificant time of the easing of tension between the US and the Soviet Union, and their respective allies, at the end of the 1980s. Physicists and astrophysicists, partly occupied with issues concerning national security, then saw an opportunity to meet new challenges. In addition, scientists in national laboratories had much better access to sufficient computing power and storage capacity than those in other research institutes, attenuating some of the aforementioned problems. While the expected data volume was still a major problem in 1986, it could be handled a few years later. Also, wide-field cameras were constructed, with which large areas of the sky could be observed simultaneously. Software was developed which specializes in the photometry of objects in crowded fields, so that light curves could be measured even if individual stars in the image were no longer cleanly separated.

To distinguish between lensing events and intrinsic variability of stars, we note that the microlensing light curves have a characteristic shape that is described by only four parameters. The light curves should be symmetric and achromatic because gravitational light deflection is independent of the frequency of the radiation. Furthermore, due to the small lensing probability, any source should experience at most one microlensing event and show a constant flux before and after, whereas intrinsic variations of stars are often periodic and in nearly all cases chromatic.

And finally a control experiment could be performed: the lensing probability in the direction of the Galactic bulge is known, or at least, we can obtain a lower limit for it from the observed density of stars in the disk. If a microlens experiment is carried out in the direction of the Galactic bulge, we *have to* find lens events if the experiment is sufficiently sensitive.

2.5.3 Surveys and Results

In the early 1990s, two collaborations (MACHO and EROS) began the search for microlensing events towards the Magellanic clouds. Another group (OGLE) started searching in an area of the Galactic bulge. Fields in the respective survey regions were observed regularly, typically once every night if weather conditions permitted. From the photometry of the stars in the fields, light curves for many millions of stars were generated and then checked for microlensing events.

First Detections. In 1993, all three groups reported their first results. The MACHO collaboration found one event in the Large Magellanic Cloud (LMC), the EROS group two events, and the OGLE group observed one event in the bulge. The light curve of the first MACHO event is plotted in Fig. 2.27. It was observed in two different filters, and the fit to the data, which corresponds to a standard light curve (2.90), is the same for both filters, proving that the event is achromatic. Together with the quality of the fit to the data, this is very strong evidence for the microlensing nature of the event.

Statistical Results. In the years since 1993, all three aforementioned teams have proceeded with their ob-

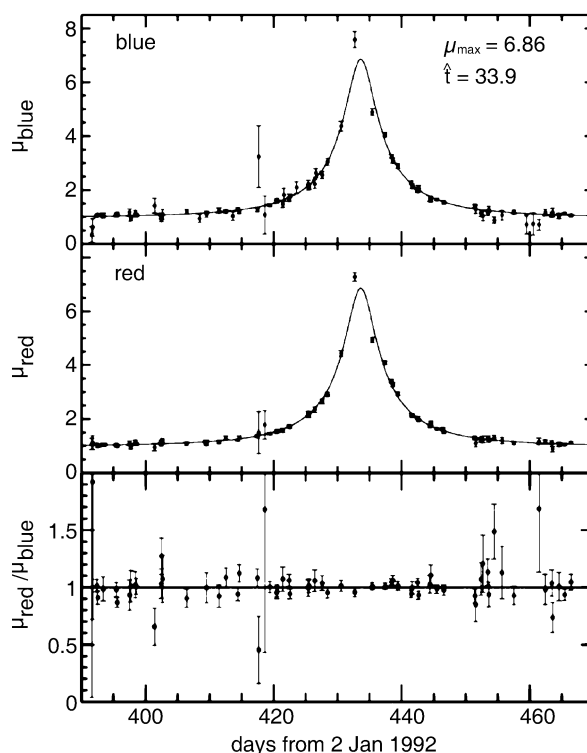


Fig. 2.27. Light curve of the first observed microlensing event in the LMC, in two broad-band filters. The solid curve is the best-fit microlens light curve as described by (2.90), with $\mu_{\max} = 6.86$. The ratio of the magnifications in both filters is displayed at the bottom, and it is compatible with 1. Some of the data points deviate significantly from the curve; this means that either the errors in the measurements were underestimated, or this event is more complicated than one described by a point-mass lens – see Sect. 2.5.4

servations and analysis (Fig. 2.28), and more groups have begun the search for microlensing events, choosing various lines-of-sight. The most important results from these experiments can be summarized as follows:

About 20 events have been found in the direction of the Magellanic Clouds, and of the order a thousand in the direction of the bulge. The statistical analysis of the data revealed the lensing probability towards the bulge to be higher than originally expected. This can be explained by the fact that *our Galaxy features a bar* (see Chap. 3). This bar was also observed in IR maps such as those made by the COBE satellite. The events in the direction of the bulge are dominated by lenses that are part of the bulge themselves, and their column density is increased by the bar-like shape of the bulge. On the other hand, the lens probability in the direction of the Magellanic Clouds is *smaller* than expected for the case where the dark halo consists solely of MACHOs.

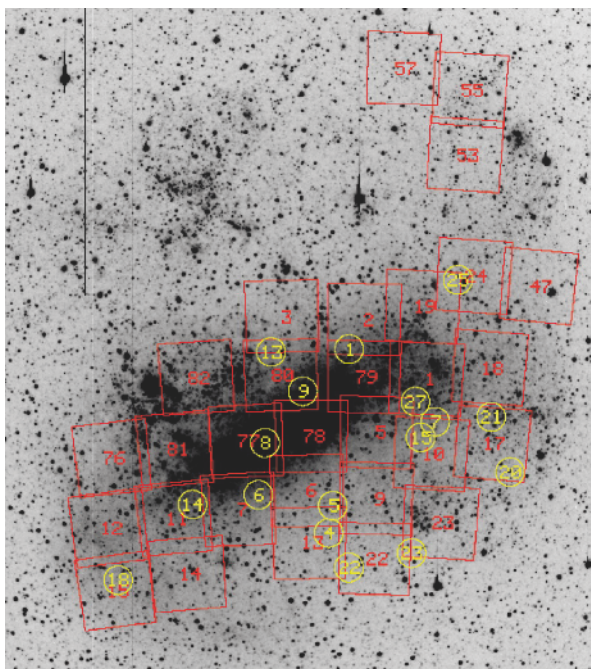


Fig. 2.28. In this $8^\circ \times 8^\circ$ image of the LMC, 30 fields are marked in red which the MACHO group has searched for microlensing events during the ~ 5.5 years of their experiment; images were taken in two filters to test for achromaticity. The positions of 17 microlensing events are marked by yellow circles; these have been subject to statistical analysis

Based on the analysis of the MACHO collaboration, the observed statistics of lensing events towards the Magellanic Clouds is best explained if about 20% of the halo mass consists of MACHOs, with a characteristic mass of about $M \sim 0.5M_\odot$ (see Fig. 2.29).

Interpretation and Discussion. This latter result is not easy to interpret and came as a real surprise. If a result compatible with $\sim 100\%$ had been found, it would have been obvious to conclude that the dark matter in our Milky Way consists of compact objects. Otherwise, if very few lensing events had been found, it would have been clear that MACHOs do not contribute significantly to the dark matter. But a value of 20% does not allow any unambiguous interpretation. Taken at face value, the result from the MACHO group would imply that the total mass of MACHOs in the Milky Way halo is about the same as that in the stellar disk.

Furthermore, the estimated mass scale is hard to understand: what could be the nature of MACHOs with $M = 0.5M_\odot$? Normal stars can be excluded, because they would be far too luminous not to be observed. White dwarfs are also unsuitable candidates, because to

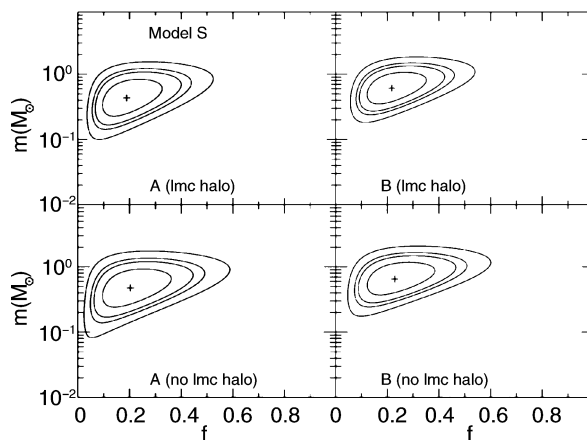


Fig. 2.29. Probability contours for a specific halo model as a function of the characteristic MACHO mass M (here denoted by m) and the mass fraction f of MACHOs in the halo. The halo of the LMC was either taken into account as an additional source for microlenses (lmc halo) or not (no lmc halo), and two different selection criteria (A,B) for the statistically complete microlensing sample have been used. In all cases, $M \sim 0.5M_\odot$ and $f \sim 0.2$ are the best-fit values

produce such a large number of white dwarfs as a final stage of stellar evolution, the total star formation in our Milky Way, integrated over its lifetime, needs to be significantly larger than normally assumed. In this case, many more massive stars would also have formed, which would then have released the metals they produced into the ISM, both by stellar winds and in supernova explosions. In such a scenario, the metal content of the ISM would therefore be distinctly higher than is actually observed. The only possibility of escaping this argument is with the hypothesis that the mass function of newly formed stars (the initial mass function, IMF) was different in the early phase of the Milky Way compared to that observed today. The IMF that needs to be assumed in this case is such that for each star of intermediate mass which evolves into a white dwarf, far fewer high-mass stars, responsible for the metal enrichment of the ISM, must have formed in the past compared to today. However, we lack a plausible physical model for such a scenario, and it is in conflict with the star-formation history that we observe in the high-redshift Universe (see Chap. 9).

Neutron stars can be excluded as well, because they are too massive (typically $> 1M_{\odot}$); in addition, they are formed in supernova explosions, implying that the aforementioned metallicity problem would be even greater for neutron stars. Would stellar-mass black holes be an alternative? The answer to this question depends on how they are formed. They could not originate in SN explosions, again because of the metallicity problem. If they had formed in a very early phase of the Universe (they are then called primordial black holes), this would be an imaginable, though perhaps quite exotic, alternative.

However, we have strong indications that the interpretation of the MACHO results is not as straightforward as described above. Some doubts have been raised as to whether all events reported as being due to microlensing are in fact caused by this effect. In fact, one of the microlensing source stars identified by the MACHO group showed another bump seven years after the first event. Given the extremely small likelihood of two microlensing events happening to a single source this is almost certainly a star with unusual variability.

As argued previously, by means of t_E we only measure a combination of lens mass, transverse velocity, and distance. The result given in Fig. 2.29 is therefore

based on the statistical analysis of the lensing events in the framework of a halo model that describes the shape and the radial density profile of the halo. However, microlensing events have been observed for which more than just t_E can be determined – e.g., events in which the lens is a binary star, or those for which t_E is larger than a few months. In this case, the orbit of the Earth around the Sun, which is not a linear motion, has a noticeable effect, causing deviations from the standard curve. Such parallax events have indeed been observed.¹³ Three events are known in the direction of the Magellanic Clouds in which more than just t_E could be measured. In all three cases the lenses are most likely located in the Magellanic Clouds themselves (an effect called self-lensing) and not in the halo of the Milky Way. If for those three cases, where the degeneracy between lens mass, distance, and transverse velocity can be broken, the respective lenses are not MACHOs in the Galactic halo, we might then suspect that in most of the other microlensing events the lens is not a MACHO either. Therefore, it is currently unclear how to interpret the results of the microlensing surveys. In particular, it is unclear to what extent self-lensing contributes to the results. Furthermore, the quantitative results depend on the halo model.

The EROS collaboration used an observation strategy which was slightly different from that of the MACHO group, by observing a number of fields in very short time intervals. Since the duration of a lensing event depends on the mass of the lens as $\Delta t \propto M^{1/2}$ – see (2.88) – they were also able to probe very small MACHO masses. The absence of lensing events of very short duration then allowed them to derive limits for the mass fraction of such low-mass MACHOs, as is shown in Fig. 2.30.

Despite this unsettled situation concerning the interpretation of the MACHO results, we have to emphasize that the microlensing surveys have been enormously successful experiments because they accomplished exactly what was expected at the beginning of the observations. They measured the lensing probability in the direction of the Magellanic Clouds and the Galactic bulge. The fact that the distribution of the lenses differs from that expected by no means diminishes the success of these surveys.

¹³ These parallax events in addition prove that the Earth is in fact orbiting around the Sun – even though this is not really a new insight.

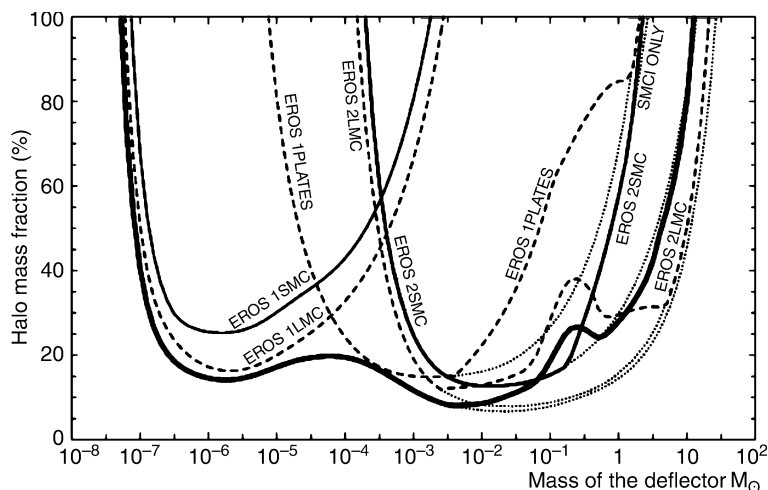


Fig. 2.30. From observations by the EROS collaboration, a large mass range for MACHO candidates can be excluded. The maximum allowed fraction of the halo mass contained in MACHOs is plotted as a function of the MACHO mass M , as an upper limit with 95% confidence. A standard model for the mass distribution in the Galactic halo was assumed which describes the rotation curve of the Milky Way quite well. The various curves show different phases of the EROS experiment. They are plotted separately for observations in

the directions of the LMC and the SMC. The experiment EROS 1 searched for microlensing events on short time-scales but did not find any; this yields the upper limits at small masses. Upper limits at larger masses were obtained by the EROS 2 experiment. The thick solid curve represents the upper limit derived from combining the individual experiments. If not a single MACHO event had been found the upper limit would have been described by the dotted line

2.5.4 Variations and Extensions

Besides the search for MACHOs, microlensing surveys have yielded other important results and will continue to do so in the future. For instance, the distribution of stars in the Galaxy can be measured by analyzing the lensing probability as a function of direction. Thousands of variable stars have been newly discovered and accurately monitored; the extensive and publicly accessible databases of the surveys form an invaluable resource for stellar astrophysics. Furthermore, globular clusters in the LMC have been identified from these photometric observations.

For some lensing events, the radius and the surface structure of distant stars can be measured with very high precision. This is possible because the magnification μ depends on the position of the source. Situations can occur, for example where a binary star acts as a lens (see Fig. 2.31), in which the dependence of the magnification on the position in the source plane is very sensitive. Since the source – the star – is in motion relative to the line-of-sight between Earth and the lens, its different

regions are subject to different magnification, depending on the time-dependent source position. A detailed analysis of the light curve of such events then enables us to reconstruct the light distribution on the surface of the star. The light curve of one such event is shown in Fig. 2.32.

For these lensing events the source can no longer be assumed to be a point source. Rather, the details of the light curve are determined by its light distribution. Therefore, another length-scale appears in the system, the radius of the star. This length-scale shows up in the corresponding microlensing light curve, as can be seen in Fig. 2.32, by the time-scale which characterizes the width of the peaks in the light curve – it is directly related to the ratio of the stellar radius and the transverse velocity of the lens. With this new scale, the degeneracy between M , v , and D_d is partially broken, so that these special events provide more information than the “classical” ones.

In fact, the light curve in Fig. 2.27 is probably not caused by a single lens star, but instead by additional slight disturbances from a companion star. This would

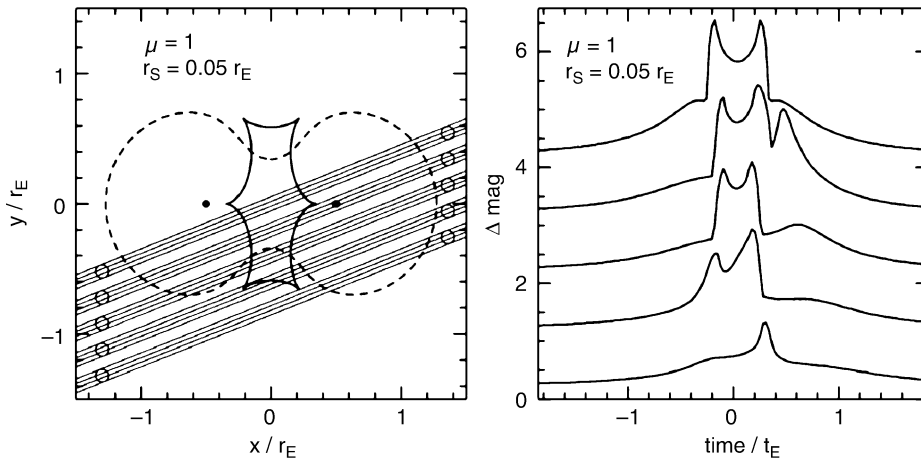


Fig. 2.31. If a binary star acts as a lens, significantly more complicated light curves can be generated. In the left-hand panel tracks are plotted for five different relative motions of a background source; the dashed curve is the so-called *critical curve*, formally defined by $\det(\partial\beta/\partial\theta) = 0$, and the solid line is the corresponding image of the critical curve in the source plane, called a *caustic*. Light curves corresponding to these five

tracks are plotted in the right-hand panel. If the source crosses the caustic, the magnification μ becomes very large – formally infinite if the source was point-like. Since it has a finite extent, μ has to be finite as well; from the maximum μ during caustic crossing, the radius of the source can be determined, and sometimes even the variation of the surface brightness across the stellar disk, an effect known as limb darkening

explain the deviation of the observed light curve from a simple model light curve. However, the sampling in time of this particular light curve is not sufficient to determine the parameters of the binary system.

By now, detailed light curves with very good time coverage have been measured, which was made possible with an alarm system. The data from those groups searching for microlensing events are analyzed immediately after observations, and potential candidates for interesting events are published on the Internet. Other groups (such as the PLANET collaboration, for example) then follow-up these systems with very good time coverage by using several telescopes spread over a large range in geographical longitude. This makes around-the-clock observations of the event possible. Using this method light curves of extremely high quality have been measured. These groups hope to detect extra-solar planets by characteristic deviations in these light curves. Indeed, these microlens observations may be the most realistic (and cheapest) option for finding low-mass planets. Other methods for finding extra-solar planets, such as the search for small periodic changes of the radial velocity of stars which is caused by the gravitational pull of their orbiting planet, are mostly sensitive to high-mass planets. Whereas such surveys

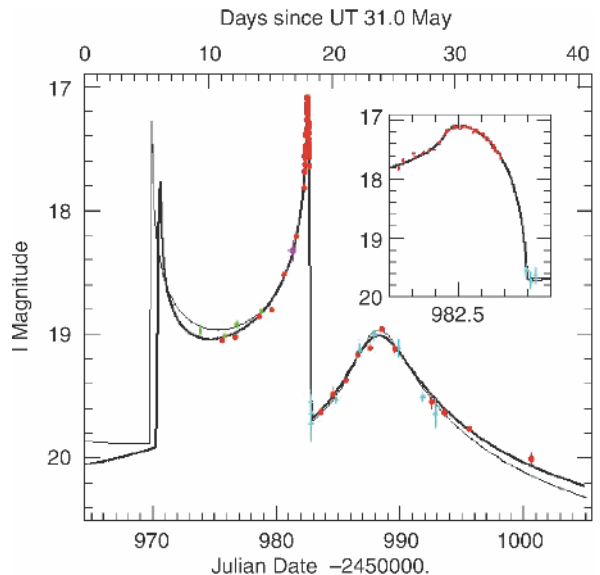


Fig. 2.32. Light curve of an event in which the lens was a binary star. The MACHO group discovered this “binary event”. Members of the PLANET collaboration obtained this data using four different telescopes (in Chile, Tasmania, and South Africa). The second caustic crossing is highly resolved (displayed in the small diagram) and allows us to draw conclusions about the size and the brightness distribution of the source star. The two curves show the fits of a binary lens to the data

have been extremely successful in the past decade, having detected far more than one hundred planets around other stars, the characteristic mass of these planets is that of Jupiter, i.e., ~ 1000 times more massive than the Earth. At least two planet-mass companions to lens stars have already been discovered through microlensing, one of them having a mass of only six times that of the Earth.

Pixel Lensing. An extension to the microlensing search was suggested in the form of the so-called pixel lensing method. Instead of measuring the light curve of a single star one records the brightness of groups of stars that are positioned closely together on the sky. This method is applicable in situations where the density of source stars is very high, such as for the stars in the Andromeda galaxy (M31), which cannot be resolved individually. If one star is magnified by a microlensing event, the brightness in the corresponding region changes in a characteristic way, similar to that in the lensing events discussed above. To identify such events, the magnification needs to be relatively large, because only then can the light of the lensed star dominate over the local brightness in the region, so that the event can be recognized. On the other hand, the number of photometrically monitored stars (per solid angle) is larger than in surveys where single stars are observed, so that events of larger magnification are also more abundant. By now, several groups have successfully started to search for microlensing events in M31. The quantitative analysis of these surveys is more complicated than for the surveys targeting the Magellanic Clouds. However, the M31 experiments are equally sensitive to both MACHOs in the halo of our Milky Way and in that of M31. Therefore, these surveys promise to finally resolve the question of whether part of the dark matter consists of MACHOs.

Annihilation Radiation due to Dark Matter? The 511 keV annihilation radiation from the Galactic bulge, discussed in Sect. 2.3.4 above, has been suggested to be related to dark matter particles. Depending on the density of dark matter in the center of the Galaxy, as well as on the cross-section of the constituent particles of the dark matter (if it is indeed due to elementary particles), these particles can annihilate. In this process, positrons might be released which can then annihilate

with the electrons of the interstellar medium. However, in order for this to be the source of the 511 keV line radiation, the dark matter particles must have rather “exotic” properties.

2.6 The Galactic Center

The Galactic center (GC, see Fig. 2.33) is not observable at optical wavelengths, because the extinction in the V-band is ~ 28 mag. Our information about the GC has

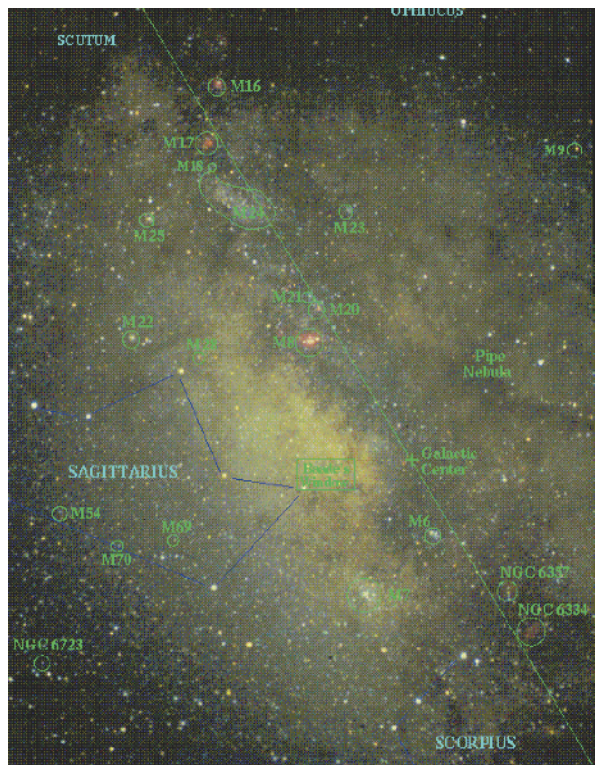


Fig. 2.33. Optical image in the direction of the Galactic center. Marked are some Messier objects: gas nebulae such as M8, M16, M17, M20; open star clusters such as M6, M7, M18, M21, M23, M24, and M25; globular clusters such as M9, M22, M28, M54, M69, and M70. Also marked is the Galactic center, as well as the Galactic plane, which is indicated by a line. Baade’s Window can be easily recognized, a direction in which the extinction is significantly lower than in nearby directions, so that a clear increase in stellar density is visible there. This is the reason why the microlensing observations towards the Galactic center were preferably done in Baade’s Window

been obtained from radio-, IR-, and X-ray radiation. Since the GC is nearby, and thus serves as a prototype of the central regions of galaxies, its observation is of great interest for our understanding of the processes taking place in the centers of galaxies.

2.6.1 Where is the Galactic Center?

The question of where the center of our Milky Way is located is by no means trivial, because the term “center” is in fact not well-defined. Is it the center of mass of the Galaxy, or the point around which the stars and the gas are orbiting? And how could we pinpoint this “center” accurately? Fortunately, the center can nevertheless be localized because, as we will see below, a distinct source exists that is readily identified as the Galactic center.

Radio observations in the direction of the GC show a relatively complex structure, as is displayed in Fig. 2.34.

A central disk of HI gas exists at radii from several 100 pc up to about 1 kpc. Its rotational velocity yields a mass estimate $M(R)$ for $R \gtrsim 100$ pc. Furthermore, radio filaments are observed which extend perpendicularly to the Galactic plane, and also a large number of supernova remnants are seen. Within about 2 kpc from the center, roughly $3 \times 10^7 M_\odot$ of atomic hydrogen is found. Optical images show regions close to the GC towards which the extinction is significantly lower. The best known of these is Baade’s window – most of the microlensing surveys towards the bulge are conducted in this region. In addition, a fairly large number of globular clusters and gas nebulae are observed towards the central region. X-ray images (Fig. 2.35) show numerous X-ray binaries, as well as diffuse emission by hot gas.

The innermost 8 pc contain the radio source Sgr A (Sagittarius A), which itself consists of different components:

- A circumnuclear molecular ring, shaped like a torus, which extends between radii of $2 \text{ pc} \lesssim R \lesssim 8 \text{ pc}$ and is inclined by about 20° relative to the Galactic disk. The rotational velocity of this ring is about $\sim 110 \text{ km/s}$, nearly independent of R . This ring has a sharp inner boundary; this cannot be the result of an equilibrium flow, because internal turbulent motions would quickly (on a time-scale of $\sim 10^5 \text{ yr}$) erase this boundary. Probably, it is evidence of an ener-

getic event that occurred in the Galactic center within the past $\sim 10^5$ years. This interpretation is also supported by other observations, e.g., by a clumpiness in density and temperature.

- Sgr A East, a non-thermal (synchrotron) source of shell-like structure. Presumably this is a supernova remnant (SNR), with an age between 100 and 5000 years.
- Sgr A West is located about $1/5$ away from Sgr A East. It is a thermal source, an unusual HII region with a spiral-like structure.
- Sgr A* is a strong compact radio source close to the center of Sgr A West. Recent observations with mm-VLBI show that its extent is smaller than 3 AU. The radio luminosity is $L_{\text{rad}} \sim 2 \times 10^{34} \text{ erg/s}$. Except for the emission in the mm and cm domain, Sgr A* is a weak source. Since other galaxies often have a compact radio source in their center, Sgr A* is an excellent candidate for being the center of our Milky Way.

Through observations of stars which contain a radio maser¹⁴ source, the astrometry of the GC in the radio domain was matched to that in the IR, i.e., the position of Sgr A* is also known in the IR.¹⁵ The uncertainty in the relative positions between radio and IR observations is only $\sim 30 \text{ mas}$ – at a presumed distance of the GC of 8 kpc, one arcsecond corresponds to 0.0388 pc, or about 8000 AU.

2.6.2 The Central Star Cluster

Density Distribution. Observations in the K-band ($\lambda \sim 2 \mu\text{m}$) show a compact star cluster that is centered on Sgr A*. Its density behaves like $\propto r^{-1.8}$ in the distance range $0.1 \text{ pc} \lesssim r \lesssim 1 \text{ pc}$. The number density

¹⁴ Masers are regions of stimulated non-thermal emission which show a very high surface brightness. The maser phenomenon is similar to that of lasers, except that the former radiate in the microwave regime of the spectrum. Masers are sometimes found in the atmospheres of active stars.

¹⁵ One problem in the combined analysis of data taken in different wavelength bands is that astrometry in each individual wavelength band can be performed with a very high precision – e.g., individually in the radio and the IR band – however, the relative astrometry between these bands is less well known. To stack maps of different wavelength precisely “on top of each other”, knowledge of exact relative astrometry is essential. This can be gained if a population of compact sources exists that is observable in both wavelength domains and for which accurate positions can be measured.

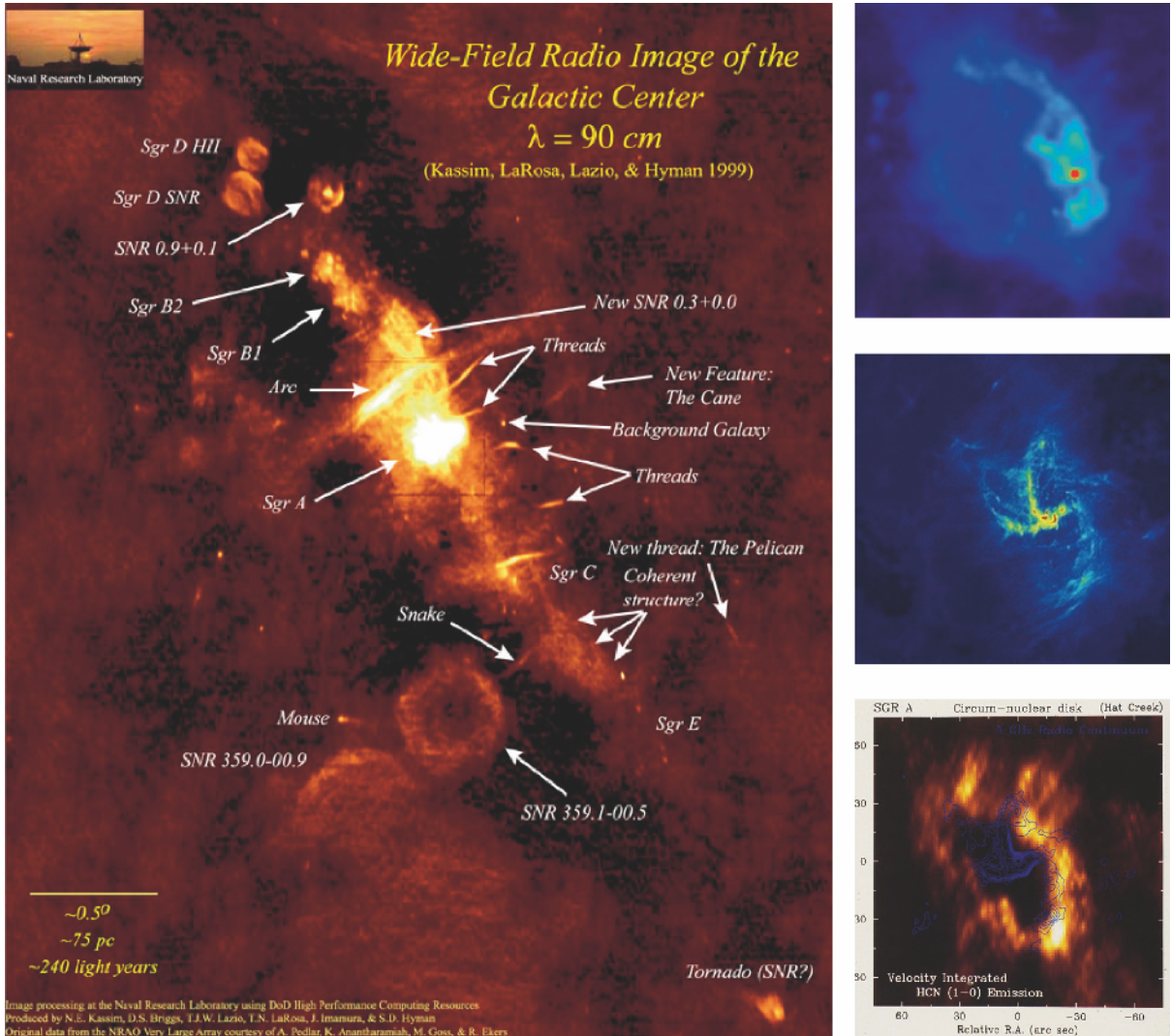


Fig. 2.34. Left: A VLA wide-field image of the region around the Galactic center, with a large number of sources identified. Upper right: a 20 cm continuum VLA image of Sgr A East,

where the red dot marks Sgr A*. Center right: Sgr A West, as seen in a 6-cm continuum VLA image. Lower right: the circumnuclear ring in HCN line emission

of stars in its inner region is so large that close stellar encounters are common. It can be estimated that a star has a close encounter about every $\sim 10^6$ years. Thus, it is expected that the distribution of the stars is “thermalized”, which means that the local velocity distribution of the stars is the same everywhere, i.e., it is close to a Maxwellian distribution with a constant velocity dispersion. For such an isothermal distribution we expect

a density profile $n \propto r^{-2}$, which is in good agreement with the observation.

However, another observational result yields a striking and interesting discrepancy with respect to the idea of an isothermal distribution. Instead of the expected constant dispersion σ of the radial velocities of the stars, a strong radial dependence is observed: σ increases towards smaller r . For example, one finds $\sigma \sim 55 \text{ km/s}$ at



Fig. 2.35. Mosaic of X-ray images of the Galactic center, taken by the Chandra satellite. The image covers an area of about $130 \text{ pc} \times 300 \text{ pc}$ ($48' \times 120'$). The actual GC, in which a supermassive black hole is suspected to reside, is located in the white region near the center of the image. Furthermore, on this image hundreds of white dwarfs, neutron stars, and

black holes are visible that radiate in the X-ray regime due to accretion phenomena (accreting X-ray binaries). Colors code the photon energy, from low energy (red) to high energy (blue). The diffuse emission, predominantly red in this image, originates in diffuse hot gas with a temperature of about $T \sim 10^7 \text{ K}$

$r = 5 \text{ pc}$, but $\sigma \sim 180 \text{ km/s}$ at $r = 0.15 \text{ pc}$. This discrepancy indicates that the gravitational potential in which the stars are moving is generated not only by themselves. According to the virial theorem, the strong increase of σ for small r implies the presence of a central mass concentration in the star cluster.

Proper Motions. Since the middle of the 1990s, proper motions of stars in this star cluster have also been measured, using the methods of speckle interferometry and adaptive optics. These produce images at diffraction-limited angular resolution, about $\sim 0''.15$ in the K-band at the ESO/NTT (3.5 m) and about $\sim 0''.05$ at the Keck (10 m). Proper motions are currently known for about 1000 stars within $\sim 10''$ of Sgr A*. This breakthrough was achieved independently by two groups, whose results are in excellent agreement. For more than 20 stars within $\sim 5''$ of Sgr A* both proper motions and radial velocities, and therefore their three-dimensional velocities are known. The radial and tangential velocity dispersions resulting from these measurements are in good mutual agreement. Thus, it can be concluded that a basically isotropic distribution of the stellar orbits exists, simplifying the study of the dynamics of this stellar cluster.

The Origin of Very Massive Stars near the Galactic Center. One of the unsolved problems is the presence of these massive stars close to the Galactic center. One

finds that most of the innermost stars are main-sequence B-stars. Their small lifetime of $\sim 10^8 \text{ yr}$ probably implies that these stars were born close to the Galactic center. This, however, is very difficult to understand. Both the strong tidal gravitational field of the central black hole (see below) and the presumably strong magnetic field in this region will prevent the “standard” star-formation picture of a collapsing molecular cloud: the former effect tends to disrupt such a cloud while the latter stabilizes it against gravitational contraction. Several solutions to this problem have been suggested, such as a scenario in which the stars are born at larger distances from the Galactic center and then brought there by dynamical processes, involving strong gravitational scattering events. However, none of these models appears satisfactory at present.

2.6.3 A Black Hole in the Center of the Milky Way

Some stars within $0''.6$ of Sgr A* have a proper motion of more than 1000 km/s , as shown in Fig. 2.36. For instance, the star S1 has a separation of only $0''.1$ from Sgr A* and shows proper motion of 1470 km/s at the epoch displayed in Fig. 2.36. Combining the velocity dispersions in radial and tangential directions reveals it to be increasing according to the Kepler law for the presence of a point mass, $\sigma \propto r^{-1/2}$ down to $r \sim 0.01 \text{ pc}$.

By now, the *acceleration* of some stars in the star cluster has also been measured, i.e., the change of proper

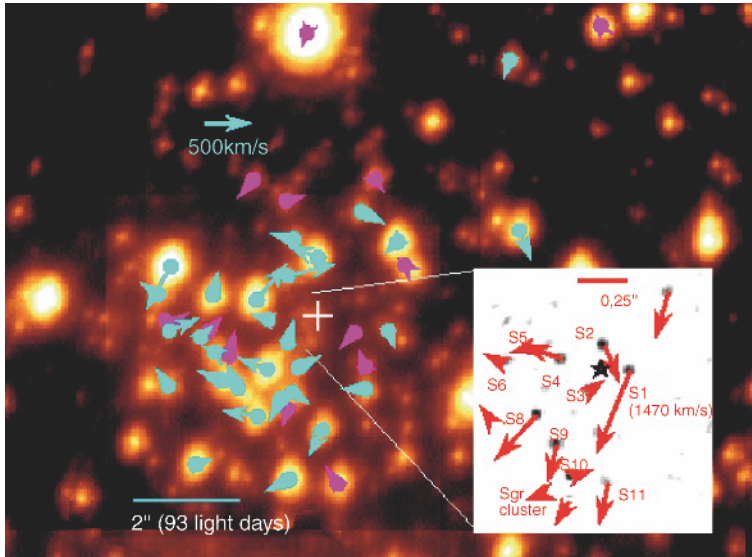


Fig. 2.36. Proper motions of stars in the central region of the GC. The differently colored arrows denote different types of stars. The small image shows the proper motions in the Sgr A* star cluster within half an arcsecond from Sgr A*; the fastest star (S1) has a proper motion of ~ 1500 km/s (from Genzel, 2000, astro-ph/0008119)

motion with time. From these measurements Sgr A* indeed emerges as the focus of the orbits and thus as the center of mass. Figure 2.37 shows the orbits of some stars around Sgr A*. The star S2 could be observed during a major fraction of its orbit, where a maximum velocity of more than 5000 km/s was found. The eccentricity of the orbit of S2 is 0.87, and its orbital period is ~ 15.7 yr. The minimum separation of this star from Sgr A* is only 6×10^{-4} pc, or about 100 AU.

From the observed kinematics, the enclosed mass $M(r)$ can be calculated, see Fig. 2.38. The corresponding analysis yields that $M(r)$ is basically constant over the range $0.01 \text{ pc} \lesssim r \lesssim 0.5 \text{ pc}$. This exciting result clearly indicates the presence of a point mass, for which a mass of

$$M = (3.6 \pm 0.4) \times 10^6 M_{\odot} \quad (2.91)$$

is determined. For larger radii, the mass of the star cluster dominates; it nearly follows an isothermal density distribution with a core radius of ~ 0.34 pc and a central density of $3.6 \times 10^6 M_{\odot}/\text{pc}^3$. This result is also compatible with the kinematics of the gas in the center of the Galaxy. However, stars are much better kinematic indicators because gas can be affected by magnetic fields, viscosity, and various other processes besides gravity.

The kinematics of stars in the central star cluster of the Galaxy shows that our Milky Way contains a mass concentration in which $\sim 3 \times 10^6 M_{\odot}$ are concentrated within a region smaller than 0.01 pc. This is most probably a black hole in the center of our Galaxy at the position of the compact radio source Sgr A*.

Why a Black Hole? We have interpreted the central mass concentration as a black hole; this requires some further explanation:

- The energy for the central activity in quasars, radio galaxies, and other AGNs is produced by accretion of gas onto a supermassive black hole (SMBH); we will discuss this in more detail in Sect. 5.3. Thus we know that at least a subclass of galaxies contains a central SMBH. Furthermore, we will see in Sect. 3.5 that many “normal” galaxies, especially ellipticals, harbor a black hole in their center. The presence of a black hole in the center of our own Galaxy would therefore not be something unusual.
- To bring the radial mass profile $M(r)$ into accordance with an extended mass distribution, its density distribution must be very strongly concentrated, with a density profile steeper than $\propto r^{-4}$; otherwise the

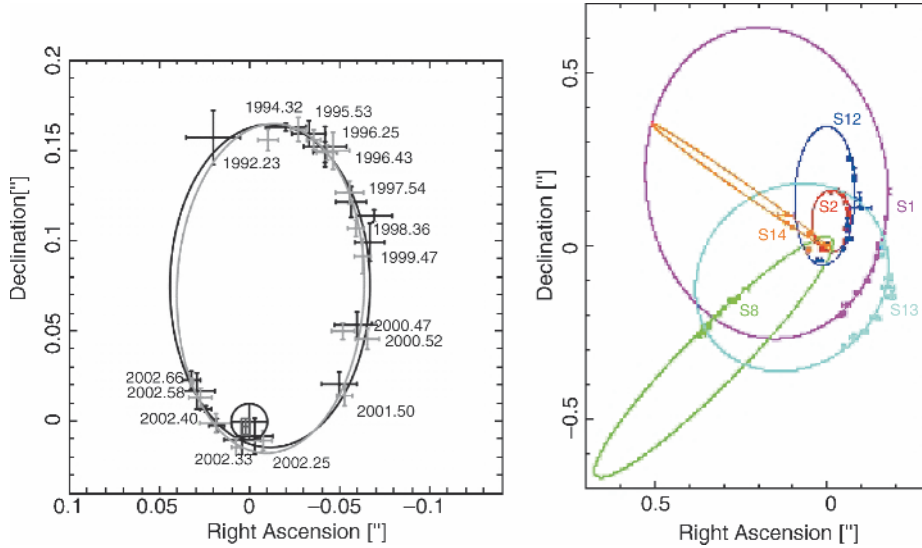


Fig. 2.37. At left, the orbit of the star S2 around Sgr A* is shown as determined by two different observing campaigns. The position of Sgr A* is indicated by the black circled cross. The individual points along the orbit are identified by the epoch of the observation. The right-hand image shows the orbits of some other stars for which accelerations have already been measured

mass profile $M(r)$ would not be as flat as observed in Fig. 2.38. Hence, this hypothetical mass distribution must be vastly different from the expected isothermal distribution which has a mass profile $\propto r^{-2}$, as discussed in Sect. 2.6.2. However, observations of the stellar distribution provide no indication of an inwardly increasing density of the star cluster with such a steep profile.

- Even if such an ultra-dense star cluster (with a central density of $\gtrsim 4 \times 10^{12} M_{\odot}/\text{pc}^3$) were present it could not be stable, but instead would dissolve within $\sim 10^7$ years through frequent stellar collisions.
- Sgr A* itself has a proper motion of less than 20 km/s. It is therefore the dynamic center of the Milky Way. Due to the large velocities of its surrounding stars, one would derive a mass of $M \gg 10^3 M_{\odot}$ for the radio source, assuming equipartition of energy (see also Sect. 2.6.5). Together with the tight upper limits for its extent, a lower limit for the density of $10^{18} M_{\odot}/\text{pc}^3$ can then be obtained.

Following the stellar orbits in forthcoming years will further complete our picture of the mass distribution in the GC.

We have to emphasize at this point that the gravitational effect of the black hole on the motion of stars and gas is constrained to the innermost region of the

Milky Way. As one can see from Fig. 2.38, the gravitational field of the SMBH dominates the rotation curve of the Galaxy only for $R \lesssim 2$ pc – this is the very reason why the detection of the SMBH is so difficult. At larger radii, the presence of the SMBH is of no relevance for the rotation curve of the Milky Way.

2.6.4 Flares from the Galactic Center

In 2000, the X-ray satellite Chandra discovered a powerful X-ray flare from Sgr A*. This event lasted for about three hours, and the X-ray flux increased by a factor of 50 during this period. XMM-Newton confirmed the existence of X-ray flares, recording one where the luminosity increased by a factor of ~ 200 . Combining the flare duration of a few hours with the short time-scale of variability of a few minutes indicates that the emission must originate from a very small source, not larger than $\sim 10^{13}$ cm in size.

Monitoring Sgr A* in the NIR, flare emission was also found in this spectral regime. These NIR flares are more frequent than in X-rays, occurring several times per day. Furthermore, the NIR emission seems to show some sort of periodicity of ~ 17 min, which is most likely to be identified with an orbital motion of the emitting material around the SMBH. Indeed, a re-analysis of the X-ray light curve shows some hint of

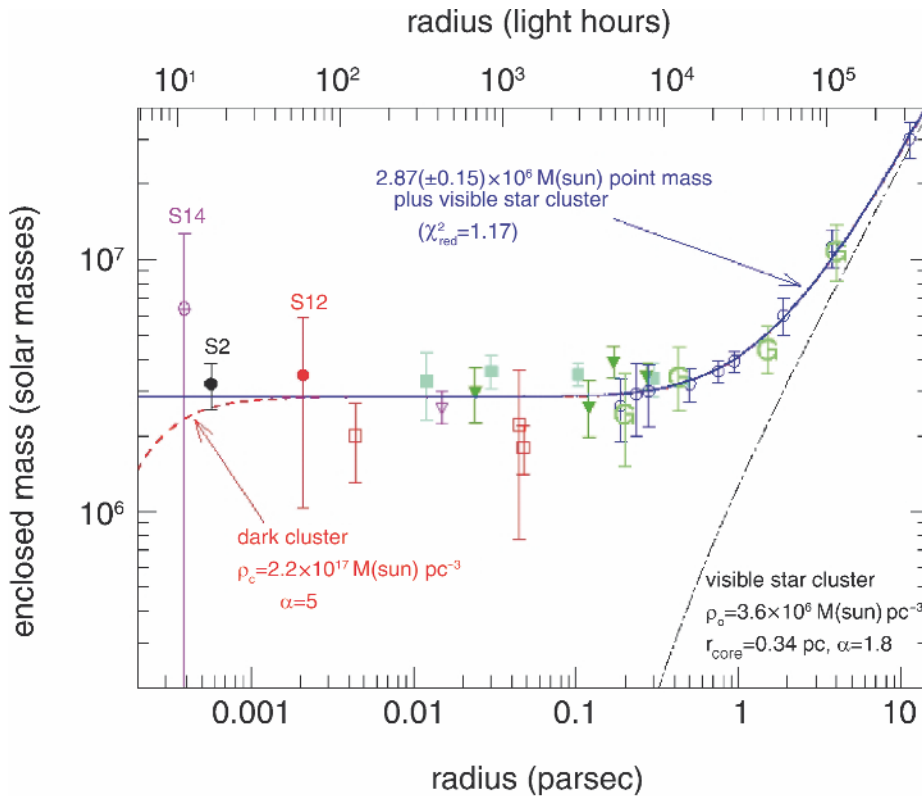


Fig. 2.38. Determination of the mass $M(r)$ within a radius r from Sgr A*, as measured by the radial velocities and proper motions of stars in the central cluster. Mass estimates obtained from individual stars (S14, S2, S12) are given by the points with error bars for small r . The other data points were derived from the kinematic analysis of the observed proper motions of the stars, where different methods have been applied. As can be seen, these methods produce results that are mutu-

ally compatible, so that the mass profile plotted here can be regarded to be robust. The solid curve is the best-fit model, representing a point mass of $2.9 \times 10^6 M_{\odot}$ plus a star cluster with a central density of $3.6 \times 10^6 M_{\odot}/\text{pc}^3$ (the mass profile of this star cluster is indicated by the dash-dotted curve). The dashed curve shows the mass profile of a hypothetical cluster with a very steep profile, $n \propto r^{-5}$, and a central density of $2.2 \times 10^{17} M_{\odot} \text{pc}^{-3}$

the same modulation time-scale. Observing the Galactic center simultaneously in the NIR and the X-rays revealed a clear correlation of the corresponding light curves; for example, simultaneous flares were found in these two wavelength regimes. These flares have similar light profiles, indicating a similar origin of their radiation. The consequences of these observations for the nature of the central black hole will be discussed in Sect. 5.4.6, after we have introduced the concept of black holes in a bit more detail. Flares were also observed at mm-wavelengths; their time-scale appears to be longer than that at higher frequencies, as expected

if the emission comes from a more extended source component.

2.6.5 The Proper Motion of Sgr A*

From a series of VLBI observations of the position of Sgr A*, covering eight years, the proper motion of this compact radio source was measured with very high precision. To do this, the position of Sgr A* was determined relative to two compact extragalactic radio sources. Due to their large distances these are not expected to show

any proper motion, and the VLBI measurements show that their separation vector is indeed constant over time. The position of Sgr A* over the observing period is plotted in Fig. 2.39.

From the plot, we can conclude that the observed proper motion of Sgr A* is essentially parallel to the Galactic plane. The proper motion perpendicular to the Galactic plane is about 0.2 mas/yr, compared to the proper motion in the Galactic plane of 6.4 mas/yr. If $R_0 = (8.0 \pm 0.5)$ kpc is assumed for the distance to the GC, this proper motion translates into an orbital velocity of (241 ± 15) km/s, where the uncertainty is dominated by the exact value of R_0 (the error in the measurement alone would yield an uncertainty of only 1 km/s). This proper motion is easily explained by the Solar orbital

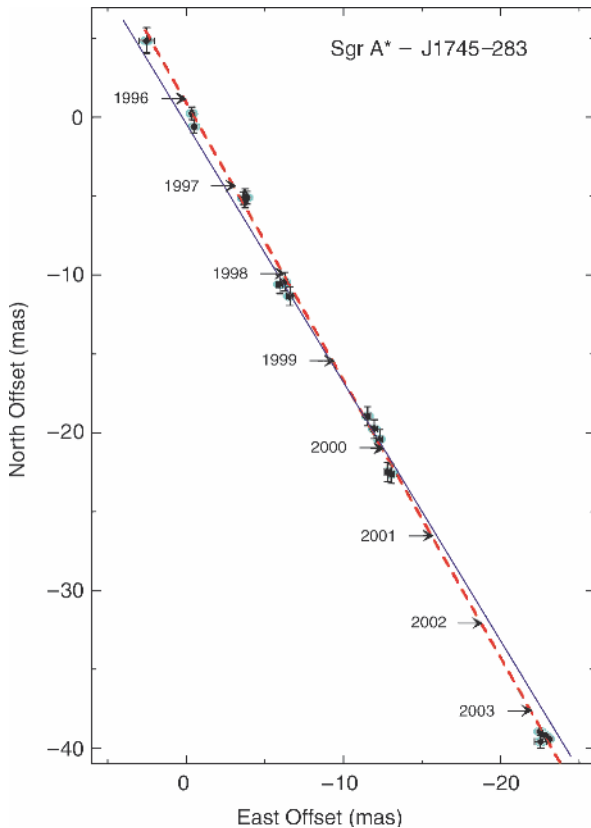


Fig. 2.39. The position of Sgr A* at different epochs, relative to the position in 1996. To a very good approximation the motion is linear, as indicated by the dashed best-fit straight line. In comparison, the solid line shows the orientation of the Galactic plane

motion around the GC, i.e., this measurement contains no hint of a non-zero velocity of the radio source Sgr A* itself. In fact, the small deviation of the proper motion from the orientation of the Galactic plane can be explained by the peculiar velocity of the Sun relative to the LSR (see Sect. 2.4.1). If this is taken into account, a velocity perpendicular to the Galactic disk of $v_{\perp} = (-0.4 \pm 0.9)$ km/s is obtained for Sgr A*. The component of the orbital velocity within the disk has a much larger uncertainty because we know neither R_0 nor the rotational velocity V_0 of the LSR very precisely. The small upper limit for v_{\perp} suggests, however, that the motion in the disk should also be very small. Under the (therefore plausible) assumption that Sgr A* has no peculiar velocity, the ratio R_0/V_0 can be determined from these measurements with an as yet unmatched precision.

What also makes this observation so impressive is that from it we can directly derive a lower limit for the mass of Sgr A*. Since this radio source is surrounded by $\sim 10^6$ stars within a sphere of radius ~ 1 pc, the net acceleration towards the center is not vanishing, even in the case of a statistically isotropic distribution of stars. Rather, due to the discrete nature of the mass distribution, a stochastic force exists that changes with time because of the orbital motion of the stars. The radio source is accelerated by this force, causing a motion of Sgr A* which becomes larger the smaller the mass of the source. The very strong limits to the velocity of Sgr A* enable us to derive a lower limit for its mass of $0.4 \times 10^6 M_{\odot}$. This mass limit is significantly lower than the mass of the SMBH that was derived from the stellar orbits, but it is the mass of the radio source itself. Although we have excellent reasons to assume that Sgr A* coincides with the SMBH, this new observation is the first proof for a large mass of the radio source itself.

2.6.6 Hypervelocity Stars in the Galaxy

Discovery. In 2005, a Galactic star was discovered which travels with a velocity of at least 700 km/s relative to the Galactic rest-frame. This B-star has a distance of ~ 110 kpc from the Galactic center, and its actual space velocity depends on its transverse motion which has not been measured, due to the large distance of the object from us. The velocity of this star is so large that it exceeds the escape velocity from the Galaxy;

hence, this star is gravitationally unbound to the Milky Way. Within one year after this first discovery, four more such *hypervelocity stars* have been discovered, all of them early-type stars (O- or B-stars) with Galactic rest-frame velocities in excess of 500 km/s. They will all escape the gravitational potential of the Galaxy.

Acceleration of Hypervelocity Stars. The fact that the hypervelocity stars are gravitationally unbound to the Milky Way implies that they must have been accelerated very recently, i.e., less than a crossing time through the Galaxy ago. In addition, since they are early-type stars, they must have been accelerated within the lifetime of such stars. The acceleration mechanism must be of gravitational origin and is related to the *dynamical instability* of N -body systems, with $N > 2$. A pair of objects will orbit in their joint gravitational field, either on bound orbits (ellipses) or unbound ones (gravitational scattering on hyperbolic orbits); in the former case, the system is stable and the two masses will orbit around each other literally forever. If more than two masses are involved this is no longer the case – such a system is inherently unstable. Consider three masses, initially bound to each other, orbiting around their center-of-mass. In general, their orbits will not be ellipses but are more complicated; in particular, they are not periodic. Such a system is, mathematically speaking, chaotic. A chaotic system is characterized by the property that the state of a system at time t depends very sensitively on the initial conditions set at time $t_i < t$. Whereas for a dynamically stable system the positions and velocities of the masses at time t are changed only a little if their initial conditions are slightly varied (e.g., by giving one of the masses a slightly larger velocity), in a chaotic, dynamically unstable system even tiny changes in the initial conditions can lead to completely different states at later times. Any N -body system with $N > 2$ is dynamically unstable.

Back to our three-body system. The three masses may orbit around each other for an extended period of

time, but their gravitational interaction may then change the state of the system suddenly, in that one of the three masses attains a sufficiently high velocity relative to the other two and may escape to infinity, whereas the other two masses form a binary system. What was a bound system initially may become an unbound system later on. This behavior may appear unphysical at first sight – where does the energy come from to eject one of the stars? Is this process violating energy conservation?

Of course not! The trick lies in the properties of gravity: a binary has *negative* binding energy, and the more negative, the tighter the binary orbit. By three-body interactions, the orbit of two masses can become tighter (one says that the binary “hardens”), and the corresponding excess energy is transferred to the third mass which may then become gravitationally unbound. In fact, a single binary of compact stars can in principle take up all the binding energy of a star cluster and “evaporate” all other stars.

This discussion then leads to the explanation of hypervelocity stars. The characteristic escape velocity of the “third mass” will be the orbital velocity of the three-body system before the escape. The only place in our Milky Way where orbital velocities are as high as that observed for the hypervelocity stars is the Galactic center. In fact, the travel time of a star with current velocity of ~ 600 km/s from the Galactic center to Galactrocentric distances of ~ 80 kpc is of order 10^8 yr, slightly shorter than the main-sequence lifetime of a B-star. Furthermore, most of the bright stars in the central $1''$ of the Galactic center region are B-stars. Therefore, the immediate environment of the central black hole is the natural origin for these hypervelocity stars. Indeed, long before their discovery the existence of such stars was predicted. When a binary star gets close to the black hole, this three-body interaction can lead to the ejection of one of the two stars into an unbound orbit. Thus, the existence of hypervelocity stars can be considered as an additional piece of evidence for the presence of a central black hole in our Galaxy.